



University of
Massachusetts
Amherst

Electronic Spectroscopy And Dissociation Dynamics Of Gasphase Transition Metal Containing Cations And Dications

Item Type	Dissertation (Open Access)
Authors	Perera, Kanchana Manori
DOI	10.7275/5648204
Download date	2026-03-14 14:33:25
Link to Item	https://hdl.handle.net/20.500.14394/16506

**ELECTRONIC SPECTROSCOPY AND DISSOCIATION DYNAMICS OF GAS-
PHASE TRANSITION METAL CONTAINING CATIONS AND DICATIONS**

A Dissertation Presented

by

KANCHANA MANORI PERERA

Submitted to the Graduate School of the
University of Massachusetts Amherst in partial fulfillment
of the requirements for the degree of

DOCTOR OF PHILOSOPHY

February 2009

Department of Chemistry

© Copyright by Kanchana Manori Perera 2009
All Rights Reserved

ELECTRONIC SPECTROSCOPY AND DISSOCIATION DYNAMICS OF GAS-
PHASE TRANSITION METAL CONTAINING CATIONS AND DICATIONS

A Dissertation Presented

by

Kanchana Manori Perera

Approved as to style and content by:

Ricardo B. Metz, Chair

Michael Maroney, Member

Richard Vachet, Member

Thomas Russell, Member

Bret E. Jackson, Department Head
Department of Chemistry

To my Ammi and Thathi

for your unconditional love.

ACKNOWLEDGMENTS

This thesis/research would not have been possible without the support and inspiration of many people. I would like to thank all who have helped and inspired me during my doctoral study at University of Massachusetts. First, I would like to express my sincere appreciation and gratitude to Prof. Ricardo B. Metz, my thesis advisor, for his support and encouragement during the six years of graduate life I have spend in his lab. The extent of my handy work was hammering a nail when I joined Rick's group. However throughout my time spend with him; I have gain confidence in building instrument to fixing pumps. Rick has inspired me to be a patient scientist with attention on details as well as a caring teacher. Thank you for all the advices you gave me on lab work as well as in general life almost like my second father (much much younger) and for the sense of humor and passion for research. Mostly I am grateful that you were patient when I was discouraged with lack of result and encourage me to strive for more. Also, thank you for making ALS trip worth while and showing me the dedication and the long work days that you need to achieve something can be sweet later.

Also, I would like to thank my dissertation committee, Richard Vachet, Michael Maroney and Tom Russell. I had the privilege of being in classes with Mike and Tom. I learned pchem in a different light when I took Mike's inorganic class. I was always grateful of Richard's generosity for letting me take diffusion pump part from his lab anytime and also for his calm and organized nature that inspired me as a

person. I have had the privilege of working with most wonderful bunch of ladies in chem. main office as well as Bob, Ashley, Walter and Mark were undeniably the most helpful and resourceful people in my grad school life.

Initially when I started graduate school I was drawn to Metz lab immediately. All the people I met throughout my graduate school life have made the experience enjoyable. I had some unique experiences like learned to play softball, and drink under the stars until 4 am in the morning and still come to lab next morning ready to work at 8am. Many wonderful memories are result of wonderful companionship of Chris, Kay, Jen, Murat, Paul and Gokhan. Also, Aruni for being there for me during the thesis writing process and feeding me and keeping my sanity to whom I am eternally grateful. I am very lucky to have known Kanchana, Chey, Mirna, Ioana, Tashya, Hemali and Chandana for being true friends. Usha, thank you for all the proof reading you had to do to make my thesis possible in just six weeks. It was amazing the turn over rate of the proof reading, I am very thankful for you. Sandra Eaton was my first favorite pchem professor at DU. I learned to love pchem because of her and she is the inspiration of mine to be a professor one day.

My deepest gratitude goes to my family for their unflagging love and support throughout my life. I am indebted to my mother and father, for teaching me to dream big and work hard towards achieving it. I am lucky to have unconditional love from both of you and all the phone calls and understanding when I felt nobody understood me. I am everything because of you and the confidence you have build on me. I was

taught never to complain (even though that was unavoidable) but to appreciate all I had which has stuck with me and inspire me to dream high. I am very proud to be your daughter, thank you for being there for me even when I was questioning myself. Also, I am very grateful for Pathmal aiya for giving me the opportunity to come to US for higher studies; you opened a box of dreams that might have never been possible for me. For Loku and Chuti aiya, thank you for being supportive and caring siblings. I am very lucky to have the family and the love and support of them. I also want to thank my new in-laws for their thoughtfulness and love and for Gehan for being a younger brother I never had. I am grateful for having Thushara as my friend and husband. You have opened my life to sunshine. I owe you for inspiring me, share the knowledge and experience and for the persistent confidence in me. We have weathered storms in this short period and lived life on fast track. Thank you for being in my life with open arms on everything.

ABSTRACT

ELECTRONIC SPECTROSCOPY AND DISSOCIATION DYNAMICS OF GAS-PHASE TRANSITION METAL CONTAINING CATIONS AND DICATIONS

February 2009

KANCHANA MANORI PERERA, B.Sc., UNIVERSITY OF DENVER

M.Sc., UNIVERSITY OF MASSACHUSETTS AMHERST

Ph.D., UNIVERSITY OF MASSACHUSETTS AMHERST

Directed by: Professor Ricardo B. Metz

Studies of gas-phase ionic clusters have become an integral component in understanding microsolvation and catalysis by transition metal cations. Further interest in this field is due to the possibility of bridging the gap between the condensed and gas phases by developing our understanding of clusters and the possibility that small clusters can have unique chemical and catalytic properties. Most gas phase studies have focused on singly charged ions. Electrospray allows for the production of multiply charged ions solvated by a few solvent molecules. Understanding smaller reactive species such as metal centered clusters with well-defined, gas phase conditions also allows for detailed comparison between theory and experiments.

In these studies the main focus is to understand bond activation by transition metal cations and solvation of transition metal dications. The gas phase ions of interest are studied using an electrospray-ionization or laser-ablation dual time-of-flight mass spectrometer and are characterized using photofragment spectroscopy in the visible and ultraviolet regions of the spectrum. Photofragment spectroscopy is a powerful method that can be used in gas phase studies to gather a wealth of information on the ions' bond strengths, spectroscopic constants, and dissociation kinetics and dynamics.

The study of $\text{TiO}^+(\text{CO}_2)$ spectroscopy (Chapter 3) was a result of study of CO_2 bond activation by Ti^+ that went on to provide a wealth of information on the spectroscopy and dissociation kinetics of this molecule. An electronic transition of the TiO^+ chromophore was observed, ${}^2\Pi \leftarrow {}^2\Delta$, revealing new information about the excited state and the effect of TiO^+ electronic state on the metal- CO_2 ligand interaction. The photodissociation spectrum of this molecule is well resolved and shows progressions in the covalent Ti-O stretch and metal-ligand stretch and rock. The lifetime of electronically excited $\text{TiO}^+(\text{CO}_2)$ was measured, and depends strongly on vibrational energy. Calculations on TiO^+ and $\text{TiO}^+(\text{CO}_2)$ were combined with experimental results on $\text{TiO}^+(\text{CO}_2)$ to predict spectroscopic transitions of TiO^+ , an astrophysically interesting molecule.

The photodissociation dynamics of $\text{M}^{2+}(\text{CH}_3\text{CN})_n(\text{H}_2\text{O})_m$ where $\text{M} = \text{Co}$ and Ni , (Chapter 4) is important in understanding the gas phase microsolvation of metal

dications. The coordination number and type of solvent affect the dissociation pathways. $M^{2+}(\text{CH}_3\text{CN})_n$ ($n > 2$) primarily lose a solvent molecule. Electron transfer is a minor channel for $n=3$ and is the only channel observed for $n=2$. Mixed clusters $M^{2+}(\text{CH}_3\text{CN})_n(\text{H}_2\text{O})_m$ preferentially lose water. Loss of acetonitrile is a minor channel, as is proton transfer. Water is the proton donor. Replacing acetonitrile with water increases the proton transfer channel. Nickel and cobalt complexes show similar dissociation dynamics, with proton transfer more likely for nickel complexes.

Methane activation by transition metal catalysts is industrially important as it can be used to produce gasoline from natural gas. We studied the products and intermediates of the reaction of laser-ablated platinum atoms with methane (Chapter 5). Photoionization efficiency curves were measured for PtCH_2 and the $[\text{H-Pt-CH}_3]$ insertion intermediate using tunable vacuum ultraviolet light. The resulting ionization energies were combined with bond strengths for the cations to derive bond strengths for the neutrals. These were used to construct a potential energy surface for methane activation by platinum atoms.

TABLE OF CONTENTS

	Page
ACKNOWLEDGMENTS.....	v
ABSTRACT	viii
LIST OF CONTENTS.....	xi
LIST OF TABLES	xv
LIST OF FIGURES	xvii
CHAPTER 1: INTRODUCTION.....	1
1.1 Introduction	1
1.2 Motivation.....	3
1.2.1 Solvation of Dications.....	4
1.2.2 Motivation for Bond Activation Studies	6
1.2.3 Astronomically Interesting Transition Metal Complexes	8
1.3 The Photodissociation Process.....	9
1.4 Time-of-Flight (TOF) Profile	12
1.4.1 Kinetic Energy Release (KER).....	13
1.4.2 Dissociation Lifetimes and Rates	17
1.5 Overview	19
1.6 References	20

CHAPTER 2: EXPERIMENTAL	23
2.1 Experimental Approach	23
2.2 ESI Apparatus Description	25
2.2.1 Ion Production and First Differential Region	25
2.2.2 Modifications to the First Differential Region.....	27
2.2.3 Second and Third Differential Regions	30
2.2.4 Last Differential Region	31
2.2.5 Detector Region.....	32
2.2.6 Data Processing and Experimental Timing.....	35
2.3 Ablation Apparatus.....	36
2.4 Advanced Light Source Ablation Apparatus Description.....	39
2.5 Experimental Timing.....	41
2.5.1.1 Electrospray Ionization Instrument.....	41
2.5.1.2 Ablation Instrument	42
2.5.2 Arrival Time Calculations	43
2.6 References	44
CHAPTER 3: PHOTOFRAGMENT SPECTROSCOPY OF $\text{TiO}^+(\text{CO}_2)$	46
3.1 Introduction	46
3.2 Experimental	51
3.3 Results and Discussion.....	52

3.3.1 Photodissociation Spectroscopy and Dissociation Kinetics of TiO ⁺ (CO ₂)	52
3.3.2 Calculations.....	60
3.4 Discussion.....	64
3.5 Conclusion.....	68
3.6 References	69
CHAPTER 4: MICROSOLVATION OF Ni ²⁺ AND Co ²⁺ BY ACETONITRILE AND WATER: PHOTODISSOCIATION DYNAMICS OF M ²⁺ (CH ₃ CN) _n (H ₂ O) _m	
4.1 Introduction	72
4.2 Experimental Approach.....	75
4.3 Results.....	78
4.3.1 Photodissociation Dynamics of Co ²⁺ Complexes.....	81
4.3.1.1 Four Coordinate Complexes	81
4.3.1.2 Three Coordinate Complexes.....	89
4.3.1.3 Two Coordinate Complexes	92
4.3.2 Photodissociation Dynamics of Ni ²⁺ Complexes	94
4.3.2.1 Photodissociation Yield of Four Coordinate Complexes	94
4.3.2.2 Photodissociation Yield of Three Coordination Complexes	99
4.3.2.3 Photodissociation Yield of Two Coordinate Complexes	100
4.3.3 Wavelength Dependence	100
4.4 Discussion.....	101
4.4.1 Geometry of the Metal Dication Clusters	101

4.4.2 Homogeneous Acetonitrile Clusters.....	102
4.4.3 Photodissociation Dynamics of $M^{2+}(CH_3CN)_n(H_2O)_m$ Clusters	104
4.4.3.1 Simple Solvent Loss Pathway.....	104
4.4.3.2 Electron Transfer Pathway.....	105
4.4.3.3 Proton Transfer Pathway	105
4.4.4 Influence of Metal	107
4.5 References	108
CHAPTER 5: IONIZATION ENERGIES OF PtC_nH_m AND A POTENTIAL ENERGY SURFACE FOR THE $Pt + CH_4$ REACTION	110
5.1 Introduction	110
5.2 Experimental	113
5.3 Results.....	116
5.4 Discussion.....	122
5.4.1 Potential Energy Surface for Methane Activation by Platinum.....	122
5.4.2 Experimental and Theoretical Studies of Methane Activation by Pt Atoms.....	126
5.4.3 Methane Activation by Platinum Cation.....	128
5.4.4 Effect of Charge on Methane Activation by Platinum.....	130
5.5 References	132
CHAPTER 6: CONCLUSIONS AND FUTURE WORK.....	134
6.1 Conclusions	134
6.1.1 Photofragment Spectroscopy of $TiO^+(CO_2)$	134

6.1.2	Microsolvation of Ni ²⁺ and Co ²⁺ by Acetonitrile and Water: Photodissociation Dynamics of M ²⁺ (CH ₃ CN) _n (H ₂ O) _m	136
6.1.3	Ionization Energies of PtC _n H _m and a Potential Energy Surface for the Pt + CH ₄ Reaction	138
6.2	Future Work on the Electrospray Ionization Instrument	140
6.2.1	Electronic Spectroscopy	140
6.2.1.1	Electronic Spectroscopy of M ²⁺ (solvent) _n for M= Ni and Co at 80 K	141
6.2.1.2	Electronic Spectroscopy of Cu ²⁺ (H ₂ O) _n at 80 K	144
6.2.2	Vibrational Spectroscopy	145
6.2.2.1	Vibrational Spectroscopy of Cu ²⁺ (H ₂ O) _n and Co ²⁺ (CH ₃ CN) _n Clusters	146
6.2.2.1	Vibrational Spectroscopy of Metal Dication – Polypeptide Complexes	148
6.3	References	150
	BIBLIOGRAPHY	152

LIST OF TABLES

Table	Page
1.1	Physical properties of acetonitrile and water..... 5
2.1	Timing constants are unique to each instrument and also allow finding the appropriate mass using arrival time of the ions 43
3.1	Excited state lifetimes for several vibronic states of $\text{TiO}^+(\text{CO}_2)$. The lifetimes are measured from fits to tailing in the TiO^+ fragment time-of-flight spectrum, as shown in figure 3.5 58
3.2	Spectroscopic parameters for the ground and low-lying excited states of TiO^+ from TD-DFT calculations at the B3LYP/6-311+G(d) level. The first row is a harmonic frequency. Other rows are anharmonic frequencies from the potentials in figure 3.6. All values in cm^{-1} 62
3.3	Spectroscopic parameters for the ground and low-lying excited states of $\text{TiO}^+(\text{CO}_2)$ from TD-DFT calculations at the B3LYP/6-311+G(d) level. The first row is a harmonic frequency. Other rows are anharmonic frequencies from the potentials in Figure 6. All values in cm^{-1} . Electronic states of $\text{TiO}^+(\text{CO}_2)$ are also labeled by the corresponding state of bare TiO^+ in parentheses. Interaction with CO_2 splits the ^2P state into two components. Parameters are not given for the upper $^2\text{A}''(^2\text{P})$ state..... 63
3.4	Calculated vibrational frequencies of ground state $\text{TiO}^+(\text{CO}_2)$ at the B3LYP/6-311+G(d) level..... 63
4.1	The physical properties of acetonitrile and water show that acetonitrile is a better solvent for gas phase cations 75
4.2	Energies for the dissociation reactions of $\text{M}^{2+}(\text{CH}_3\text{CN})_n(\text{H}_2\text{O})_m$ clusters 95
4.3	Normalized photodissociation yields are compared for homogeneous clusters of both metals at 532 nm 96

4.4	Four coordinate clusters of $M^{2+}(CH_3CN)_n(H_2O)_m$ where $M = Co$ and Ni , normalized photodissociation yield for simple solvent loss at the maximum absorption wavelength	96
4.5	Three coordinate clusters of Ni and Co , $M^{2+}(CH_3CN)_n(H_2O)_m$, normalized photodissociation yield at 532 nm	97
5.1	Ionization energies and bond strengths for platinum containing compounds at 0 K. Cation values are from Armentrout and co-workers ⁵ and Pt-H neutral bond strength from Brooks and co-workers	126

LIST OF FIGURES

Figure	Page
1.1	Schematic depiction of photodissociation via two different processes: (a) direct and (b) indirect..... 10
1.2	Schematic of two potential energy profiles (a) without (b) with a reverse activation barrier. In part (b), two diabatic potentials are shown above the adiabatic potential..... 15
1.3	The time-of-flight profile of two fragments with different kinetic energy releases. The dip in middle is due to fragments with high velocity perpendicular to the ion beam missing the detector 16
1.4	TOF profile of TiO^+ fragment from photodissociation of $\text{TiO}^+(\text{CO}_2)$ at two photon energies. Tailing at lower energy is due to slow photodissociation (~ 1100 ns lifetime) 18
2.1	Schematic drawing of the electrospray ionization dual time-of-flight mass spectrometer apparatus that was used for $\text{M}^{2+}(\text{CH}_3\text{CN})_n(\text{H}_2\text{O})_m$ study 26
2.2	Schematics of (a) tube lens and (b) an ion funnel that are used for ion transmission and to create a concentrated ion beam..... 29
2.3	Side view of the reflectron. The turning point for the ions is shown with a cross..... 34
2.4	Experimental timing for the electrospray ionization dual time-of-flight apparatus. The timings given are for $\text{Co}^{2+}(\text{CH}_3\text{CN})_4$ 37
2.5	Schematic drawing of the laser ablation dual time-of-flight mass spectrometer apparatus that was used for the $\text{TiO}^+(\text{CO}_2)$ study..... 38
3.1	Molecular orbital diagram and electron occupancy of TiO^+ ($X, {}^2\Delta$) 49

3.2	Photodissociation spectrum of $\text{TiO}^+(\text{CO}_2)$ with the covalent Ti-O stretch vibrational quantum numbers ν_{TiO} marked. The asterisk denotes the electronic state origin	53
3.3	Assignment of covalent Ti-O stretch vibrational levels ν_{TiO} in the photodissociation spectrum of $\text{TiO}^+(\text{CO}_2)$. Experimental isotope shifts are compared to calculated shifts assuming the vibrational numbering is as shown in Fig. 2 (solid line) and with the numbering shifted by one (dashed lines).....	55
3.4	Overlapped photodissociation spectrum of $\text{TiO}^+(\text{CO}_2)$. Bands corresponding to the covalent Ti-O stretch $\nu_{\text{TiO}} = 0$ to 4 are shifted to allow comparison of the low-frequency metal- CO_2 stretch and rock. The low-frequency vibrations are essentially independent of ν_{TiO}	57
3.5	Time-of-flight spectra of TiO^+ from photodissociation of $\text{TiO}^+(\text{CO}_2)$ at 14204 and 14925 cm^{-1} . Tailing in the 14204 cm^{-1} spectrum indicates a lifetime of 1100 ns, which drops to 120 ns at 14925 cm^{-1} . The small peaks in the spectra are due to photodissociation of minor isotopomers	59
3.6	Calculated potential energy curves for doublet states of TiO^+ and $\text{TiO}^+(\text{CO}_2)$ along the covalent Ti-O stretch. Points are calculated using TD-DFT at the B3LYP/6-311+G(d,p) level. Electronic states of $\text{TiO}^+(\text{CO}_2)$ are also labeled by the corresponding state of bare TiO^+	61
4.1	(a) Mass spectrum of $\text{Co}^{2+}(\text{CH}_3\text{CN})_n(\text{H}_2\text{O})_m$ clusters (b) Mass spectrum of $\text{Ni}^{2+}(\text{CH}_3\text{CN})_n(\text{H}_2\text{O})_m$. The peaks consist of doublets due to the two major isotopes of nickel, ^{58}Ni and ^{60}Ni , which are separated by one m/z unit as shown above.....	80
4.2	Difference spectra for $\text{Co}^{2+}(\text{CH}_3\text{CN})_4$ (top) and $\text{Ni}^{2+}(\text{CH}_3\text{CN})_4$ (bottom) at 532 nm. The fragment is due to simple solvent acetonitrile loss	82
4.3	Difference spectra for $\text{Co}^{2+}(\text{CH}_3\text{CN})_3(\text{H}_2\text{O})$ (top) and $\text{Ni}^{2+}(\text{CH}_3\text{CN})_3(\text{H}_2\text{O})$ (bottom) at 532 nm. The fragment is due to simple solvent, water, loss.....	84

4.4	Difference spectrum for $\text{Co}^{2+}(\text{CH}_3\text{CN})_2(\text{H}_2\text{O})_2$ shows three dissociation pathways. The major channel is solvent water loss. Loss of solvent acetonitrile and proton transfer are minor channels.....	85
4.5	As seen in the difference spectra of (a) $\text{Co}^{2+}(\text{CH}_3\text{CN})_2(\text{H}_2\text{O})_2$ and (b) $\text{Ni}^{2+}(\text{CH}_3\text{CN})_2(\text{H}_2\text{O})_2$ the minor pathways yields are different. $\text{Ni}^{2+}(\text{CH}_3\text{CN})_2(\text{H}_2\text{O})_2$ favors proton transfer while $\text{Co}^{2+}(\text{CH}_3\text{CN})_2(\text{H}_2\text{O})_2$ prefers acetonitrile loss.....	86
4.6	The minor fragmentation pathways, proton transfer and acetonitrile loss, are shown for (a) $\text{Co}^{2+}(\text{CH}_3\text{CN})_2(\text{H}_2\text{O})_2$ and (b) $\text{Co}^{2+}(\text{CD}_3\text{CN})_2(\text{H}_2\text{O})_2$. This was used to identify the proton donor to be water and not acetonitrile.....	87
4.7	Difference spectra of three coordinate clusters (a) $\text{Co}^{2+}(\text{CH}_3\text{CN})_3$ and (b) $\text{Ni}^{2+}(\text{CH}_3\text{CN})_3$. The common fragmentation pathway is acetonitrile loss (major). The electron transfer channel is unique for Ni^{2+} cluster	90
4.8	Difference spectra of (a) $\text{Co}^{2+}(\text{CH}_3\text{CN})_2(\text{H}_2\text{O})$ and (b) $\text{Ni}^{2+}(\text{CH}_3\text{CN})_2(\text{H}_2\text{O})$. The common fragmentation pathways are water loss (major) and proton transfer.....	91
4.9	Difference spectra of (a) $\text{Co}^{2+}(\text{CH}_3\text{CN})_2$ and (b) $\text{Ni}^{2+}(\text{CH}_3\text{CN})_2$. Dissociation occurs via electron transfer	93
4.10	Difference spectrum for $\text{Ni}^{2+}(\text{CH}_3\text{CN})_2(\text{H}_2\text{O})_2$ shows three dissociation pathways: proton transfer and solvent (major: water, very minor: acetonitrile) loss.....	98
4.11	Shvartsburg and coworkers have above fragmentation pathways for doubly charged metals such as Be, Mg, Ca, Sr, Ba, Zn, Cd, Mn, Fe, Co, Ni and Cu with acetonitrile. ¹³ Collision energies range from 40 – 160 eV	103
5.1	The ablation reflectron time-of-flight instrument used at the ALS is shown above. The VUV light irradiates the molecular beam at the center of the ion optics as shown (courtesy of Dr. Musa Ahmed, Lawrence Berkeley National Lab).....	114

5.2	The mass spectrum of the ionized products from the reaction of laser-ablated platinum with CD ₄ at 11 eV. The enlarged portion shows the assignment of the PtCD _n peaks	117
5.3	The mass spectrum of the ionized products from the reaction of laser-ablated platinum with CH ₄ at 11 eV. The enlarged portion shows the assignment of the PtCH _n peaks	119
5.4	The ionization energy onset for ¹⁹⁵ PtCH ₂ made via reaction of methane with platinum. The vertical line shows the ionization energy of 8.78 eV ..	120
5.5	The ionization energy onset for the insertion intermediate, H- ¹⁹⁵ Pt-CH ₃ made via reaction of methane with platinum. The vertical line shows the ionization energy of 8.89 eV	121
5.6	Thermodynamic cycle used to calculate the bond dissociation energy of Pt-CH ₂	123
5.7	The potential energy surface for the reaction of methane with platinum. Values in parenthesis are based on calculations.....	125
5.8	Comparison of Pt ⁺ + CH ₄ reaction with Pt + CH ₄ reaction.....	129
6.1	Total photodissociation spectrum of Co ²⁺ (H ₂ O) ₆ and the absorption spectrum of Cobalt (II) in aqueous solution	142
6.2	Spectral resolution is greatly improved by lowering the internal energy of the ions. The vibration energy calculations were done on Zn ²⁺ (H ₂ O) ₆	143
6.3	Structures and calculated IR spectra of two possible structures of Cu ²⁺ (H ₂ O) ₆ . Arrows and solid bars indicate the calculated positions and intensities for bare H ₂ O	147

CHAPTER 1

INTRODUCTION

1.1 Introduction

Photodissociation spectroscopy was revealed as a useful experimental technique in the early 60's. It is particularly useful in cases where it is hard to obtain an absorption spectrum.¹ Photodissociation requires that the molecules absorb light and dissociate. Hence, the intensity of the features in the photodissociation spectrum is the product of the absorption cross-section and the dissociation probability of the excited molecules. Directly measuring absorption spectra of transient molecules is challenging due to the very low concentrations of molecules typically present. Indirect measurements offer the potential for improved sensitivity. Photofragment spectroscopy is particularly well suited to studying ions. Parent ions can be mass selected and fragment ions can be distinguished and detected with exquisite sensitivity using mass spectrometry. We use gas-phase photofragment spectroscopy to study ion structure and non-covalent metal ion-ligand interactions in controlled surroundings.

Studies of ionic clusters have become an integral component in understanding microsolvation and catalysis by transition metal cations. Research on ion clusters in the gas phase has emerged as a very active field in chemistry and physics during the

last decade. This wide interest is due to two reasons: the possibility of bridging the gap between the condensed and gas phases by developing our understanding of clusters and the possibility that small clusters can have unique chemical and catalytic properties.

Understanding smaller reactive species such as metal centered clusters in the gas phase with well-defined conditions allows for detailed comparison between theory and experiments. This is more challenging in condensed phase studies because it is hard to accurately model interactions of the bulk solvent molecules with the charged metal center.² However, in the gas phase, the number and type of solvent molecules interacting with a metal center can be controlled.

Most of the studies conducted on gas phase ions have focused on singly charged cations. But with Fenn's introduction of the electrospray ionization technique multiply charged ions can be produced in sufficient concentrations for detailed studies.³ The higher charge on the metal leads to very strong interaction with inner-shell solvent molecules. For example, the first six water molecules bond to M^{2+} by an average of ~ 60 kcal/mol, giving 75% of the bulk free energy of solvation.^{4,5} Gas phase studies of small, microsolvated clusters provide a unique opportunity to study very strong non-covalent interactions. Research by Stace and co-workers has shown that smaller clusters are useful because they are too small to exhibit bulk behavior without ion solvation.⁶

1.2 Motivation

In our lab the main focus is to understand bond activation by transition metal cations and solvation of transition metal dications. The gas phase ions of interest are characterized using photofragment spectroscopy in the visible and ultraviolet regions of the spectrum. The solvation studies were conducted using Co^{2+} and Ni^{2+} as the metals and acetonitrile and water as solvents. This complements previous studies done by our lab with the same metal dications and water/methanol as solvents. Also, activation of methane by neutral platinum atoms, and the key insertion intermediate were studied via Photoionization. Transition metals hold interest far from our galaxy into the stars. One of the studies is of significant importance for astronomy because it can aid the investigation of potential molecular ions present in cool M-type stars by observing and characterizing excited states of TiO^+ . Since we don't have enough photon energy to efficiently break the TiO^+ bond, we use a spy molecule, CO_2 , to understand the electronic spectroscopy of TiO^+ by studying $\text{TiO}^+(\text{CO}_2)$. The electrostatic bond between the metal oxide cation and ligand requires very little energy to break. So this technique has become one of the common methods to understand molecular spectroscopy indirectly.^{7,8} Typically spy molecules are used to obtain vibrational spectra of ions where one IR photon does not have enough energy to break a covalent bond. The first studies of this type attached H_2 to protonated

water clusters to measure the O-H stretching vibrations.⁷ In recent studies a rare gas atom, typically Ar is used as the spy instead.^{9,10}

1.2.1 Solvation of Dications

Transition metals are known for their colorful character. The color is determined by the interaction of the metal compound or ion with solvent molecules or ligands. Thus, the change in energy of the d-orbitals due to the solvent splitting the degeneracy of the orbitals into higher and lower energy states is reflected in the color of light the metal species is able to absorb. In recent years, research on microsolvation of transition metal clusters has expanded dramatically due to advances in experimental techniques. Previously, the major part of our understanding was limited to singly charged species because multiply charged species were impossible to produce in the gas phase.¹¹ Transition metals are usually multiply charged in solution.⁶ Hence, understanding these states is of importance in chemistry and biology. The introduction of electrospray ionization by Fenn and co-workers opened doors to a new era in studying multiply charged ions and their chemistry in the gas phase.³ Studies of microsolvated, multiply charged transition metal ions offer insight into solvation of these important species by measuring their thermochemical properties, excited electronic states, coordination and structure.^{2,12-14} Gas phase studies offer complete control over solvent and coordination number, which is simply not possible in the condensed phase.

These studies focus on acetonitrile and water as the solvent molecules. Acetonitrile is a polar, aprotic solvent which has become a good prototype due to its widespread use as a non-aqueous solvent. At present acetonitrile is primarily emitted from biomass burning.¹⁵ This leads to its importance in atmospheric and marine chemistry as well as biological sciences. Also, acetonitrile has a higher dipole moment and polarizability (α) than water as shown in table 1.1. Thus, acetonitrile is a better solvent for isolated M^{2+} than water. Studies of M^{2+} microsolvated by acetonitrile and water provide a wealth of information on aprotic vs. protic molecule competition for the solvation of the transition metal dication, and on how the nature of the solvent affects the stability and dissociation dynamics of the cluster. There have been two studies of fragments produced from $M^{2+}(\text{CH}_3\text{CN})_n$ by collision induced dissociation (CID).^{13,16,17} Our work uses photons to excite the molecules which provides better control over the energy. Also, we will study mixed acetonitrile water clusters.

Ligand	IE (eV)	μ (D)	α (\AA^3)
Water	12.62	1.8	1.4
Acetonitrile	12.19	3.9	4.4

Table 1.1: Physical properties of acetonitrile and water.

1.2.2 Motivation for Bond Activation Studies

Transition metals are known to form the best catalysts. For example, nickel is a hydrogenation catalyst that is used to make partially hydrogenated vegetable oil which has a higher melting point and is less reactive. Also, platinum and rhenium are vital in industry for production of high octane gasoline. They perform better as catalysts due to their multiple oxidation states and ability to provide alternative lower overall activation energy route in reactions. Understanding the particular character of these transition metals, and mechanism for bond activation reactions, is critical for developing more efficient catalysts for industry.

In the late 70's Allison, Freas and Ridge first studied C-H and C-C bond activation by gas phase transition metal ions.¹⁸ Many subsequent studies showed that gas phase transition metal cations are very reactive, and are able to activate H-H, C-H and C-O bonds, often with surprising selectivity.¹⁹⁻²⁵ The ability of gas phase studies to provide quantitative information on these transition metal cation species leads to well-characterized reaction mechanisms and energies of the reactions.^{22,26} These studies have provided the electronic requirement for covalent bond activation by metal cations without interference from solvents or stabilizing ligands. However, the mechanisms for the reactions of neutral metal atoms ^{24,27-29} are not as well characterized due to challenges faced in the experimental approach. This makes the

study of neutrals extra important, and it quantifies how charge affects the reaction energetics and mechanism.

Accurate computational studies can help to establish reaction mechanisms and develop new catalysts. Theory on transition metals tends to be challenging due to the number of electrons, spin contamination and relativistic effects.³⁰ Accurate data on relatively simple, yet relevant systems such as platinum cation with methane provide an ideal benchmark for computational studies. Platinum is an all purpose catalyst and highly studied transition metal^{27,28} and metal cation.^{22,23,30} Methane is the major (~80%) component of natural gas, a resource of which the US has extensive supplies. Methane can be used to produce larger hydrocarbons that then can be used in the gasoline industry to make highly branched hydrocarbons, but current catalysts for methane activation have poor conversion and selectivity. So, the activation of methane by platinum becomes an important system not only for intrinsic interest but also for industrial applications.

One of the studies we have done is to examine methane activation by neutral platinum. The thermochemistry of intermediates and products of methane activation by platinum cation is known.²² Measuring their ionization energies will allow us to determine energetics for the corresponding neutral reaction, from which we can learn about the reaction mechanism.

1.2.3 Astronomically Interesting Transition Metal Complexes

The middle region of the photosphere of cool stars contains certain diatomic 3d oxide molecules. In cool red M-type stars, the dominant diatomic molecule is titanium oxide.³¹ Due to its importance in astrophysics, TiO is one of the most studied transition metal containing diatomics. It has strong electronic absorption bands in the visible spectrum with resolvable rotational structure. These spectral features are used to classify these stars in the MK system and the rotational structure is used as a thermometer.³² Unlike other types of stars, cooler M stars emit very little UV radiation throughout their very long lifetimes. This factor works in favor of molecule production near M stars. The TiO bond dissociation energy is slightly higher than its ionization energy making it a likely diatomic candidate to donate free electrons into the pool of electrons in these stars. However, for astronomers to observe TiO⁺, its electronic spectroscopy needs to be characterized.

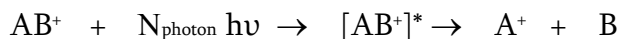
The only excited state of TiO⁺ known experimentally is the ²Σ state from photoelectron spectroscopy of TiO studied by Weisshaar and coworkers.³³ Transitions to this state from the ²Δ TiO⁺ ground state are forbidden, making this excited state useless for astronomical observations. Astrophysicists and chemists have used theory to study TiO⁺, but, to date, these calculations are at too low a level to be very helpful.³⁴ Therefore, there is much interest in the electronic spectroscopy of the titanium oxide cation in the visible region of the spectrum. In our lab, we have

studied the $\text{TiO}^+(\text{CO}_2)$ molecule to look into TiO^+ electronic spectroscopy. With the photon energy available in our lab, we are unable to photodissociate the TiO^+ bond. However, using a spy molecule, carbon dioxide, we are able to study photofragment spectroscopy of $\text{TiO}^+(\text{CO}_2)$ to understand the electronic states of TiO^+ as well as to explore how the TiO^+-CO_2 interaction depends on the electronic state of TiO^+ . Since the carbon dioxide can slightly perturb the TiO^+ , theory is useful in inferring the properties of bare TiO^+ from studies of $\text{TiO}^+(\text{CO}_2)$.

1.3 The Photodissociation Process

The main technique that is utilized in our lab is photofragment spectroscopy. Photofragment spectroscopy is a form of action spectroscopy. When the charged molecule absorbs a photon and dissociates, what is monitored is the fragment that was produced due to the photon energy. The yield of the fragment is an indirect measurement of the absorption of a photon. The spectrum that results from observing a fragment over a range of energies is the photodissociation spectrum.

Figure 1.1 depicts a typical photodissociation process. The parent, AB^+ , absorbs the photon energy provided to promote it to an excited state, $[\text{AB}^+]^*$. If this leads to dissociation the following fragments would be observed:



where N_{photon} is the number of absorbed photons with energy $h\nu$. This is only possible

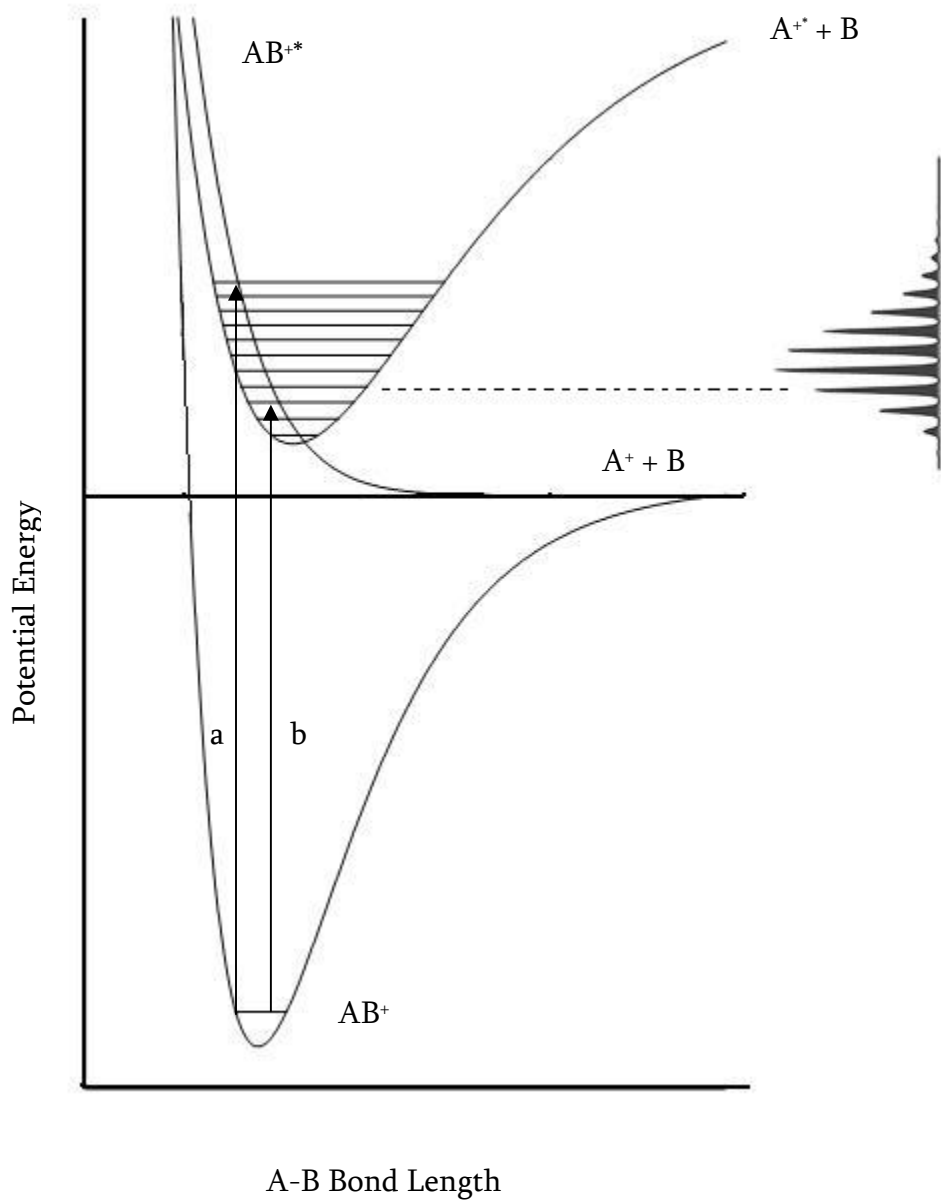


Figure 1.1: Schematic depiction of photodissociation via two different processes: (a) direct and (b) indirect.

under certain conditions. The molecules must absorb the photon to produce $[AB^+]^*$, the photon should have ample amount of energy to dissociate the bond to produce A^+ fragment and there must be a non-zero quantum yield for the dissociation to observe a peak on the spectrum. Basic photofragmentation involves a single photon which is shown throughout these studies. However, multi-photon techniques are common with photons of the same or different energy.

There are two types of photodissociation, direct and indirect, which are shown in figure 1.1. Direct dissociation is simple and the fragmentation does not depend on dynamic limitations such as energy barriers. When the parent ion is excited to a higher energy state, fragmentation results due to the potential being repulsive along the reaction coordinate. This is a rapid process, so the excited state lifetime tends to be very short and the spectral features are limited. But the upper limit of the bond strength can be found from the dissociation threshold.³⁵

Indirect dissociation is slightly complicated since it involves two separate steps leading to fragmentation. The initial step is the absorption of a photon to promote the parent ion into an excited state. The second step is the fragmentation which is challenged by dynamic constraints such as energy barriers. This is not a quick dissociation process since it needs to overcome the barrier. It is necessary either to tunnel through the barrier, redistribute the internal vibrational energy or avoid it completely by crossing to another nearby electronic state (internal conversion) to dissociate.

Photodissociation, as described in our studies, is due to the crossover to a lower lying state above the dissociation limit via internal conversion. Indirect photodissociation that leads to long-lived excited states (“pre-dissociation”) yields more information regarding the parent ion such as vibrational frequencies of the excited and sometimes ground electronic states, and even bond lengths. The $\text{TiO}^+(\text{CO}_2)$ spectrum (Chapter 3) is a good example of indirect photodissociation via internal conversion to the ground state. The electronic spectrum has resolved vibrational structure, and the excited state lifetime depends on the vibration energy in the excited state. The study of solvated M^{2+} is an example of indirect photodissociation via internal conversion to the ground state. The fragment time-of-flight profile is sensitive to the lifetime of the excited state and to the kinetic energy release in the dissociation.

1.4 Time-of-Flight (TOF) Profile

The instruments that were used for all the studies are dual reflectron time-of-flight mass spectrometers. They are discussed in detail in Chapter 2. Each differentiates according to the source region: ablation or electrospray ionization TOF mass spectrometer. Initially the parent mass is selected and then the photofragmentation takes place at the turning point of the reflectron. The second portion is where the fragment and the depleted parent are monitored and identified

according to their arrival flight time. In addition, from the fragment TOF profile, we can get information about the dynamics and kinetics of the fragmentation.

The $\text{TiO}^+(\text{CO}_2)$ studies were done using the laser ablation dual TOF. The TiO^+ fragment TOF profile provided useful information on the lifetime of the excited state of $\text{TiO}^+(\text{CO}_2)$. The solvation of Co and Ni dications by acetonitrile and water studies used the ESI apparatus. The TOF profile reveals the kinetic energy release (KER) in the dissociation.

1.4.1 Kinetic Energy Release (KER)

To study photodissociation, a photon should excite a molecule from a lower energy state to a higher electronic state and the excited molecule should ultimately dissociate due to the upper electronic state's potential being repulsive along the intermolecular coordinates. When the photon energy exceeds the bond dissociation energy, the excess energy will partition to other modes such as translational energy and internal energy of the fragments.

$$E_{\text{excess}} = E_{\text{photon}} - D_0 = E_{\text{trans}} + E_{\text{internal}}$$

where D_0 is the bond dissociation energy and the E_{internal} is a combination of vibrational, rotational and electronic energies of the fragments.

The kinetic energy release (KER) is the energy that is released as the translational energy of the departing fragments. The kinetic energy release depends on the potential energy surface and it reveals information on the transition state

structure and reverse reaction barrier.³⁶ Schematic of potential energy surfaces with different reverse barriers are shown in figure 1.2.

For example, the transition state of simple bond cleavage is similar to the products (“loose”), which leads to little kinetic energy release (figure 1.2 a). So there is no reverse activation barrier because the transition state does not need rearrangement to lead to products. So the resulting TOF profile is a narrow fragment peak. This is what we observe for simple solvent loss from microsolvated M^{2+} .

However, a “tight” transition state involves substantial rearrangement in going from reactants to products. There is a substantial reverse activation barrier. The internal energy is not re-distributed among the degrees of freedom of the tight transition state as in the loose transition state. As a result often the reverse reaction barrier will end up as KER. The KER will be observed in the fragment peak shape. In cases where a doubly charged parent ion dissociates to form two singly charged fragments there is a substantial reverse activation barrier. This is a result of coulombic repulsion between the singly charged fragments, and can give rise to large KER (figure 1.2 b). The peak broadening is caused by the large distribution of velocities of the fragment ions. Ions with KER parallel to the beam direction reach the detector first, while those anti parallel reach the detector last. Some charged fragments dissociate perpendicular to the beam direction can completely miss the detector, giving a dip in the TOF profile as shown in figure 1.3. Modeling the peak profile allows us to measure the KER, providing insights into the reverse activation

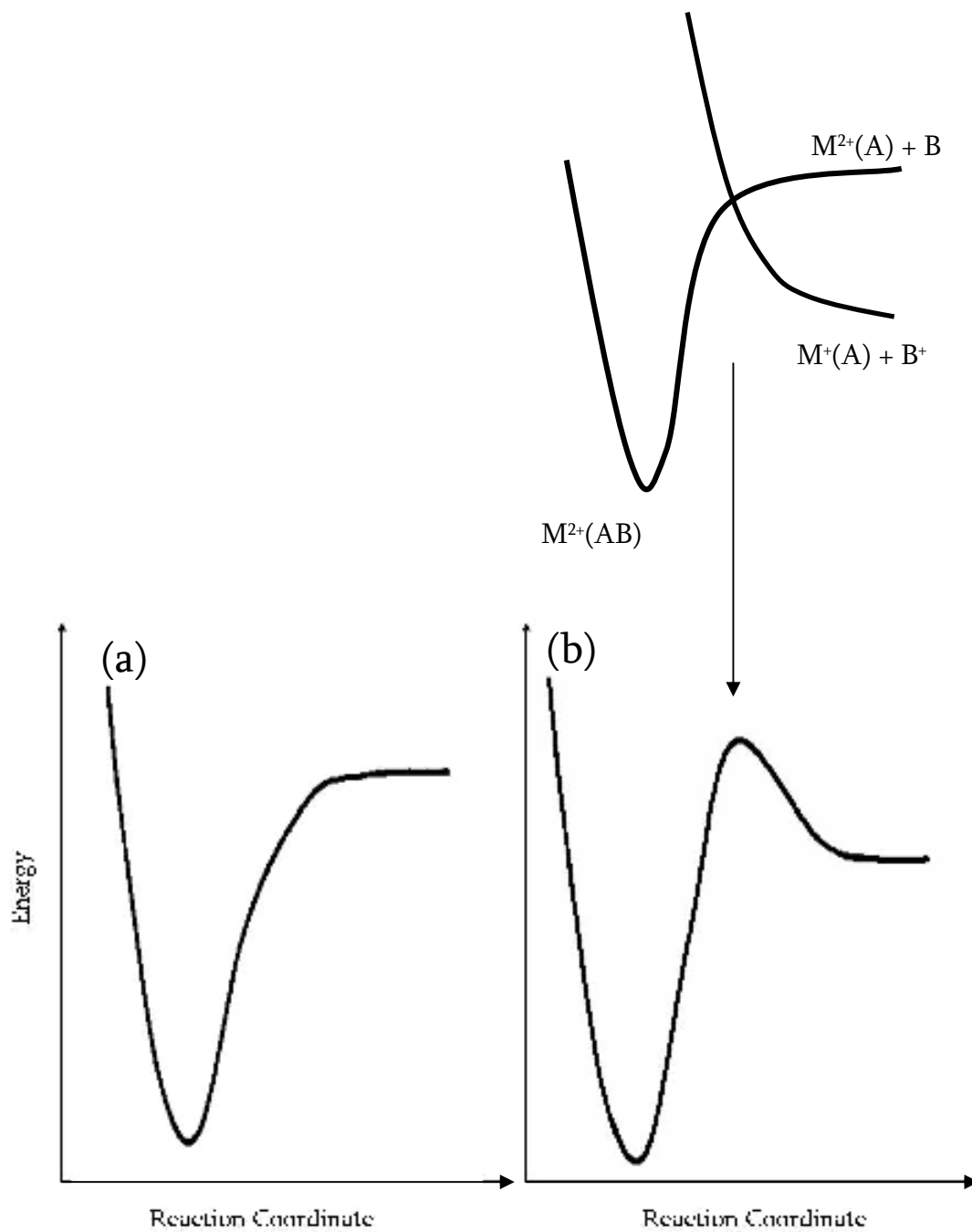


Figure 1.2: Schematic of two potential energy profiles (a) without (b) with a reverse activation barrier. In part (b), two diabatic potentials are shown above the adiabatic potential.

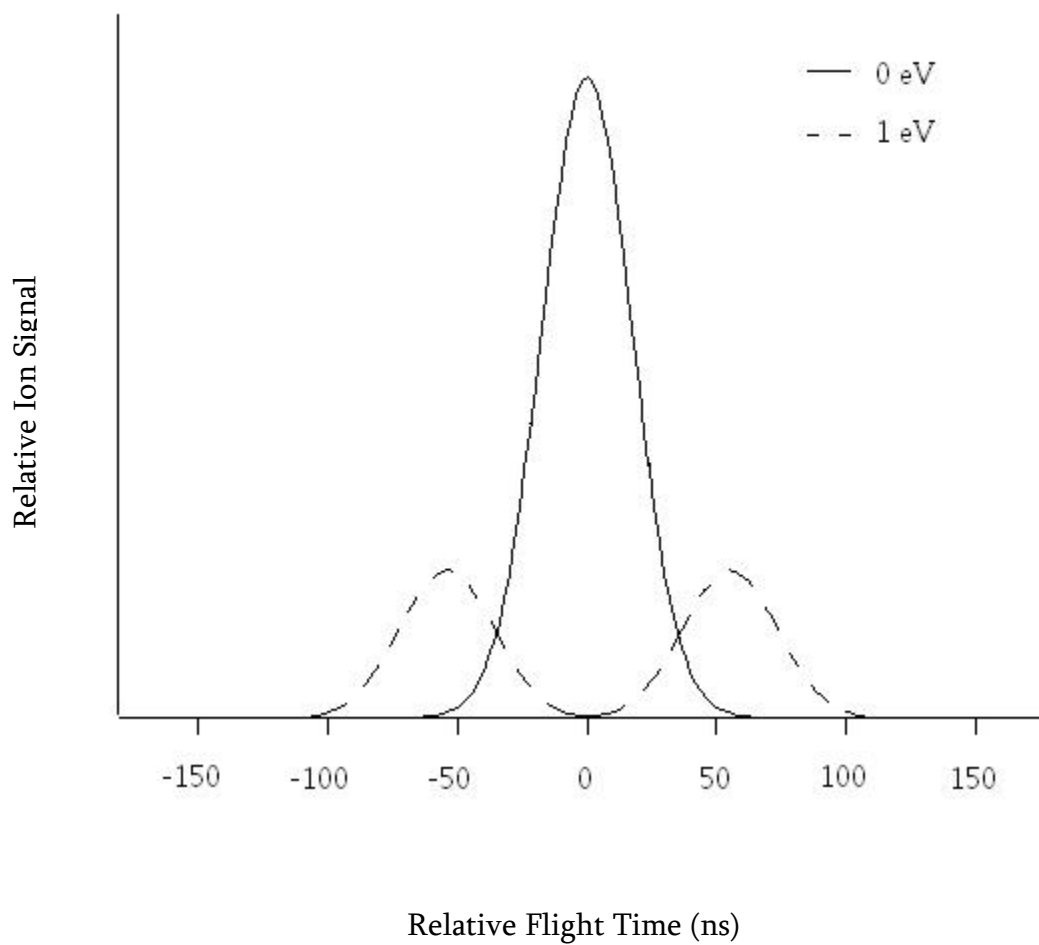


Figure 1.3: The time-of-flight profile of two fragments with different kinetic energy releases. The dip in middle is due to fragments with high velocity perpendicular to the ion beam missing the detector.

barrier and dissociation mechanism.

1.4.2 Dissociation Lifetimes and Rates

Another piece of useful information that is derived from the TOF mass spectrum is the dissociation rate of the molecules. The data are collected based on the flight times of the charged particles. If the fragmentation is rapid, all the parents will dissociate at the same time to produce the same mass charged fragment ions that reach the detector simultaneously, resulting in a narrow peak unless there is KER. If the photoexcited ion does not fall apart immediately, but remains excited for ≥ 50 ns, there is observable tailing of the fragment peak leading towards the parent mass. The study of $\text{TiO}^+(\text{CO}_2)$ showed excited state lifetimes which depend on the vibrational energy of the excited state. The tailing that was observed is shown in figure 1.4.

We measure the dissociation rate using a MathCAD program to iteratively simulate the shape of the fragment peak. However, there are limitations to the lifetimes we can measure in our lab. Ions that dissociate ≤ 50 ns show no tailing. Ions that dissociate after the reflectron have the same flight time as parent ions, and are thus not detected as fragments. This limits the maximum lifetime we can monitor to $\sim 1-5 \mu\text{s}$, depending on the mass of the parent.

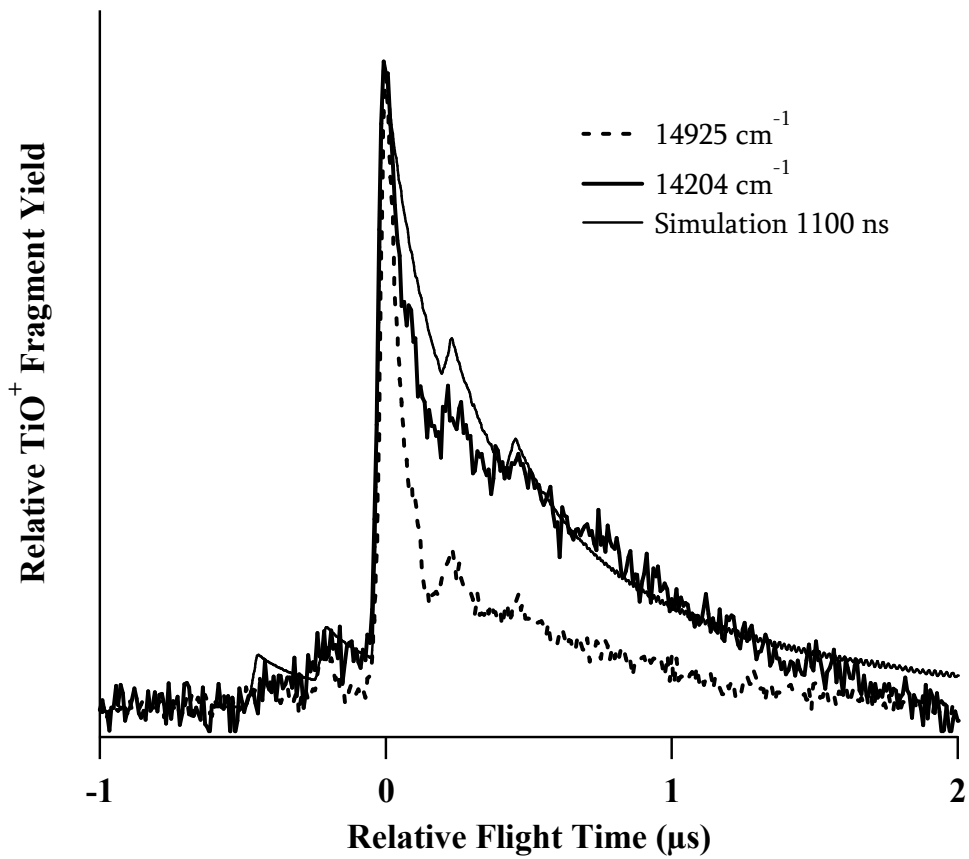


Figure 1.4: TOF profile of TiO⁺ fragment from photodissociation of TiO⁺(CO₂) at two photon energies. Tailing at lower energy is due to slow photodissociation (~1100 ns lifetime).

1.5 Overview

The instrumentation used in these studies is described in chapter 2, particularly modifications made to the electrospray instrument. Chapter 3 describes studies of the photofragment spectroscopy of $\text{TiO}^+(\text{CO}_2)$, which reveals information on the electronic spectroscopy of TiO^+ , as well as how electronic excitation of the TiO^+ affects the metal- CO_2 interaction. The studies of strong non-covalent interactions between metal dications and acetonitrile and water solvent molecules are described in chapter 4. Photofragment pathways reveal competition between solvent loss, proton transfer, and electron transfer and how this depends on the number and type of solvent molecules and the metal. Chapter 5 details photoionization studies of products and intermediates of the $\text{Pt} + \text{CH}_4$ reaction. The measured ionization energies and bond strengths for the cations are used to derive a potential energy surface for the reaction. Chapter 6 summarizes our results and describes future studies on our electrospray instrument.

1.6 References

- (1) Schinke, R. *Photodissociation Dynamics*, University Press: Cambridge, 1993.
- (2) Stace, A. J. *J. Phys. Chem. A* **2002**, *106*, 7993.
- (3) Yamashita, M.; Fenn, J. B. *J. Phys. Chem.* **1984**, *88*, 4451.
- (4) Blades, A. T.; Jayaweera, P.; Ikonomou, M. G.; Kebarle, P. *Int. J. Mass Spec. Ion Proc.* **1990**, *102*, 251.
- (5) Åkesson, R.; Pettersson, L. G. M.; Sandström, M.; Wahlgren, U. *J. Phys. Chem.* **1992**, *96*, 150.
- (6) Stace, A. J.; Walker, N. R.; Firth, S. *J. Am. Chem. Soc.* **1997**, *119*, 10239.
- (7) Okumura, M.; Yeh, L. I.; Meyers, J. D.; Lee, Y. T. *J. Chem. Phys.* **1986**, *85*, 2328.
- (8) Bellert, D.; Buthelezi, T.; Hayes, T.; Brucat, P. J. *Chem. Phys. Lett.* **1997**, *276*, 242.
- (9) Duncan, M. A. *Int. Rev. Phys. Chem.* **2003**, *22*, 407.
- (10) Hammer, N. I.; Diken, E. G.; Roscioli, J. R.; Johnson, M. A.; Myshakin, E. M.; Jordan, K. D.; McCoy, A. B.; Huang, X.; Bowman, J. M.; Carter, S. *J. Chem. Phys.* **2005**, *122*, Art. No. 244301.
- (11) Keese, R. G.; A. W. Castleman, J. *J. Phys. Chem. Ref. Data* **1986**, *15*, 1011.
- (12) Metz, R. B. *Int. J. Mass Spectrom.* **2004**, *235*, 131.
- (13) Kohler, M.; Leary, J. A. *Int. J. Mass Spectrom. Ion Proc.* **1997**, *162*, 17.
- (14) Rodriguez-Cruz, W. E.; Jockusch, R. A.; Williams, E. R. *J. Am. Chem. Soc.* **1998**, *120*, 5842.

- (15) Bange, H. W., Williams, J. *Atmospheric Environment* **2000**, *34*, 4959.
- (16) Shvartsburg, A. A.; Wilkes, J. G.; Lay, J. O.; Siu, K. W. M. *Chem. Phys. Lett.* **2001**, *350*, 216.
- (17) Kohler, M.; Leary, J. A. *J. Am. Soc. Mass Spectrom.* **1997**, *8*, 1124.
- (18) Allison, J.; Ridge, D. P. *J. Am. Chem. Soc.* **1979**, *101*, 4998.
- (19) Eller, K.; Schwarz, H. *Chem. Rev.* **1991**, *91*, 1121.
- (20) Böhme, D. K.; Schwarz, H. *Angew. Chem., Int. Ed. Engl.* **2005**, *44*, 2336.
- (21) Metz, R. B. *Adv. Chem. Phys.* **2008**, *138*, 331.
- (22) Zhang, X. G.; Liyanage, R.; Armentrout, P. B. *J. Am. Chem. Soc.* **2001**, *123*, 5563.
- (23) Irikura, K. K.; Beauchamp, J. L. *J. Phys. Chem.* **1991**, *95*, 8344.
- (24) Weisshaar, J. C. *Acc. Chem. Res.* **1993**, *26*, 213.
- (25) Koyanagi, G. K.; Bohme, D. K. *J. Phys. Chem. A* **2006**, *110*, 1232.
- (26) Parke, L. G., Hinton, C. S., Armentrout, P. B. *J. Phys. Chem. C.* **2007**, *111*, 17773.
- (27) Carroll, J. J.; Weisshaar, J. C. *J. Phys. Chem.* **1996**, *100*, 12355.
- (28) Carroll, J. J.; Weisshaar, J. C.; Siegbahn, P. E. M.; Wittborn, C. A. M.; Blomberg, M. R. A. *J. Phys. Chem.* **1995**, *99*, 14388.
- (29) Campbell, M. L. *J. Chem. Soc. Faraday Trans.* **1998**, *94*, 353.
- (30) Citir, M.; Metz, R. B.; Belau, L.; Ahmed, M. *J. Phys. Chem. A* **2008**, *112*, 9584.
- (31) Merer, A. J. *Ann. Rev. Phys. Chem.* **1989**, *40*, 407.

- (32) Burrows, A.; Dulick, M.; Bauschlicher, C. W., Jr.; Bernath, P. F.; Ram, R. S.; Sharp, C. M.; Milsom, J. A. *Astrophys. J.* **2005**, *624*, 988.
- (33) Sappey, A. D.; Eiden, G.; Harrington, J. E.; Weisshaar, J. C. *J. Chem. Phys.* **1989**, *90*, 1415.
- (34) McLaughlin, B. M.; Ballance, C. P.; Berrington, K. A. *J. Phys. B-At. Mol. Opt. Phys.* **2001**, *34*, L179.
- (35) Husband, J.; Aguirre, F.; Thompson, C. J.; Laperle, C. M.; Metz, R. B. *J. Phys. Chem. A* **2000**, *104*, 2020.
- (36) Laskin, J.; Lifshitz, C. *J. Mass Spectrom.* **2001**, *36*, 459.

CHAPTER 2

EXPERIMENTAL

2.1 Experimental Approach

All the work that is described in the following chapters has one experimental technique in common, the time-of-flight reflectron mass spectrometer. However, each project was uniquely differentiated by the source region such as the manner in which the molecules or ions of interest were produced.

The solvation study (Chapter 4) utilizes electrospray ionization (ESI) to produce multiply charged metal centered clusters.¹ Then the ions are introduced to the vacuum through a heated desolvating capillary. With the aid of an ion funnel the ion beam is concentrated and transmitted to the following vacuum region. After a couple of differential pumping regions and two octopole ion guides the ion beam enters an ion trap. The ion trap is very important, since it couples the continuous region to the pulsed instrument leading the ions to thermalize in the trap. The trapped ions are extracted, accelerated and re-referenced to ground prior to entering the field free region. The ions are photodissociated at the turning point of the reflectron and the fragments are detected by a dual micro channel plate detector and identified by their flight times.

Two of the projects, spectroscopy of $\text{TiO}^+(\text{CO}_2)$ (Chapter 3) and photoionization studies of PtC_nH_m (Chapter 5), use laser ablation to produce the ion/molecule of interest. The instrument in our lab used laser ablation of a titanium rod, followed by reaction and clustering with CO_2 to produce $\text{TiO}^+(\text{CO}_2)$. The ions were then accelerated and re-referenced to ground prior to entering the field free flight tube. As in the electrospray instrument, the ions were photodissociated at the turning point of the reflectron. Fragments were monitored at the detector.

Photoionization studies of PtC_nH_m were carried out at the Advanced Light Source (ALS) at Lawrence Berkeley National Laboratory. Laser ablation of a platinum tube produced neutral platinum, which reacted with methane to produce gas-phase PtCH_2 and HPtCH_3 . These molecules are then photoionized in the extraction region of a reflectron time of flight mass spectrometer using tunable vacuum ultraviolet light and the ions are detected on a microchannel plate detector.

The remainder of this chapter describes the electrospray instrument in detail. Our laser ablation instrument has been described in John Husband's thesis² and in two review articles.^{3,4} The photoionization instrument and ALS capabilities are described in several papers.^{5,6}

2.2 ESI Apparatus Description

The study of solvation of metal dications Co^{2+} , Ni^{2+} and Cu^{2+} by acetonitrile and water was carried out using an electrospray source to produce microsolvated $\text{M}^{2+}(\text{CH}_3\text{CN})_n(\text{H}_2\text{O})_m$ ions that are then mass selected. Selected ions are irradiated with a pulsed tunable laser. The charged photofragments were characterized by their masses using a dual time-of-flight reflectron mass spectrometer. Two key recent improvements to the apparatus are an ion funnel used for improved signals and liquid nitrogen cooling for the ion trap used for improved spectral resolution. For the solvation studies, only the ion funnel was used. The electrospray ionization ion trap reflectron time-of-flight mass spectrometer is shown in figure 2.1.

2.2.1 Ion Production and First Differential Region

With the introduction of electrospray ionization (ESI) by Fenn and co-workers in the 80's, multiply charged ions became very popular in gas phase studies.¹ In an ESI source, a solution of the ion of interest in a solvent such as water, methanol or acetonitrile flows through a thin needle. The potential difference between the hypodermic needle and the desolvating capillary causes the droplets to be highly charged. As the solvent evaporates, the droplets shrink in size resulting in an increased charge on the droplets' surface. As the surface charge increases due to instability of the droplet, the droplets undergo fission to produce smaller droplets

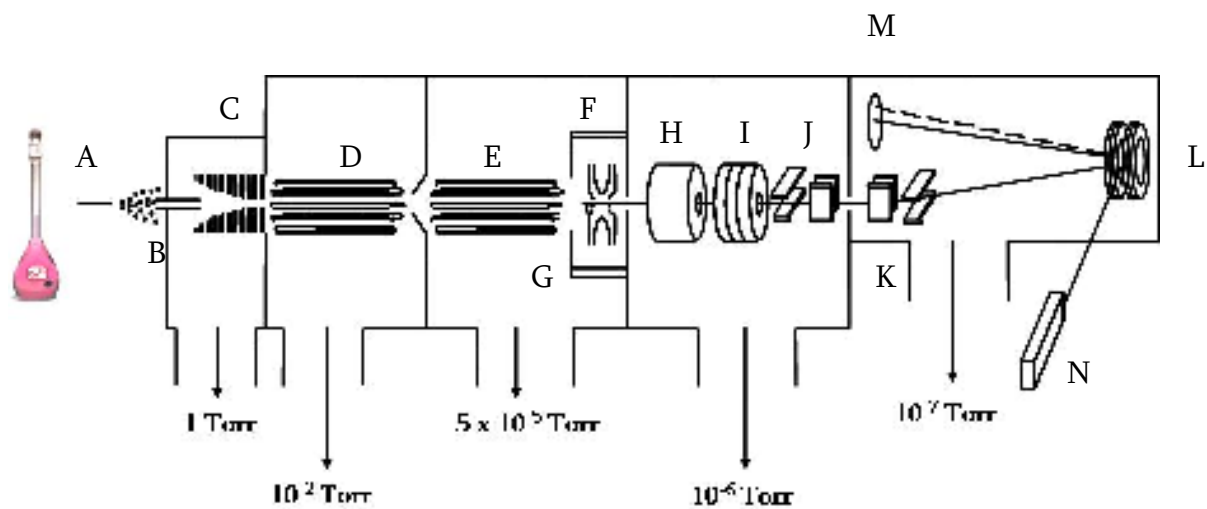


Figure 2.1: Schematic drawing of the electrospray ionization dual time-of-flight mass spectrometer apparatus that was used for $M^{2+}(\text{CH}_3\text{CN})_n(\text{H}_2\text{O})_m$ study.

until stable gas phase cluster ions are produced.⁷ Many combinations of clusters are produced and the charges depend on the conditions of the needle, capillary and metal solvent mix.

These multiply charged metal clusters are produced with an electrospray ionization source (ESI) in the room environment. A 10^{-3} – 10^{-4} M solution of the appropriate M^{2+} salt in the solvent of interest flows through a stainless steel needle (A) held at a high voltage (5–6 kV for water; 3.5–5 kV for acetonitrile). All the solutions were made using nitrate salts due to the difficulties of dissolving chlorides and sulfates in pure acetonitrile. Salts were vacuum dried overnight while acetonitrile was dried using molecular sieves for a day prior to making the solution in order to create pure acetonitrile clusters with metal dications such as $M^{2+}(\text{CH}_3\text{CN})_n$. Mixed clusters were made with an acetonitrile to water ratio of 50:1. A desolvating capillary (B), which is usually held at 100–150 V, is the coupling between the atmospheric ESI source and the vacuum instrument. It is a stainless steel tube is 6" long with an internal diameter of 0.03" and outer diameter of 0.0625". This tube is heated to $\sim 50^\circ\text{C}$ to detach excess solvent molecules from the clusters. After passing through the desolvating capillary the ion clusters enter the first differential region, which is at ~ 1 Torr.

2.2.2 Modifications to the First Differential Region

A problem with the electrospray is that ions are formed at atmospheric pressure, while the detector is at $\sim 10^{-7}$ Torr. It is challenging to achieve this

differential in pressure while maintaining good ion transmission. Until recently, we used a tube lens, which is basically a tube with high voltage, to guide ions from the desolvating capillary through a skimmer and into the next chamber. Unfortunately, the tube lens is not very useful for keeping the ions in a narrow beam. Therefore, most of the ions do not pass through the skimmer as shown in figure 2.2. When the capillary is moved closer to the skimmer, the pressure in the next chamber gets too high. Several groups have used a device called an ion funnel^{8,9} to solve this problem, increasing the ion signal by at least an order of magnitude, while reducing the gas load on later chambers. In this work, we have adopted this approach. Our ion funnel (C) is made of 32 plates with apertures exponentially decreasing in diameter from 1" to 0.05". A similar concept is shown in figure 2.2. The plates are made of 0.035" thick stainless steel and the spacing between the plates is 1/16". There is a potential difference of 10-50 V between the first and last plates. The plates are connected to each other with 1 M Ω resistors, creating a DC gradient, which causes the ions to flow towards the skimmer. A 180^o phase shifted RF signal (10-500 V peak to peak at 1 MHz) is applied to alternating plates using 1000 pF to compress the ion beam. We built the electronics based on O'Connor's design for a high voltage regulated oscillator which produces two phase shifted sine waves.¹⁰ The RF frequency and amplitude can be changed easily to optimize the ion beam transmission and is usually run with amplitude of 30 V peak-to-peak. Using this technique, we were able to significantly improve the ion beam intensity thus allowing us to study smaller cluster ions.

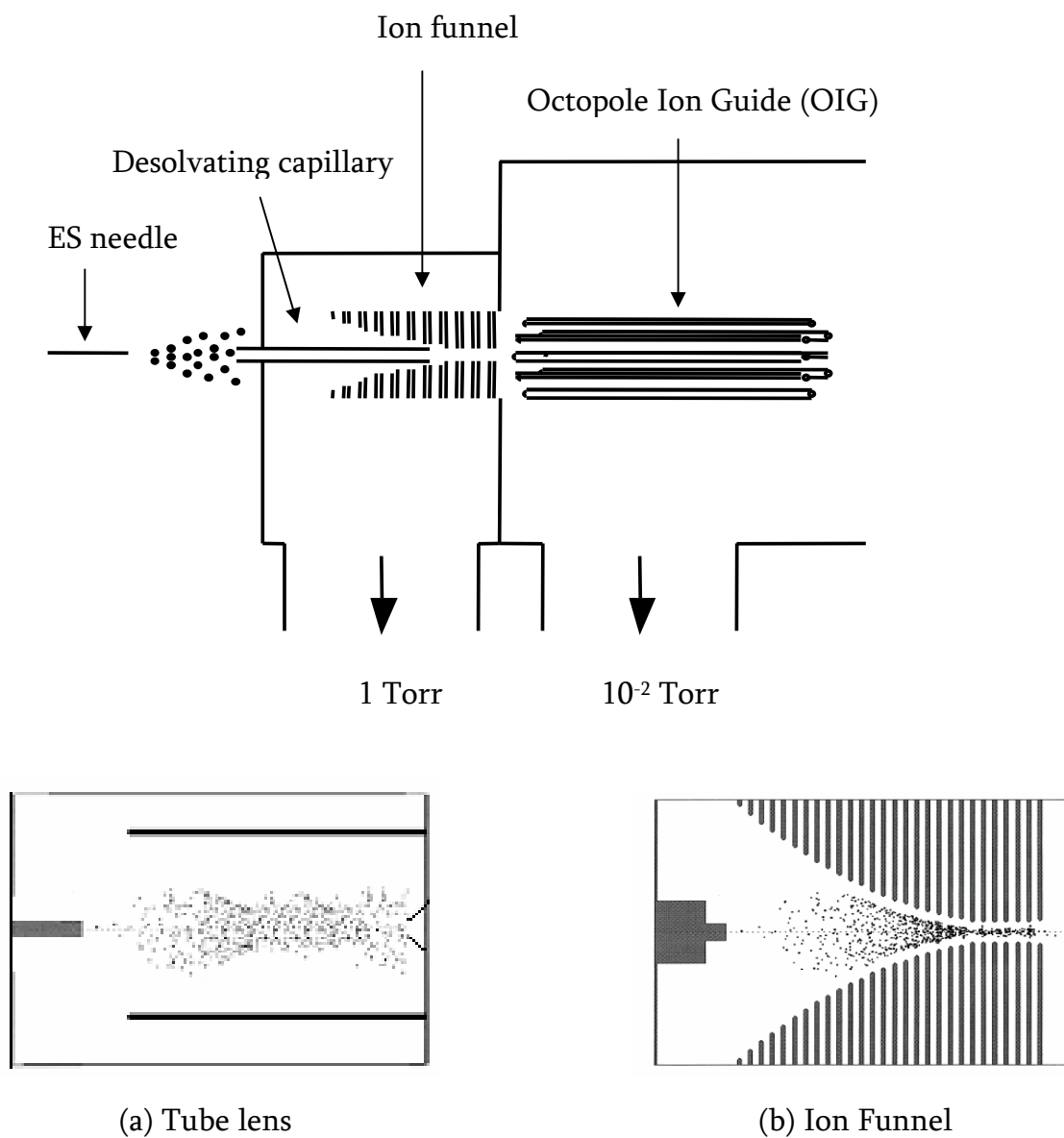


Figure 2.2: Schematics of (a) tube lens and (b) an ion funnel that are used for ion transmission and to create a concentrated ion beam.

2.2.3 Second and Third Differential Regions

The first octopole ion guide (OIG) (D) aids the transport of cluster ions through the second differential pressure region to the next chamber. The second octopole ion guide (E) leads the ions to a radio-frequency quadrupole ion trap (F) (R. M. Jordan Co.). The OIG consists of 8 stainless steel rods with alternating RF on each of the stainless steel poles. The first OIG is floating at a 10 V DC potential and is 10" in length. The second OIG is shorter, 5", and has no DC offset. The main purpose of the OIGs is to transport ions efficiently through differential pumping regions over a long distance and to lose any neutrals in the beam. The loss of ions over a long distance is minimized by narrowing the distance between the skimmer and the OIG as well as between the back plate of the ion funnel and front plate of the ion trap.

The ion trap serves three useful purposes: (1) collecting ions to improve the overall signal and (2) coupling the continuous ion source to the pulsed time-of-flight mass spectrometer (TOF-MS) (3) thermalizing the ions that are collected. The back plate of the ion trap is held at (-) 10 to (+) 10 V to guide ions to the trap. Ions are trapped for up to 49 ms when running at the typical 20 Hz repetition rate. During this time they collide with the background gas, comprising 1 mTorr of He that has been added to the trap. This causes the ions to thermalize to 298 K. Prior to ejecting the ions the RF is turned off, which causes the ions to diffuse within the trap. A 100 V pulse is provided to the front plate of the trap after a delay of 2 μ s, ejecting the

stored ions. Then ions are accelerated into the last differential region by a plate held at (-) 1800 V. This is where the continuous region of the instrument is coupled to the pulsed region.

The photodissociation of parent ions containing a wide distribution of internal energies results in peak broadening. Recently, a liquid nitrogen cooling system (G) was added to the ion trap, which cools the trap gas (He) and the ion trap environment through a thermal link. When liquid N₂ is added to the reservoir, ions can be thermalized down to ~80 K, lowering the internal energy and improving the spectral resolution. The liquid nitrogen cooling reservoir was not utilized for the solvation studies mentioned here.

2.2.4 Last Differential Region

The pressure of this region is around 10⁻⁶ Torr under typical running conditions. The ions are re-referenced to ground potential and focused by a series of ion optics. A pair of deflector plates transmits the ions to the field free flight tube and also acts as a mass gate to select the parent of interest. Following the mass gate a set of vertical deflector plates guides the ion beam to optimize overlap with the laser beam.

The re-referencing tube (H) is a 3" long 1.5" diameter stainless steel tube that is initially held at (-) 1800V, the same potential as the acceleration plate. When the pulsed ion packet reaches the center of the tube, the voltage is set to zero, uniformly

changing the electric field around the ions to ground. This is the re-referencing process. It is important to re-reference ions to ground, so that the flight tube can also be grounded, which simplifies the instrumentation as well as lowers the operating risks.¹¹ Following the re-referencing tube is a 1.25" i.d. Einzel lens (I). The Einzel lens has three cylinders where the outer rings are at ground potential with the middle ring at (-) 2.3 kV. When the ions enter the Einzel, ions travel from the grounded re-referencing tube to the grounded first ring. The Einzel lens spatially focuses the ion cloud for optimum overlap with the dissociation laser. A pair of deflector plates (J) provides the horizontal and vertical alignment of the ion beam into the field free region of the instrument.

2.2.5 Detector Region

The time-of-flight mass spectrometer we use was initially introduced by Wiley and McLaren in the fifties as an analytical tool.¹² Using the Wiley McLaren configuration a spatially dispersed ion cloud is focus into a tight packet of ions at a focal point, reflectron. In this region the laser beam intersects the ion beam at the turning point of the reflectron. Under running conditions the pressure of this region is 10^{-7} Torr. With the aid of deflector plates (J,K) the ions are focused to the center of the reflectron (L). The second set of deflector plates also act as the mass gate with a pulsed voltage to allow ions to go through reflectron at the correct angle to reach the detector. Thus, it eliminates unwanted masses.

The reflectron consists of ten 1.8" i.d., 3.6" o.d. stainless steel plates spaced by 0.174" cm and joined with resistors as shown in figure 2.3. The first, second and last plates have meshes. This is a two-field reflectron, with the potential on plate 2 usually using an external resistor to 1.2 kV. Internal resistors (261 k Ω) provide a constant electric field between plates 2 and 11. Under typical condition, (+) 2970 V is applied to plate 11. The ions that enter the reflectron are decelerated by the electric field and come to a rest at the turning point, midway between plates 6 and 7. This is where the laser crosses with the ions. Then the ions are accelerated back out of the reflectron with the same kinetic energy they entered. The reflectron is at "high field" (-306 V/cm) at the turning point under normal conditions, which gives a more compact ion packet, and maximizes the overlap with the dissociation laser. This field can be controlled by an external resistor to the "low field" (-150 V/cm) to further study kinetic energy release.

Directly behind the last plate of the reflectron is an imaging detector aligned with the center. When the reflectron power is turned off, the ions hit the imaging detector instead of turning around to the ion detector. The imaging detector is very useful to troubleshoot the instrument and to focus and align the ions to the center of the reflector. The imaging detector is a dual micro channel plate detector coupled to a 1" phosphorous screen so that a glow is observed as the ions hit. Under normal running conditions this detector is not in use, and the ions are redirected to the ion detector by the reflectron.

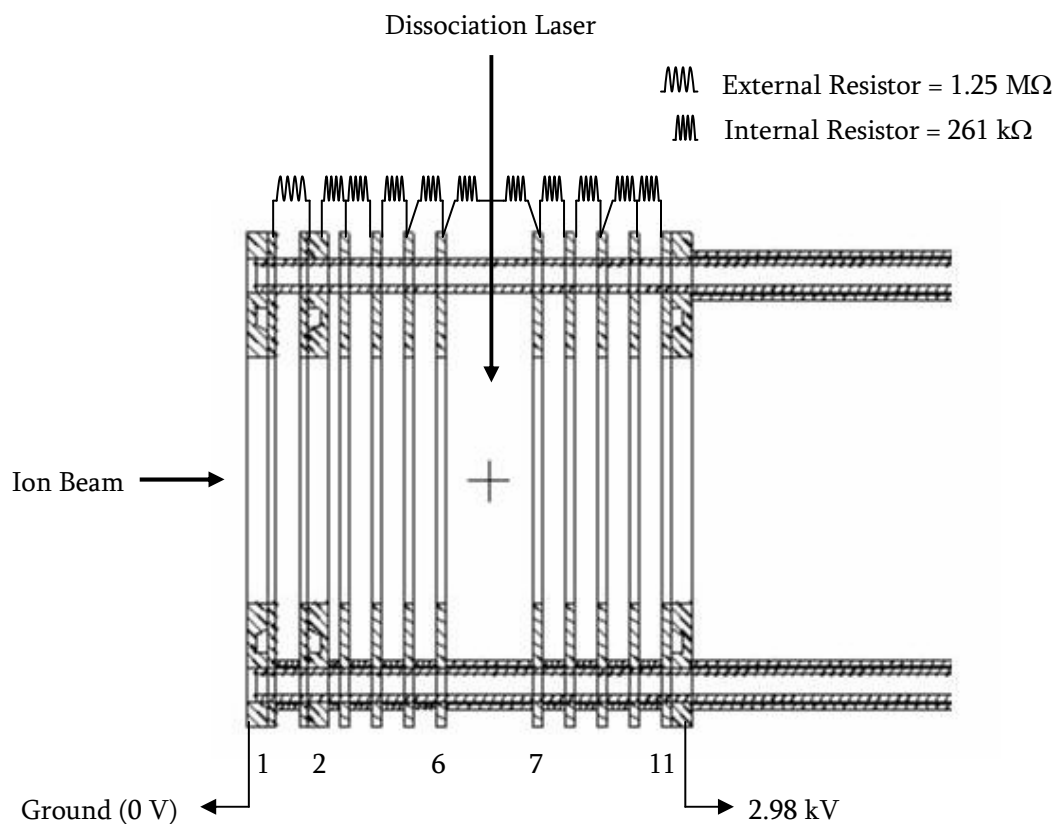


Figure 2.3: Side view of the reflectron. The turning point for the ions is shown with a cross.

The mass selected clusters are irradiated with the unfocused output of a pulsed (20 Hz) Nd:YAG-pumped dye laser (N) with a line width of $<0.1\text{cm}^{-1}$ that is tunable from 540 to 900 nm. For some of these studies, the 532 nm second harmonic and 355 nm third harmonic of a Nd:YAG laser were also used. When the clusters are photodissociated and the charged fragments and remaining parent ions are accelerated down a second field-free tube to the detector (M). The ion detector is located 26" from the center of the reflectron. A 40 mm dual micro-channel plate detector detects the resulting ions. The ion signal is produced by an avalanche effect. The resulting signal is amplified, collected on a digital oscilloscope or a gated integrator, and recorded digitally using a LabView-based program.

2.2.6 Data Processing and Experimental Timing

Mass spectra are collected on a 200 MHz Tektronix TDS 2022 digital oscilloscope with a LabView-based program. A mass spectrum of the ions is produced by measuring ion signals as a function of time on the digital scope. Difference (mass) spectra are obtained by subtracting mass spectra obtained when the dissociation laser is off from those when it is on. A home-built chopper wheel assists in producing a difference spectrum by allowing for the subtraction of laser-on spectra from laser-off spectra. Difference (mass) spectra were used to find the relative abundance of the dissociated fragments as well as to identify the fragments and fragment pathways at a given wavelength. The difference spectrum can also give information that is also

sensitive to dissociation dynamics and kinetics. Kinetic energy release leads to broadening of the fragment time-of-flight peaks, while slow dissociation leads to tailing in the fragment peak toward the parent time.¹³ The area of the signal can be computed using numerical integration of difference spectral peaks or monitoring the parent and fragment peaks using a gated integrator. The photodissociation spectra were obtained by monitoring the fragment ion yield as a function of wavelength and then normalizing to both the parent ion signal and laser power.

Experimental timing is key when studying a pulsed ion packet dissociated by a pulsed laser. Re-reference, mass gate, dissociation laser Q-switch, the delay and the trigger for the scope (fragment flight time) are all with respect to the extraction pulse. Stanford Research System and Precision Plus digital pulse generators control pulse timing via TTL outputs. Figure 2.4 shows the timings associated with the instrument.

2.3 Ablation Apparatus

The metal centered ion species were produced using laser ablation techniques for the $\text{TiO}^{2+}(\text{CO}_2)$ study. This differentiates the instrument from the previously described ESI instrument. However, the regions following the skimmer are very similar to the previously described ESI instrument's ion optics. The laser ablation dual time-of-flight mass spectrometer is shown in figure 2.5. The instrument and

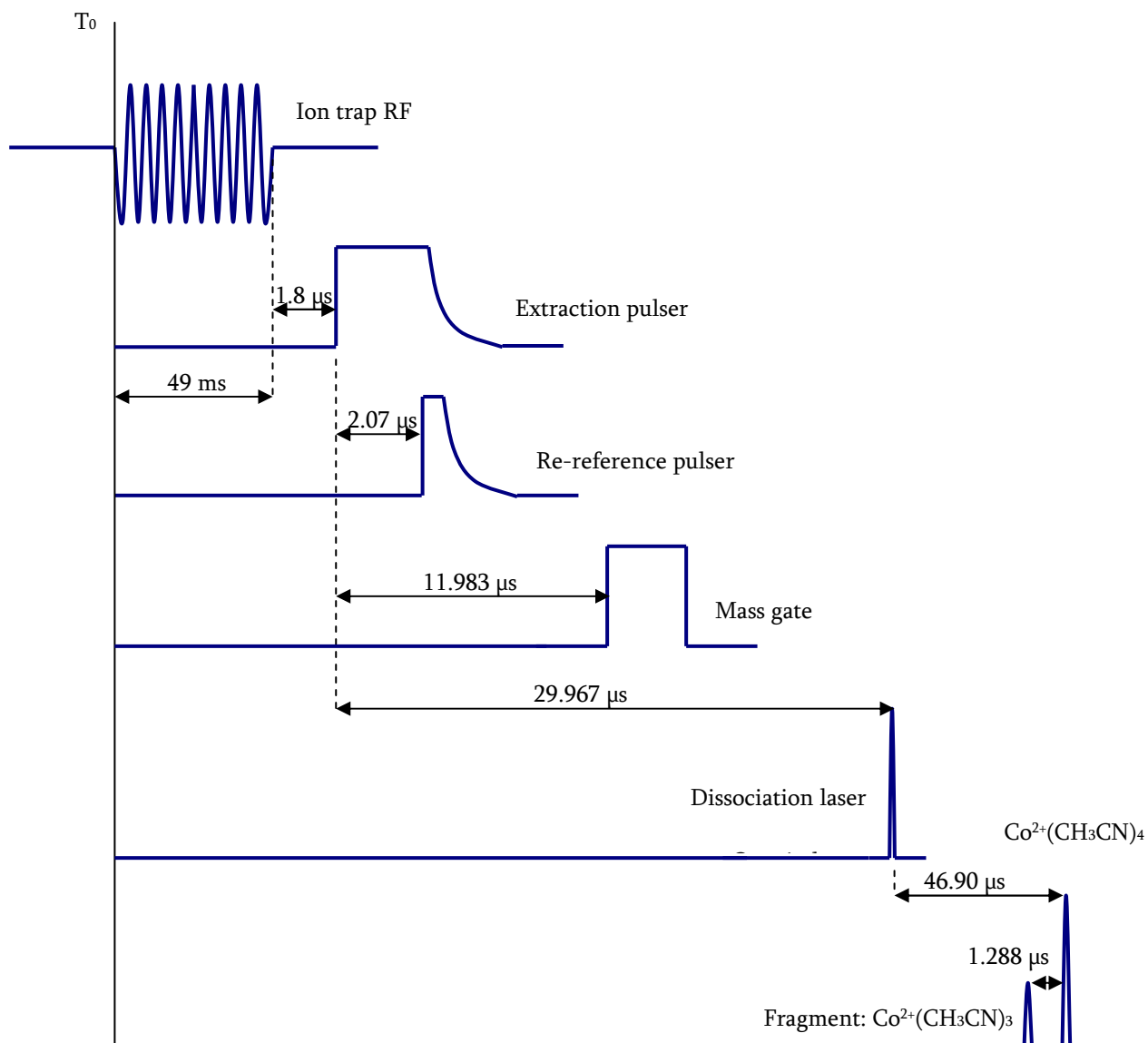


Figure 2.4: Experimental timing for the electro spray ionization dual time-of-flight apparatus. The timings given are for $\text{Co}^{2+}(\text{CH}_3\text{CN})_4$.

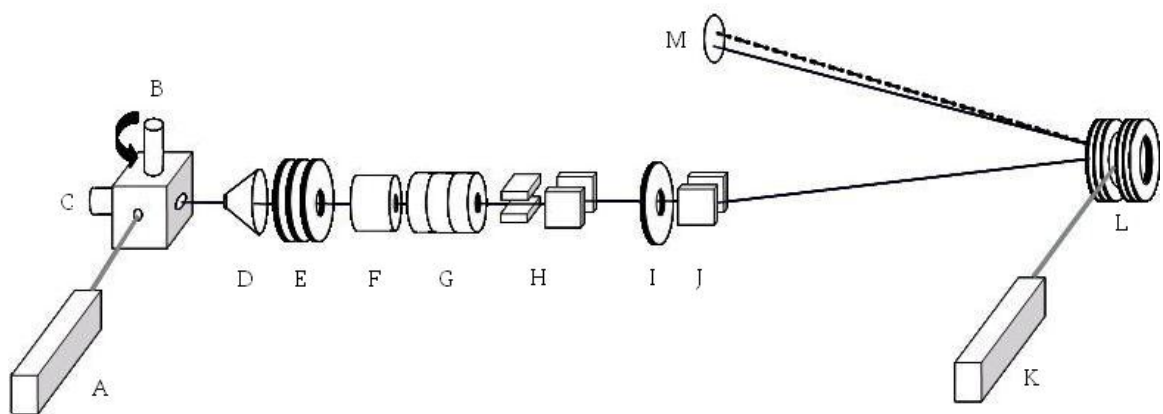


Figure 2.5: Schematic drawing of the laser ablation dual time-of-flight mass spectrometer apparatus that was used for the $\text{TiO}^+(\text{CO}_2)$ study.

data acquisition software are described in detail in John Husband's thesis, so only the conditions used for the $\text{TiO}^+(\text{CO}_2)$ study are described here.²

Singly charged metal cations are generated by laser (A) ablation of a translating and rotating titanium rod (B) in the source region. An external stepper motor rotates and translates the rod. A Nd:YAG laser at 532 nm with laser pulse energy of 13 mJ is used for ablating the rod. Once produced, Ti^+ ions react with ~0.1% CO_2 seeded in helium introduced through a piezoelectric pulsed valve (C)¹⁴ to produce Ti^+ , TiO^+ and $\text{TiO}^+(\text{CO}_2)_n$. The pulsed valve is operated at 10 to 40 psi backing pressure. The rep rate for the whole instrument is at 20 Hz.

Ions produced by laser ablation undergo supersonic expansion into a vacuum where the ion beam is skimmed (D) and extracted into the time-of-flight mass spectrometer. In the meantime, the ions are cooled electronically and vibrationally by collision with bath-gas helium. Typical rotational temperatures are 10 K.^{15,16} The cations of interest are mass selected and re-referenced (F) to the ground potential before entering the flight tube through the Einzel lens (G). The ion optics, fragmentation, and data processing are similar to those for the ESI instrument.

2.4 Advanced Light Source Ablation Apparatus Description

All the studies on Pt were conducted at the Chemical Dynamic Beamline at the Advanced Light Source at Lawrence Berkeley National Laboratory. The

instrument setup consists of a laser ablation source region coupled to a time-of-flight reflectron mass spectrometer. The molecular beam is skimmed and irradiated with tunable vacuum ultraviolet (VUV) light. The ionization VUV light energies are 8-14 eV and linewidths of 25 to 100 meV were used.^{5,6}

The neutrals are made in the similar manner as previously described for the ions with laser ablation technique. The 532 nm output of a pulsed, 50 Hz rep rate Nd:YAG laser was used for ablation with power of 8 mJ on a platinum tube (Goodfellow, 99.95% pure) to produce gas phase platinum atoms. The platinum atoms then react with CH₄ or CD₄ introduced through a pulsed piezoelectric valve at a backing pressure of 2 atm. Different laser powers favor production of different neutral molecules: higher power favors PtC, while lower power favors H-Pt-CH₃. Ions produced in the source are deviated off the neutral molecular beam path prior to the skimmer by a set of deflector plates. The neutral molecular beam propagates to the next vacuum region through the skimmer.

The molecular beam is irradiated by the VUV light in the extraction region of a reflectron time-of-flight mass spectrometer. The newly made photo-ions are extracted with a high voltage pulse into the reflectron time-of-flight and are collected on a microchannel plate detector. To obtain photoionization efficiency curves, photoion mass spectra are obtained as a function of VUV energy. The signal for a particular ion is integrated and counted by a fast scaler and normalized to the VUV energy and photon flux.

2.5 Experimental Timing

Since our instrument is a pulsed time-of-flight mass spectrometer, the timing is very important. Timing is controlled by two digital pulse generators, a Stanford Research Systems DG 535 and a Precision Instruments Inc. Model 9650. The initial time, T_0 , is arbitrary. The entire timing triggers are relative to T_0 and the repetition rate for the entire instrument is set by the delay generators 20 Hz. We use TTL logic outputs (0-5 V pulses) with high impedance load. There are a total of 8 channels that can be used: four channels (A, B, C, and D) and four other combination channels. Each channel can be triggered relative to an internal trigger, external trigger or by another channel. These pulses are used throughout the instrument for various purposes: to trap ions, select mass, laser flash lamp and Q-switch delays, etc.

2.5.1.1 Electrospray Ionization Instrument

Timing on this instrument is summarized in figure 2.4. First, the ions are accumulated inside the ion trap. The RF voltage to the ion trap is turned off, and ions are extracted into the time of flight mass spectrometer with a pulsed voltage. All subsequent times are relative to extraction timing. Then the extracted ion packet referenced to ground potential via the reference tube. Initially as the ions enter the tube the potential is held at (-) 1800 V and then triggered to provide a ground potential, so that as the ions leave, they are grounded. Then the ions are mass

selected with the mass gate. The mass gate is a pulsed voltage that can be controlled to select a mass of interest. When the mass gate is at continuous voltage a mass spectrum of all the stable ions can be monitored.

Mass selected ions then enter the field free region of the time-of-flight tube and travel towards the reflectron. The ions are irradiated with the dissociation laser at the turning point of the reflectron which is another critical time control. The flashlamp-Q-switch delay can be experimentally found by maximizing the laser power. The dissociation laser Q-switch time is controlled to optimize the maximum dissociation. This can be done either experimentally by observing the fragment or calculating the time using parameters that are unique to the instrument (table 2.1).

2.5.1.2 Ablation Instrument

It is critical that the timing for this instrument is properly maintained because the whole instrument is pulsed. Initially the pulsed valve gets a trigger and the ablation laser flash lamp is triggered shortly after. Just after the gas pulse leaves the holder, the ablation laser fires on to the metal rod so the metal cation can react with the gas molecules around the rod inside the holder. These ions are pulse extracted and accelerated to 1800 V kinetic energy. The rest of the instrument shares the same as the electrospray instrument.

2.5.2 Arrival Time Calculations

When the mass gate is turned off, the spectrum that is seen at the detector includes all the stable ions that were produced. The arrival time of an ion is related to its mass by

$$\tau = a\sqrt{m/z} + t_0$$

The parameters a and t_0 can be initially calibrated using two known ion peaks.

When ions are photodissociated, the photofragment flight times reflect the fact that the ions spend a portion of the time as parents prior to fragmenting. Therefore the photofragment flight time can be calculated using the equation below.

$$\tau = b\sqrt{m/z_{(parent)}} + c\sqrt{m/z_{(fragment)}} + t_0$$

where $b + c = a$. So to identify the fragment, use the above equation to find the time difference from the parent flight time. Typical parameters a , b , and c for the two instruments are listed below.

Instrument	a	b	c
Electrospray	4.426	3.116	1.31
Ablation	5.87	3.82	2.02

Table 2.1: Timing constants are unique to each instrument and also allow finding the appropriate mass using arrival time of the ions.

2.6 References

- (1) Yamashita, M.; Fenn, J. B. *J. Phys. Chem.* **1984**, *88*, 4451.
- (2) Husband, J. *Thesis University of Massachusetts Amherst* **2001**.
- (3) Metz, R. B. *Adv. Chem. Phys.* **2008**, *138*, 331.
- (4) Metz, R. B. *Int. Rev. Phys. Chem.* **2004**, *23*, 79.
- (5) Metz, R. B.; Nicolas, C.; Ahmed, M.; Leone, S. R. *J. Chem. Phys.* **2005**, *123*, 114313.
- (6) Citir, M.; Metz, R. B. *J. Chem. Phys.* **2008**, *128*, 024307.
- (7) Smith, J. N.; Flagan, R. C.; Beauchamp, J. L. *J. Phys. Chem. A* **2002**, *106*, 9957.
- (8) Him, T.; Tolmachev, A. V.; Harkewicz, R.; Prior, D. C.; Anderson, G.; Udseth, H. R.; Smith, R. D.; Bailey, T. H.; Rakov, S.; Futrell, J. H. *Anal. Chem.* **2000**, *72*, 2247.
- (9) Prior, D. A., G.; Bruce, J.; Schaeffer, S.; Kim, T. M.; Smith, R. *Computing and Information Sciences 1999 Annual Report* **1999**, PNNL.
- (10) O'Connor, P. B., Costello, C. E., Earle, W. E. *Journal of the American Society for Mass Spectrometry* **2002**, *13*, 1370.
- (11) Posey, L. A., DeLuca, M. J., Johnson, M. A. *Chemical Physics Letters* **1986**, *131*, 170.
- (12) Wiley, W. C., McLaren, I. H. *Rev. Sci. Instrum.* **1955**, *26*, 1150.
- (13) Thompson, C. J.; Faherty, K. P.; Stringer, K. L.; Metz, R. B. *Phys. Chem. Chem. Phys.* **2005**, *7*, 814.
- (14) Proch, D., Trickl, T. *Rev. Sci. Instrum.* **1989**, *60*, 713.

- (15) Citir, M.; Altinay, G.; Metz, R. B. *J. Phys. Chem. A* **2006**, *110*, 5051.
- (16) Aguirre, F.; Husband, J.; Thompson, C. J.; Stringer, K. L.; Metz, R. B. *Journal of Chemical Physics* **2002**, *116*, 4071.

CHAPTER 3

PHOTOFRAGMENT SPECTROSCOPY OF $\text{TiO}^+(\text{CO}_2)$

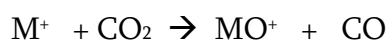
3.1 Introduction

Metal oxides are interesting due to their importance in astronomy and as catalysts. Astrophysicists consider cool stars to be the largest stellar class. Therefore, understanding their properties is vital for astronomy in general. Diatomic molecules play an important role in the middle region of the photosphere of cool stars. Most interesting is the domination of TiO molecule in the spectrum of M-type stars due to its opacity in the visible and near-infrared regions.¹

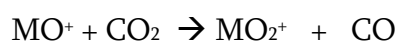
Ionization of metals and oxygen leads to the formation of a pool of free electrons in interstellar clouds. Titanium and oxygen ionization results in the production of TiO^+ and TiO .² Some stars are classified by the abundance of certain metal oxides and cations present in them. For instance, cool M and S class stars contain titanium oxides.³ Furthermore, the temperature of the stellar atmosphere is determined by the rotational structures of these oxides.⁴ Hence, studying the metal oxides, cations, and the excited states of these molecules in a quantitative manner is very important. Although there has been some theoretical work² on TiO^+ , little is known about it experimentally, whereas an abundance of information is available for TiO.

Another motivation for studying transition metal oxide cations is catalysis. Transition metal oxides are widely used in industry as oxidation catalysts. A recent interesting application of titanium oxide is its use as a non-platinum electro catalyst for oxygen reduction reactions that can be useful in polymer electrolyte fuel cells.⁵ There have been numerous gas-phase studies of transition metal oxides to understand the oxo ligand influence on metal chemistry and to characterize reactions such as methane to methanol conversion.⁶⁻⁹

Recently, Koyanagi and Bohme measured the room temperature kinetics of the sequential reactions of 46 main group and transition metal cations with CO₂.¹⁰ Several early transition metal cations (including Ti) activate CO₂:



While sequential activation is observed for Hf⁺, Nb⁺, Ta⁺ and W⁺:



Breaking the OC-O bond requires 5.52 eV. So, Ti⁺ oxygen abstraction from CO₂ is consistent with the measured Ti⁺-O bond strength of 6.88±0.07 eV.¹¹

To date, the only spectroscopic information on TiO⁺ is from photoelectron spectroscopy of TiO. Dyke and co-workers irradiated TiO from a high-temperature oven with 21.22 eV photons and observed transitions assigned to two states of TiO⁺. A weak band due to ionization to TiO⁺ (X, ²Δ) gives an ionization energy of 6.82±0.02 eV. A second band at T₀=10250±80cm⁻¹ with vibrational frequency ω_e=860±60 cm⁻¹ and r_e=1.73±0.01 Å was assigned to the A, ²Σ⁺ state.¹² Neutral TiO has a ³Δ ground

state with the electron configuration $8\sigma^2, 3\pi^4, 1\delta^1, 9\sigma^1$ and $r_e=1.620 \text{ \AA}$. The $^2\Delta$ ground state of TiO^+ results from removing 9σ electron (figure 3.1). Removing the 1δ electron gives the $^2\Sigma$ excited state. Weisshaar and co-workers measured the photoelectron spectrum of supersonically cooled TiO using resonance-enhanced multi-photon-ionization.¹³ They measure an ionization energy of $6.819\pm 0.006 \text{ eV}$, in accord with the earlier work. The vibrational frequency of the TiO^+ ground state is $\omega_e=1045\pm 7 \text{ cm}^{-1}$, with anharmonicity $\omega_e x_e=4\pm 1 \text{ cm}^{-1}$. They observe an excited $^2\Sigma^+$ state with an origin at $11227\pm 17 \text{ cm}^{-1}$, a vibrational frequency $\omega_e=1020\pm 9 \text{ cm}^{-1}$, and anharmonicity $\omega_e x_e=6\pm 2 \text{ cm}^{-1}$. Although this state lies at a similar energy to the $^2\Sigma$ observed by Dyke and co-workers, the very different vibrational frequencies led Weisshaar and co-workers to propose that TiO^+ has two distinct low-lying $^2\Sigma$ states, and resonant two-photon ionization reaches one state, while one-photon ionization reaches another. Unfortunately, $^2\Delta\text{-}^2\Sigma$ optical transitions are forbidden, so these states are difficult to characterize by other means, and are not useful for astronomical observation of TiO^+ . The low ionization energy of TiO , and its high bond strength of $6.92\pm 0.09 \text{ eV}$ allow for TiO^+ to be formed by chemionization:



Due to interest in CO_2 activation, the electronic and vibrational spectroscopy of several transition metal cation complexes with CO_2 have been measured. Brucat and coworkers have studied the electronic spectroscopy of CO_2 bound to Ni^+ and Co^+ .¹⁴⁻¹⁶ In our lab, we have looked at the electronic and vibrational spectroscopy of

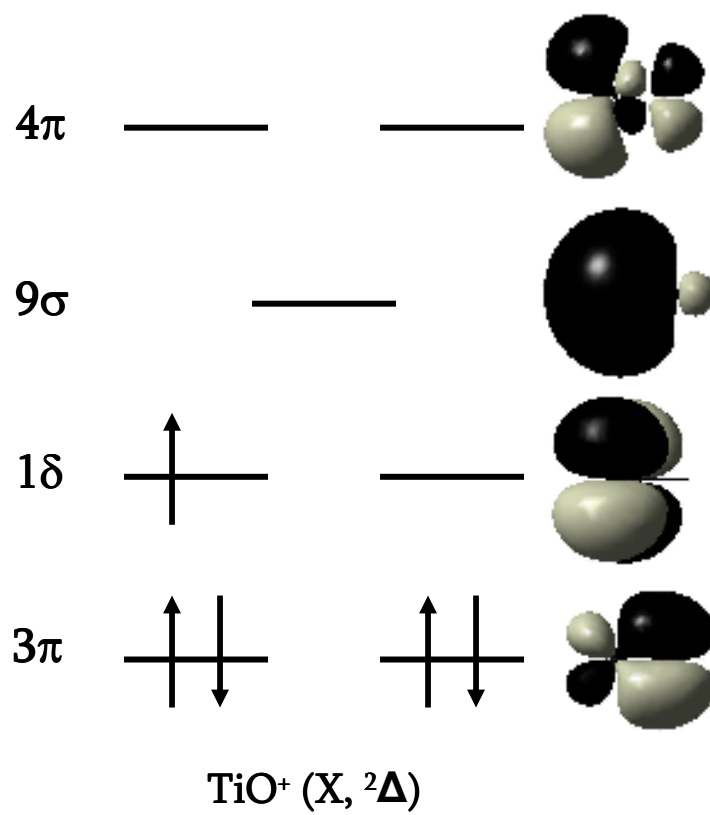


Figure 3.1: Molecular orbital diagram and electron occupancy of $\text{TiO}^+ (\text{X}, {}^2\Delta)$.

$V^+(CO_2)$.^{17,18} Duncan and coworkers have studied the vibrational spectroscopy of $M^+(CO_2)_n$ clusters for several metals.¹⁹⁻²¹

Other studies have focused on $MO^+(CO_2)_n$ to understand metal-ligand interactions. Brucat and co-workers have produced $ZrO^+(CO_2)_n$ using molecular-beam methods and characterized an excited electronic state with photofragment spectroscopy.²² As the CO_2 electrostatic bond with ZrO^+ is dissociated, much information about the ZrO^+ excited and ground states are revealed. For example, the binding to CO_2 decreases the energy gap to the excited state indicating that the solvent molecule binds to the excited state much more strongly than to the ground state. This can be explained with respect to the upper-electronic state properties of ZrO^+ , particularly the greater electric dipole moment and the larger separation of its internuclear bond. This information is obtained by comparing to other complexes of ZrO^+ such as $ZrO^+(N_2)$.

The Ti^+-O bond is very strong, and consequently it is hard to use photofragment spectroscopy to observe the absorptions of this molecule. To understand the excited states without breaking the Ti^+-O bond, one can look into attaching a spy molecule like CO_2 and then breaking the metal-ligand bond. We have measured the photodissociation spectrum of $TiO^+(CO_2)$ to characterize an excited state of the TiO^+ chromophore. When TiO^+ is photoexcited, its electron density changes, and the response of the ligand to these changes is reflected in the

photodissociation spectrum. In addition, calculations help to further characterize the ground and excited states of TiO^+ and $\text{TiO}^+(\text{CO}_2)$.

3.2 Experimental

The experimental apparatus, a dual time-of-flight reflectron photofragment spectrometer, and methods used have been described in detail previously in Chapter 3 and literature.^{23 24} In this study, titanium cations are generated by laser ablation of a translating and rotating titanium rod (Strem Chemicals, 99.98% pure) in the source region. The Ti^+ ions react with ~0.1% carbon dioxide (99.98% pure) seeded in helium introduced through a piezoelectric pulsed valve to produce TiO^+ and $\text{TiO}^+(\text{CO}_2)_n$. The ions in the plasma then undergo supersonic expansion into vacuum, leading to substantial cooling. Vibrationally mediated photodissociation of $\text{V}^+(\text{CO}_2)$ reveals a rotational temperature of 12 K for ions produced in this source.¹⁷ The ion beam is then skimmed, extracted into the time-of-flight mass spectrometer and re-referenced to ground potential. The mass-selected ions of interest are then photoexcited at the turning point of the reflectron by the output of a pulsed (20 Hz) Nd:YAG-pumped dye laser with a line width of $<0.1\text{cm}^{-1}$. Fragment and parent ions re-accelerate to a dual micro-channel-plate detector. The resulting signal is amplified, collected on a digital scope or a gated integrator, and recorded digitally using a LabView-based program. The photofragment experiments produce two types of spectra. *Difference*

spectra are obtained by subtracting time-of-flight spectra with the dissociation laser block from those with it unblocked. Difference spectra are used to identify fragment ions and their relative abundance at a given wavelength. The difference spectrum can also give information on the dissociation dynamics and kinetics. Kinetic energy release leads to broadening of the fragment time-of-flight peaks, while slow dissociation leads to tailing in the fragment peak toward the parent time.²⁵ *Photodissociation spectra* are obtained by monitoring the fragment ion yield as a function of wavelength and normalizing to the parent ion signal and laser power. The intensities of features in the photodissociation spectrum are given by the product of the absorption cross section and the quantum yield for photodissociation.

3.3 Results and Discussion

3.3.1 Photodissociation Spectroscopy and Dissociation Kinetics of $\text{TiO}^+(\text{CO}_2)$

The photodissociation spectrum provides the absorption spectrum of $\text{TiO}^+(\text{CO}_2)$ when absorption leads to dissociation. Figure 3.2 shows the resonant photodissociation spectrum of $^{48}\text{TiO}^+(\text{CO}_2)$ obtained by monitoring $^{48}\text{TiO}^+$, the only fragment observed. The spectrum is richly structured, with four bands separated by $\sim 950\text{ cm}^{-1}$; each band consists of several peaks separated by $\sim 50\text{ cm}^{-1}$. In order to identify the vibrational progressions in electronic spectrum of $\text{TiO}^+(\text{CO}_2)$ we first

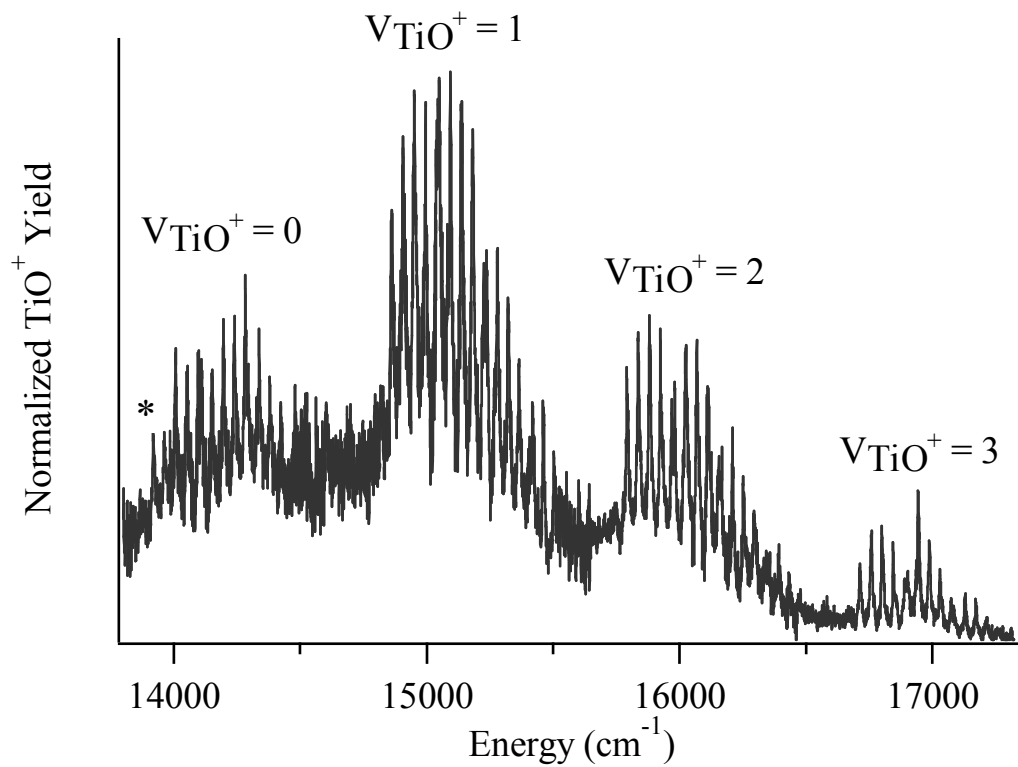


Figure 3.2: Photodissociation spectrum of $\text{TiO}^+(\text{CO}_2)$ with the covalent Ti-O stretch vibrational quantum numbers v_{TiO} marked. The asterisk denotes the electronic state origin.

consider the vibrational frequencies of TiO^+ and CO_2 . The vibrational frequency¹³ of the TiO^+ ground state is $\omega_e=1045\pm 7 \text{ cm}^{-1}$, with anharmonicity $\omega_e x_e=4\pm 1 \text{ cm}^{-1}$; the vibrational frequencies of CO_2 are 2349, 1333 and 667 cm^{-1} . The 950 cm^{-1} progression observed is thus likely due to the covalent Ti-O stretch in the excited state of $\text{TiO}^+(\text{CO}_2)$, while the low-frequency vibration(s) are due to non-covalent metal- CO_2 stretches and bends. In order to confirm the assignment of the high-frequency bands and to establish vibrational quantum numbers we measured the photodissociation spectrum of $\text{TiO}^+(\text{CO}_2)$ using the minor ^{50}Ti isotope (5% natural abundance), rather than ^{48}Ti (74% abundance). Since vibrational frequencies depend on the reduced mass of the molecule, the TiO^+ stretching frequency of the heavier ^{50}TiO isotopomer is lower than that of the more abundant ^{48}TiO isotopomer. Ignoring anharmonicity and the influence of the CO_2 , the ratio of reduced masses yields $\omega_{50} = 0.994986 \omega_{48}$. Using the vibrational frequencies of the ground (1045 cm^{-1}) and excited (950 cm^{-1}) states of TiO^+ gives an isotopic shift (in cm^{-1}) of

$$E_{^{48}\text{TiO}^+} - E_{^{50}\text{TiO}^+} \approx 4.76 v' - 0.24 \quad (1)$$

where v' is the excited state vibrational quantum number. Figure 3.3 shows the measured isotopic shifts, and the predictions of equation 1 for the cases where the first observed band corresponds to $v'=0$ (best fit), $v'=1$, and where the second band is due to $v'=0$. With the vibrational numbering established, the peak at 13918 cm^{-1} (asterisk in figure 3.2) is the origin. The excited state covalent TiO^+ stretching

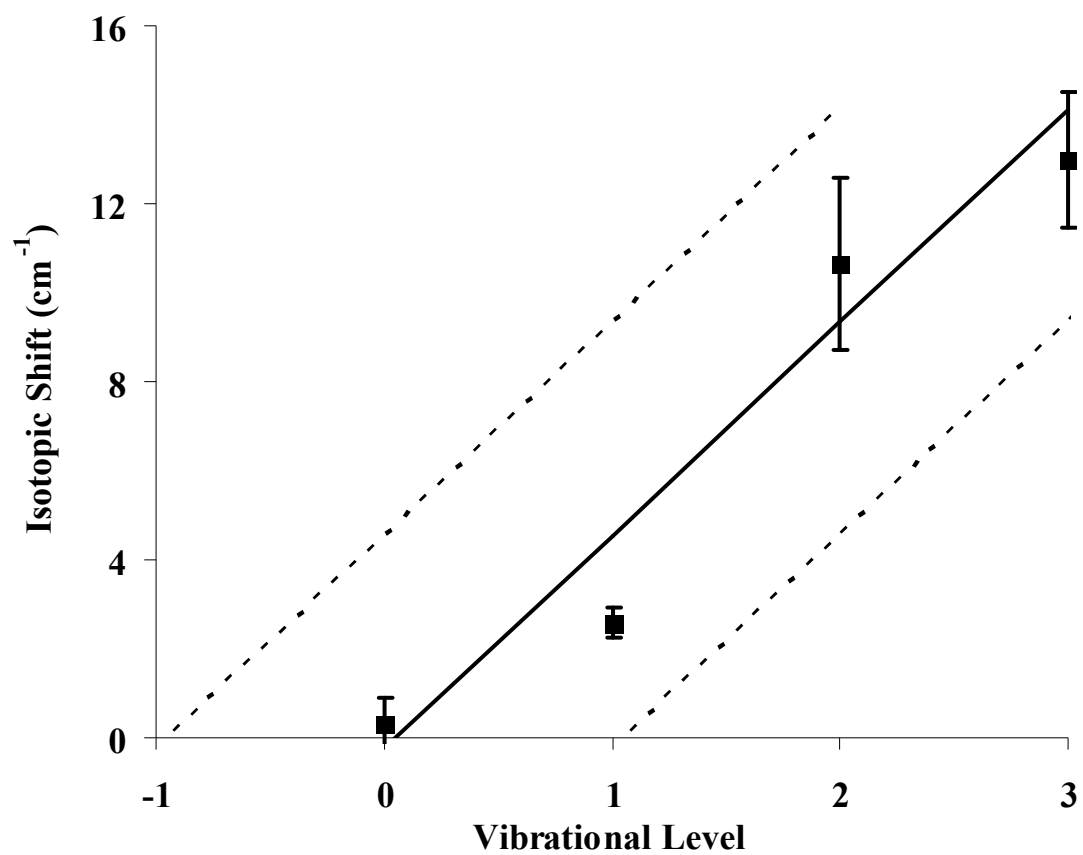


Figure 3.3: Assignment of covalent Ti-O stretch vibrational levels ν_{TiO} in the photodissociation spectrum of $\text{TiO}^+(\text{CO}_2)$. Experimental isotope shifts are compared to calculated shifts assuming the vibrational numbering is as shown in Fig. 2 (solid line) and with the numbering shifted by one (dashed lines).

frequency is $\omega'_{\text{TiO}}=952 \text{ cm}^{-1}$ with anharmonicity $x'_{\text{TiO}}=5 \text{ cm}^{-1}$.

Figure 3.4 again shows the photodissociation spectrum of $\text{TiO}^+(\text{CO}_2)$, but with the four high-frequency bands shifted, to allow for better comparison of the low-frequency structure in each band. The four bands exhibit almost identical low-frequency structure, indicating that there is little coupling between the covalent Ti-O stretch and the metal- CO_2 stretches and bends. There are progressions in two low-frequency modes: at 45 cm^{-1} and 186 cm^{-1} . The 186 cm^{-1} vibration is assigned to the non-covalent metal- CO_2 stretch, while the lowest frequency vibration is due to the metal- CO_2 rock. Every fourth peak has a split feature, as the stretch frequency is not quite an integer multiple of the rocking frequency. The long progressions observed in the metal-ligand rock and, to a lesser extent, rock indicate that the TiO^+ electronic state substantially affects its interaction with CO_2 . This will be explored in more detail with the aid of electronic structure calculations. It is also interesting to compare the photodissociation spectrum of $\text{TiO}^+(\text{CO}_2)$ to that of isoelectronic $\text{ZrO}^+(\text{CO}_2)$ obtained by Bellert et al.²² The spectra are very similar. They observe a progression in the Zr-O covalent stretch ($\omega'_{\text{ZrO}}=891 \text{ cm}^{-1}$, $x'_{\text{ZrO}}=3.4 \text{ cm}^{-1}$), as well as the metal- CO_2 stretch ($\omega'_{\text{stretch}}=173 \text{ cm}^{-1}$) and rock ($\omega'_{\text{rock}}=39 \text{ cm}^{-1}$). These values are very similar to those we observe for $\text{TiO}^+(\text{CO}_2)$. The titanium complex does, however show a more extensive progression in the rock, indicating that electronic excitation of TiO^+ results in a larger change in the orientation of CO_2 ligand.

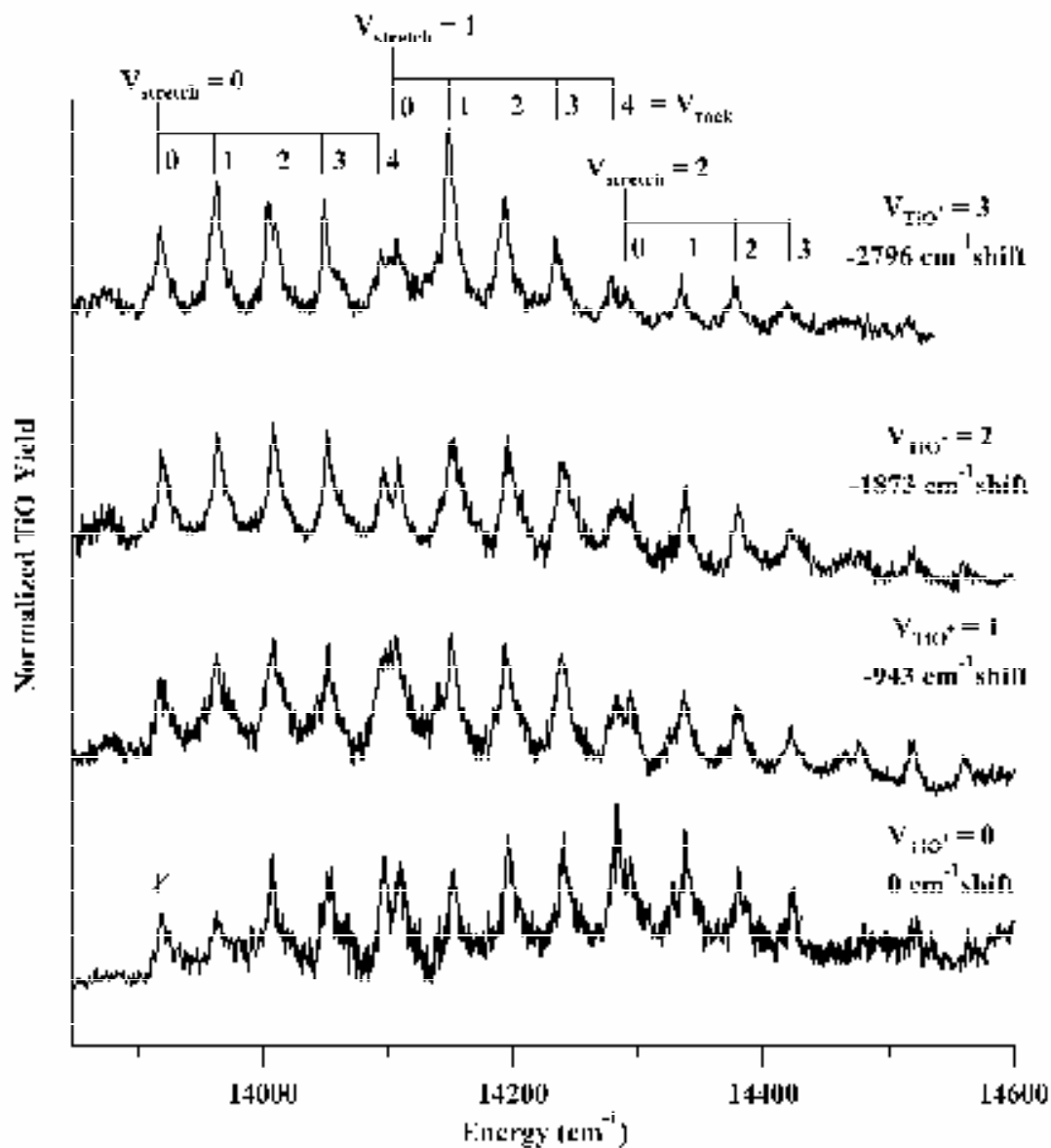


Figure 3.4: Overlapped photodissociation spectrum of $\text{TiO}^+(\text{CO}_2)$. Bands corresponding to the covalent Ti-O stretch $v_{\text{TiO}} = 0$ to 4 are shifted to allow comparison of the low-frequency metal- CO_2 stretch and rock. The low-frequency vibrations are essentially independent of v_{TiO} .

The shape of the fragment peak in the time-of-flight spectrum is sensitive to dissociation dynamics and kinetics. Substantial kinetic energy release leads to peak broadening, while slow dissociation leads to peak tailing. Figure 3.5 shows the TiO^+ fragment peak from photodissociation of $\text{TiO}^+(\text{CO}_2)$ at 14204 and 14925 cm^{-1} . The 14204 cm^{-1} spectrum shows clear tailing, which is much reduced at 14925 cm^{-1} . The lifetimes of the photoexcited molecules are determined by comparing experimental and simulated²⁵ fragment time-of-flight profiles. Excited state lifetimes measured at several photon energies covering $\nu_{\text{Ti-O}}=0-4$ are listed in table 3.1. The lifetime drops rapidly with increasing photon energy, until no tailing is observed at energies above 16500 cm^{-1} , indicating lifetimes below 50 ns.

Energy (cm^{-1})	Lifetime (ns)	Dissociation rate (s^{-1})
14204	1100	9×10^5
14925	120	8×10^6
15798	60	1.7×10^7
16722	≤ 50	$\geq 2 \times 10^7$

Table 3.1: Excited state lifetimes for several vibronic states of $\text{TiO}^+(\text{CO}_2)$. The lifetimes are measured from fits to tailing in the TiO^+ fragment time-of-flight spectrum, as shown in figure 3.5.

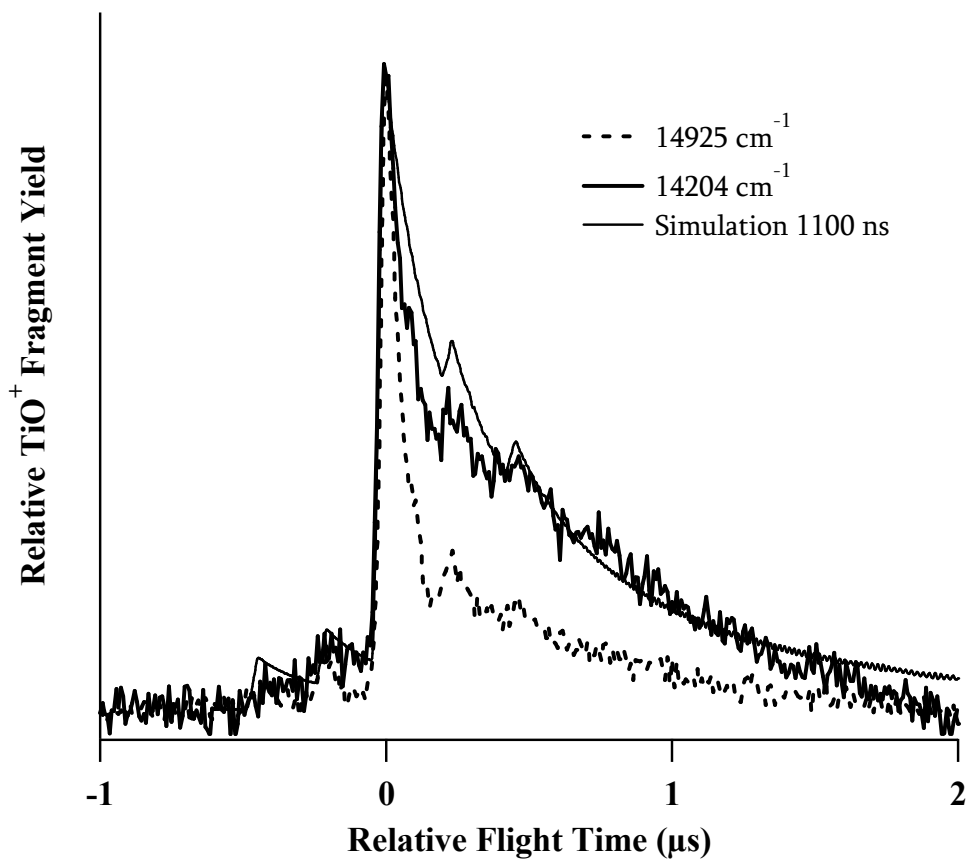


Figure 3.5: Time-of-flight spectra of TiO^+ from photodissociation of $\text{TiO}^+(\text{CO}_2)$ at 14204 and 14925 cm^{-1} . Tailing in the 14204 cm^{-1} spectrum indicates a lifetime of 1100 ns , which drops to 120 ns at 14925 cm^{-1} . The small peaks in the spectra are due to photodissociation of minor isotopomers.

3.3.2 Calculations

Electronic structure calculations were carried out on TiO^+ and $\text{TiO}^+(\text{CO}_2)$ to determine which state of the TiO^+ chromophore is responsible for the observed spectrum, as well as to try to explain the photodissociation mechanism and the broad range of dissociation lifetimes. In addition, by calculating how the CO_2 affects the vibrational frequencies and electronic spectroscopy of TiO^+ , we can use our experimental results on $\text{TiO}^+(\text{CO}_2)$ to predict the electronic spectrum of bare TiO^+ in the visible. Calculations were carried out using the B3LYP hybrid density functional method, with the 6-311+G(d) basis set, using *Gaussian03*.²⁶ At this level of theory, bare TiO^+ is predicted to have a $^2\Delta$ ground state, with the electron configuration $8\sigma^2, 3\pi^4, 1\delta^1$ and $r_e=1.570 \text{ \AA}$. To characterize excited electronic states, time-dependent density functional theory (TD-DFT) calculations were carried out, at the B3LYP/6-311+G(d) level. There are two low-lying excited states: the $^2\Sigma$ state is formed by promotion of the 1δ electron to the 9σ orbital (see figure 3.1); promotion to the 4π orbital produces the $^2\Pi$ state. Figure 3.6 shows scans along the Ti-O stretch for the ground and low-lying doublet states of TiO^+ . Spectroscopic parameters obtained by solving the Schrodinger equation on the one-dimensional stretching potential are given in table 3.2. Transitions from the $^2\Delta$ ground state to the $^2\Sigma$ excited state are symmetry forbidden. Transitions to the $^2\Pi$ state are calculated to have an integrated oscillator strength $f= 0.0050$.

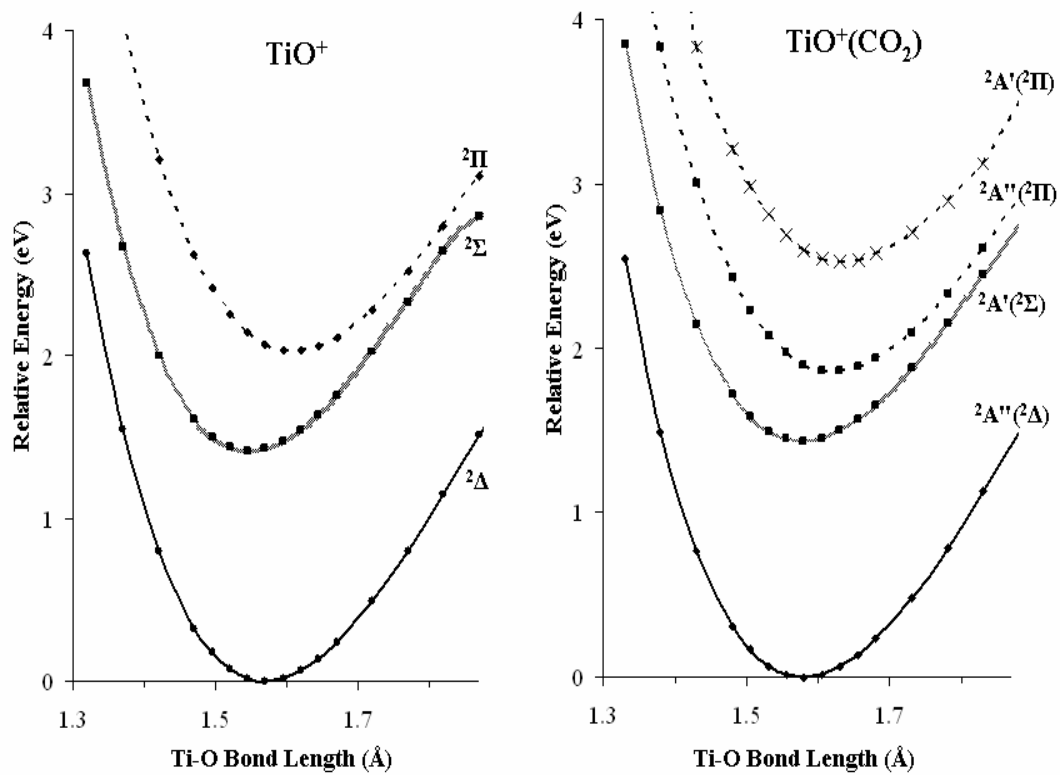


Figure 3.6: Calculated potential energy curves for doublet states of TiO^+ and $\text{TiO}^+(\text{CO}_2)$ along the covalent Ti-O stretch. Points are calculated using TD-DFT at the B3LYP/6-311+G(d,p) level. Electronic states of $\text{TiO}^+(\text{CO}_2)$ are also labeled by the corresponding state of bare TiO^+ .

State	w_e	$w_e x_e$	T_e	T_0
${}^2\Delta_{\text{harmonic}}$	1122.1	0	0	0
${}^2\Delta$	1122.5	4.18	0	0
${}^2\Sigma$	1130.9	4.84	11399	11403
${}^2\Pi$	1049.6	3.89	16385	16348

Table 3.2: Spectroscopic parameters for the ground and low-lying excited states of TiO^+ from TD-DFT calculations at the B3LYP/6-311+G(d) level. The first row is a harmonic frequency. Other rows are anharmonic frequencies from the potentials in figure 3.6. All values in cm^{-1} .

The $\text{TiO}^+(\text{CO}_2)$ complex is calculated to be planar. Binding to CO_2 lengthens the covalent Ti-O bond by 0.010 Å, to 1.580 Å. The noncovalent OTi-OCO bond length is 2.19 Å, and the complex is bent, with an O-Ti-(OCO) angle of 107°. The CO_2 is bound by 8000 cm^{-1} . Figure 3.6 shows scans of excited states of $\text{TiO}^+(\text{CO}_2)$ along the covalent Ti-O stretch. Interaction with CO_2 splits the ${}^2\Pi$ excited state of TiO^+ into two states. The lower-energy state corresponds to an electron in the out-of-plane π orbital, resulting in less repulsion with CO_2 than promotion to the in-plane π orbital. Binding to the CO_2 lowers the symmetry, so transitions to the ${}^2A'$ (${}^2\Sigma$) state are no longer forbidden, but are weak with $f \approx 0.0007$. The low-energy ${}^2A''$ component of the ${}^2\Pi$ state retains significant oscillator strength ($f \approx 0.0057$), while the ${}^2A'$ component has $f \approx 0$. Calculated spectroscopic parameters for the covalent Ti-O stretch in $\text{TiO}^+(\text{CO}_2)$ are given in table 3.3. Calculated harmonic vibrational frequencies for the ground state of $\text{TiO}^+(\text{CO}_2)$ are in table 3.4.

State	ω_e	$\omega_e x_e$	T_e	T_0
${}^2A''$ (${}^2\Delta$), harmonic	1106	0	0	0
${}^2A''$ (${}^2\Delta$)	1103.5	3.16	0	0
${}^2A'$ (${}^2\Sigma$)	1062.4	3.31	11552	11531
${}^2A'$ (${}^2\Pi$)	1033.5	3.96	14992	14957

Table 3.3: Spectroscopic parameters for the ground and low-lying excited states of $\text{TiO}^+(\text{CO}_2)$ from TD-DFT calculations at the B3LYP/6-311+G(d) level. The first row is a harmonic frequency. Other rows are anharmonic frequencies from the potentials in Figure 6. All values in cm^{-1} . Electronic states of $\text{TiO}^+(\text{CO}_2)$ are also labeled by the corresponding state of bare TiO^+ in parentheses. Interaction with CO_2 splits the 2P state into two components. Parameters are not given for the upper ${}^2A''$ (2P) state.

Assignment	Frequency (cm^{-1})
CO_2 antisymmetric stretch	2458
CO_2 symmetric stretch	1377
CO_2 bend	639 and 647
Covalent Ti-O stretch	1106
OTi-(OCO) stretch	255
OTi-(OCO) rock	53, 100 and 132

Table 3.4: Calculated vibrational frequencies of ground state $\text{TiO}^+(\text{CO}_2)$ at the B3LYP/6-311+G(d) level.

3.4 Discussion

The photodissociation spectrum of $\text{TiO}^+(\text{CO}_2)$ has an origin at 13918 cm^{-1} and shows extensive progressions in the covalent Ti-O stretch ($\omega'_{\text{TiO}}=952 \text{ cm}^{-1}$ with anharmonicity $x'_{\text{TiO}}=5 \text{ cm}^{-1}$), and the metal- CO_2 stretch and rock (186 and 45 cm^{-1} , respectively). The calculations predict two states of $\text{TiO}^+(\text{CO}_2)$ in this region: the ${}^2\text{A}'$ (${}^2\Sigma$) and ${}^2\text{A}'$ (${}^2\Pi$) states. Transitions to the ${}^2\text{A}'$ (${}^2\Sigma$) state are predicted to be about an order of magnitude weaker than those to the ${}^2\text{A}'$ (${}^2\Pi$) state. Since we observe only one electronic transition, it is assigned to the ${}^2\text{A}'$ (${}^2\Pi$) state. This state is at an adiabatic energy of $T_e=14877 \text{ cm}^{-1}$, if the excited state geometry is optimized. Photoexcitation of $\text{TiO}^+(\text{CO}_2)$ to this state is calculated to increase the covalent Ti-O bond length by 0.04 \AA , decrease the OTi-OCO bond length by 0.04 \AA , and decrease the O-Ti-OCO angle by 13° . These geometry changes would lead to progressions in the covalent Ti-O stretch, and the metal- CO_2 stretch and bend, as observed. The calculation slightly over-estimates the covalent TiO stretch frequency, predicting $\omega'_{\text{TiO}}=1033.5 \text{ cm}^{-1}$ with anharmonicity $x'_{\text{TiO}}=4 \text{ cm}^{-1}$.

The TiO^+ cation is an astronomically interesting molecule. The TiO neutral has been detected near numerous stars and its presence is used to identify cool M and S class stars. Neutral TiO is detected based on absorption in three strong electronic transitions in the visible. The resulting rotational structure is used to measure the local temperature. The low ionization energy of TiO and high bond strength of TiO^+

make it likely that it is present in circumstellar envelopes. The electronic spectrum of TiO^+ has not been measured, which clearly hampers its detection. The high Ti⁺-O bond strength also makes it difficult to detect via photofragment spectroscopy. We would like to use our calculations on TiO^+ and $\text{TiO}^+(\text{CO}_2)$, as well as experimental results on $\text{TiO}^+(\text{CO}_2)$, to predict the electronic spectroscopy of bare TiO^+ . The calculations indicate that binding to CO_2 affects the $^2\Pi$ state of TiO^+ : lowering ω_e by 16 cm^{-1} and T_e by 1508 cm^{-1} . For $\text{TiO}^+(\text{CO}_2)$, we measure $T_0=13918\text{ cm}^{-1}$ and $\omega'_{\text{TiO}}=952\text{ cm}^{-1}$ with anharmonicity $x'_{\text{TiO}}=5\text{ cm}^{-1}$. We would then predict that the $^2\Pi$ state of TiO^+ has $\omega_e=968\text{ cm}^{-1}$ with anharmonicity $\omega_e x_e=5\text{ cm}^{-1}$, and lies at $T_0=15426\text{ cm}^{-1}$. The estimated value of T_0 ignores differences in zero-point energy between the two states. These values are very close to recent very high level multi-reference calculations by Miliordos <ref – A. Miliordos, private communication, 2008>. Astronomical identification of TiO^+ would require accurate laboratory frequencies, but these values provide an excellent starting point for laboratory studies of TiO^+ , perhaps by sensitive absorption techniques such as cavity ring-down spectroscopy.

The calculations predict that TiO^+ ($X, ^2\Delta$) binds CO_2 by 8000 cm^{-1} . The calculated 1508 cm^{-1} red shift for excitation to the $^2A'$ ($^2\Pi$) state indicates that the $^2\Pi$ state of TiO^+ binds CO_2 more strongly, by $\sim 9500\text{ cm}^{-1}$. This stronger interaction is also consistent with the calculated reduction in the OTi-OCO bond length upon photoexcitation. Despite this strong binding, interaction with the CO_2 only slightly affects the vibrational frequency of TiO^+ .

Current spectroscopic information on TiO^+ is from photoelectron spectroscopy of TiO by Dyke and co-workers and Weisshaar and co-workers. They agree on the ground ${}^2\Delta$ state of TiO^+ . Dyke and co-workers also observe a band at $T_0=10250\pm 80\text{cm}^{-1}$ with $\omega_e=860\pm 60\text{cm}^{-1}$ and $r_e=1.73\pm 0.01\text{ \AA}$, which they assign to the $A, {}^2\Sigma^+$ state.¹² Weisshaar and co-workers observe an excited ${}^2\Sigma^+$ state with $T_0=11227\pm 17\text{cm}^{-1}$, $\omega_e=1020\pm 9\text{cm}^{-1}$, and anharmonicity $\omega_e x_e=6\pm 2\text{cm}^{-1}$.¹³ Although this state lies at a similar energy to the ${}^2\Sigma$ observed by Dyke and co-workers, the very different vibrational frequencies led Weisshaar and co-workers to propose that TiO^+ has two distinct low-lying ${}^2\Sigma$ states, and resonant two-photon ionization reaches one state, while one-photon ionization reaches another. Our photodissociation study of $\text{TiO}^+(\text{CO}_2)$ probes the ${}^2\Pi$ state of TiO^+ . This state has the electron configuration $8\sigma^2, 3\pi^4, 4\pi^1$ and thus can't be reached by simply removing an electron from neutral TiO , so it was not observed by Dyke and co-workers. The multiphoton ionization study of Weisshaar and co-workers used several intermediate electronic states of TiO , so they could conceivably ionize to the ${}^2\Pi$ state of TiO^+ , but their study did not extend to sufficiently high energies. However, our calculations shed light on the ${}^2\Sigma$ states observed by photoelectron spectroscopy. The TD-DFT calculations predict *one* low-lying ${}^2\Sigma$ state of TiO^+ , at $T_0=11403\text{ cm}^{-1}$ with $\omega_e=1131\text{ cm}^{-1}$ and $\omega_e x_e=5\text{ cm}^{-1}$ and $r_e=1.55\text{ \AA}$. These values are in excellent agreement with the values for the 2S state observed by Weisshaar and co-workers. The next ${}^2\Sigma$ state is predicted to lie at much higher energy, with $T_e=30600\text{ cm}^{-1}$. It is not clear why the one-photon photoelectron

spectrum of TiO leads to such a low predicted vibrational frequency for the A $^2\Sigma$ state of TiO⁺. One possibility is that the high temperature (~800 K) of the molecules and modest spectral resolution lead to overlapping vibrational bands that are easily mis-assigned.

The slow dissociation and wide range of dissociation lifetimes observed for TiO⁺(CO₂) is unusual for a molecule this small. Photoexcitation of TiO⁺(CO₂) initially produces [TiO⁺(CO₂)]^{*} $^2A''$ ($^2\Pi$). Dissociation requires internal conversion or intersystem crossing to a lower-lying electronic state followed by intermolecular vibrational relaxation (IVR) to transfer sufficient energy into the OTi-OCO stretch to dissociate the complex. Intersystem crossing does not contribute since the lowest quartet state is calculated to lie above the photon energy. We can use a statistical model to predict whether internal conversion or IVR is the rate-limiting step. If internal conversion of [TiO⁺(CO₂)]^{*} to highly vibrationally excited TiO⁺(CO₂) in its ground electronic state is rapid, then the statistical RRKM model can then be used to predict the unimolecular dissociation rate of the energized complex. Using computed vibrational frequencies (table 3.4) and the computed TiO⁺-CO₂ binding energy of 8000 cm⁻¹, the statistical dissociation rate is $3 \times 10^{10} \text{ s}^{-1}$ at a photon energy of 14000 cm⁻¹. Even increasing the binding energy to 10000 cm⁻¹, the dissociation rate is $3 \times 10^9 \text{ s}^{-1}$ at 14000 cm⁻¹. This is over 3 orders of magnitude faster than is observed. Thus, these calculations predict that IVR is rapid and internal conversion is the rate-limiting step.

This suggests that TiO^+ ($^2\Pi$) may fluoresce, which provides an additional route for laboratory studies.

3.5 Conclusion

Photofragment spectroscopy of $\text{TiO}^+(\text{CO}_2)$ has been used to characterize the $^2A''$ ($^2\Pi$) excited state. These measurements, along with calculations on TiO^+ and $\text{TiO}^+(\text{CO}_2)$ allow for the prediction of the excitation energy and vibrational frequency of the $^2\Pi$ state of TiO^+ . Astronomical observation of TiO^+ in circumstellar envelopes may be possible via the $^2\Delta$ - $^2\Pi$ electronic transition in the visible. Photoexcited $\text{TiO}^+(\text{CO}_2)$ shows a wide range of dissociation lifetimes, which is likely due to slow internal conversion at lower energies.

3.6 References

- (1) Langhoff, S. R. *Astrophys. J.* **1997**, *481*, 1007.
- (2) McLaughlin, B. M.; Ballance, C. P.; Berrington, K. A. *J. Phys. B-At. Mol. Opt. Phys.* **2001**, *34*, L179.
- (3) Bauschlicher, C. W., Jr.; Maitre, P. *Theor. Chim. Acta* **1995**, *90*, 189.
- (4) Burrows, A.; Dulick, M.; Bauschlicher, C. W., Jr.; Bernath, P. F.; Ram, R. S.; Sharp, C. M.; Milsom, J. A. *Astrophys. J.* **2005**, *624*, 988.
- (5) Kim, J. H.; Ishihara, A.; Mitsushima, S.; Kamiya, N.; Ota, K. I. *Electrochim. Acta* **2007**, *52*, 2492.
- (6) Eller, K.; Schwarz, H. *Chem. Rev.* **1991**, *91*, 1121.
- (7) Schröder, D.; Schwarz, H. *Angew. Chem. Int. Ed. Engl.* **1995**, *34*, 1973.
- (8) Böhme, D. K.; Schwarz, H. *Angew. Chem., Int. Ed. Engl.* **2005**, *44*, 2336.
- (9) Clemmer, D. E.; Aristov, N.; Armentrout, P. B. *J. Phys. Chem.* **1993**, *97*, 544.
- (10) Koyanagi, G. K.; Bohme, D. K. *J. Phys. Chem. A* **2006**, *110*, 1232.
- (11) Armentrout, P. B.; Kickel, B. L. Gas-Phase Thermochemistry of Transition Metal Ligand Systems: Reassessment of Values and Periodic Trends. In *Organometallic Ion Chemistry*; Freiser, B. S., Ed.; Kluwer Academic Publishers: Dordrecht, The Netherlands, 1994; pp 1.
- (12) Dyke, J. M.; Gravenor, B. W. J.; Josland, G. D.; Lewis, R. A.; Morris, A. *Mol. Phys.* **1984**, *53*, 465.
- (13) Sappey, A. D.; Eiden, G.; Harrington, J. E.; Weisshaar, J. C. *J. Chem. Phys.* **1989**, *90*, 1415.

- (14) Bellert, D.; Buthelezi, T.; Brucat, P. J. *Chem. Phys. Lett.* **1998**, *290*, 316.
- (15) Asher, R. L.; Bellert, D.; Buthelezi, T.; Brucat, P. J. *Chem. Phys. Lett.* **1994**, *227*, 623.
- (16) Asher, R. L.; Bellert, D.; Buthelezi, T.; Weerasekera, G.; Brucat, P. J. *Chem. Phys. Lett.* **1994**, *228*, 390.
- (17) Citir, M.; Altinay, G.; Metz, R. B. *J. Phys. Chem. A* **2006**, *110*, 5051.
- (18) Citir, M.; Metz, R. B. *J. Chem. Phys.* **2008**, *128*, 024307 (10 pgs).
- (19) Gregoire, G.; Duncan, M. A. *J. Chem. Phys.* **2002**, *117*, 2120.
- (20) Duncan, M. A. *Int. Rev. Phys. Chem.* **2003**, *22*, 407.
- (21) Walker, N. R.; Walters, R. S.; Duncan, M. A. *J. Chem. Phys.* **2004**, *120*, 10037.
- (22) Bellert, D.; Buthelezi, T.; Hayes, T.; Brucat, P. J. *Chem. Phys. Lett.* **1997**, *276*, 242.
- (23) Metz, R. B. *Int. Rev. Phys. Chem.* **2004**, *23*, 79.
- (24) Metz, R. B. *Adv. Chem. Phys.* **2008**, *138*, 331.
- (25) Thompson, C. J.; Faherty, K. P.; Stringer, K. L.; Metz, R. B. *Phys. Chem. Chem. Phys.* **2005**, *7*, 814.
- (26) Frisch, M. J.; Trucks, G. W.; Schlegel, H. B.; Scuseria, G. E.; Robb, M. A.; Cheeseman, J. R.; Zakrzewski, V. G.; Montgomery, J. A.; Stratmann, R. E.; Burant, J. C.; Dapprich, S.; Millam, J. M.; Daniels, A. D.; Kudin, K. N.; Strain, M. C.; Farkas, O.; Tomasi, J.; Barone, V.; Cossi, M.; Cammi, R.; Mennucci, B.; Pomelli, C.; Adamo, C.; Clifford, S.; Ochterski, J.; Petersson, G. A.; Ayala, P. Y.; Cui, Q.; Morokuma, K.; Malick, D. K.; Rabuck, A. D.; Raghavachari, K.; Foresman, J. B.; Cioslowski, J.; Ortiz, J. V.; Stefanov, B. B.; Liu, G.; Liashenko, A.; Piskorz, P.; Komaromi, I.; Gomperts, R.; Martin, R. L.; Fox, D. J.; Keith, T.; Al-Laham, M. A.; Peng, C. Y.; Nanayakkara, A.; Gonzalez, C.; Challacombe, M.; Gill, P. M. W.; Johnson, B. G.; Chen, W.; Wong, M. W.; Andres, J. L.;

Head-Gordon, M.; Replogle, E. S.; Pople, J. A. Gaussian 98; Revision A.3 ed.; Gaussian, Inc.: Pittsburgh PA, 1998.

CHAPTER 4

MICROSOLVATION OF Ni²⁺ AND Co²⁺ BY ACETONITRILE AND WATER:

PHOTODISSOCIATION DYNAMICS OF M²⁺(CH₃CN)_n(H₂O)_m

4.1 Introduction

Transition metals make human blood red and crustacean blood blue. This colorful character makes d-block elements useful as pigments in dyes and paints and also gives precious gems like rubies their beautiful color. Transition metals are vital to the physiology of living organisms. For example, cobalt is imperative for vitamin B₁₂ activity and copper and zinc are widely used metals in biological systems. Also, transition metal ligation/solvation is a key aspect of homogeneous catalysis. Studying metal ion solvation leads to a better understanding of transition metal chemistry and catalysis as well as providing functional and structural information on biological molecules in which these metals interact.

There is much that is not yet known about the interaction of transition metals with different solvents. In solution, transition metals are typically multiply charged species such as M²⁺ and M³⁺. Transition metal cations have a strong attraction to solvent molecules, due to their partially filled d-orbitals and characteristic multiple charges. Most studies of ion-ligand interactions have been in solution.¹ However, it is really difficult to differentiate the influence of the solvent molecules in the first

solvent shell from the second shell in solution. In contrast to solution, gas phase studies allow for better control of the environment around the metal ion. Gas phase clusters can be made with a known number of solvent molecules, and gas phase studies eliminate bulk effects due to outer-shell solvent molecules. The number of solvent molecules needed to stabilize the metal dication depends on the type of solvent. Typically, the preferred coordination number in solution is six for water but gas phase complexes with four water molecules are readily produced.² Furthermore, the gas phase offers better control over the type of solvent that binds to the metal dication when different solvents are present. For example this study focuses on mixed $M^{2+}(\text{CH}_3\text{CN})_n(\text{H}_2\text{O})_m$ clusters. These features make the gas phase an ideal medium to study fundamental ion-ligand interactions.³⁻⁶

Singly charged transition metals tend to be the focus of much of the gas phase studies due to the convenience of producing them.^{6,7} Also, singly charged complexes are stable since metals have significantly lower first ionization energies than most solvent molecules. However, in the condensed phase many transition metals in chemistry and biology are found in their more characteristic multiply charged states.⁸ This is a compelling reason to produce and study multiply charged clusters in the gas phase. The second ionization potential of metals is much higher than the first ionization potential, making it challenging to generate multiply charged ions.³ For example, nickel's second ionization energy is 18.17 eV which is 10.53 eV higher than the first ionization energy. Similarly, the energy difference between the second and

first ionization of cobalt is 9.2 eV. With Fenn's introduction of electrospray, efficient production of solvated, multiply charged ions became a possibility.⁹

Microsolvated multiply charged metal ions can be excited by energetic collisions or, in our experiment, absorption of light. The microsolvated metal ion must first absorb a photon which has sufficient energy to break a bond leading to dissociation. Charged fragments are detected by their characteristic flight time in the mass spectrometer. In addition to identifying dissociation pathways, photofragment spectra can yield both dynamic and kinetic information about the dissociation process. Metal ion clusters follow different dissociation pathways as the number of solvents increase; the relative yield of different fragments also changes with wavelength. The larger clusters lose one or more solvent molecules, whereas smaller clusters show charge reduction or heterolytic bond cleavage. In charge reduction, the doubly charged parent ion will make two fragment ions that are singly charged via proton transfer or electron transfer.

Earlier work in our lab has determined the dissociation pathways, mechanisms and bond dissociation thresholds for Co^{2+} and Ni^{2+} solvated by 4 to 7 water and methanol molecules.¹⁰⁻¹² Both are protic solvents with the ability to hydrogen bond outer shell solvent molecules to those in the inner shell. To extend the solvation study we will move away from the protic solvents to understand the effects of aprotic solvents such as acetonitrile. Previous studies using Collision Induced Dissociation (CID) have shown that proton transfer is much less favorable for aprotic solvents,

narrowing the major charge reduction pathway exclusively to electron transfer and allowing for the production of smaller clusters.¹³⁻¹⁵

Even though acetonitrile and water have similar ionization energies, the dipole moment of acetonitrile is more than two times higher than that of water, as shown in table 4.1. The polarizability of acetonitrile is over thrice that of water which is only 1.4 Å³. So, acetonitrile interacts more strongly with M²⁺ than water. As a result, stable smaller clusters can be produced. Smaller clusters show more interesting dissociation dynamics and kinetic energy release than larger clusters.

Ligand	IE (eV)	μ (D)	α (Å ³)
Water	12.62	1.8	1.4
Acetonitrile	12.19	3.9	4.4

Table 4.1: The physical properties of acetonitrile and water show that acetonitrile is a better solvent for gas phase cations.

4.2 Experimental Approach

The experimental apparatus, a dual time-of-flight photofragment mass spectrometer, is described in chapter 2 in detail and also in the literature.¹⁶ The multiply charged metal clusters are produced with an electrospray source (ESI) outside the instrument and introduced to the vacuum chamber through a capillary. A 10⁻³–10⁻⁴ M solution of the appropriate M²⁺ salt, Co(NO₃)₂ or Ni(NO₃)₂, in the solvent of interest flows through a stainless steel needle held at a high voltage (4.5-5.5 kV).

Nitrate salts were used for the acetonitrile studies, as chlorides and sulfates did not dissolve. To control the water content, the salts were vacuum dried overnight and the acetonitrile was dried using molecular sieves for at least 24 hrs. It was necessary to use salts and acetonitrile that was free of water to produce small $M^{2+}(CH_3CN)_n$ clusters. For the mixed clusters, the solvent mix is changed depending on the ion cluster we are interested in studying. A 1:13 ratio of acetonitrile to water is used to generate $M^{2+}(CH_3CN)_2(H_2O)_2$ and a 1:100 ratio is used to generate $M^{2+}(CH_3CN)_2(H_2O)$. As the water content increases in the solvent mixture, the needle voltage also needs to be increased.

Normally, the desolvating capillary is kept below 0.1 kV. The desolvating capillary¹⁷ is typically heated to 50-60 °C to aid in desolvating the clusters. Once they reach the source chamber, the ions travel through an ion funnel¹⁸ before heading to the next low pressure chamber. The alternating plates of the ion funnel have phase-shifted RF of 30-40 V peak-to-peak at 1MHz frequency and a DC gradient: 12 V on first plate, 30 V on last plate. Using this technique, we are able to significantly improve the ion beam intensity, thus allowing us to study challenging ions such as smaller clusters.

The ion funnel focuses the ions through a differential pumping aperture and into the second differential region where they enter the first octopole guide (OIG). The first OIG is floating at a 10 V DC potential and alternate rods carry 200 V peak-to-peak at ~1 MHz. The second octopole ion guide which has the same RF potential,

but has no DC bias, leads the ions to a radio frequency quadrupole ion trap. The front plate of the ion trap is held at (-) 10 to (+) 2 V to guide ions into the trap. The back plate carries a slightly more positive voltage than the front plate. The difference between the ion trap plate voltages was -1-2V for larger ions ($n>3$) and above -2 V for smaller ion clusters ($n=2$, and 3). The ions are trapped for up to 49 ms. During this time they collide with background gas of 1 mTorr of He which is added to the trap. These collisions cause the ions to thermalize to ~ 298 K. Ions are ejected from the trap with a pulsed voltage and are accelerated into the last differential region by a plate held at (-) 1800 V.

In this region, ions are re-referenced to ground potential, focused by an Einzel lens and guided by a pair of deflector plates into the field free flight tube. The ion of interest is mass selected from the entire ion beam in this region. The ion beam is then photo-excited at the turning point of the reflectron by the output of a pulsed (20 Hz) Nd:YAG-pumped dye laser with a line width of $<0.1\text{cm}^{-1}$ or by the 532 nm or 355 nm harmonics of a Nd:YAG laser. The fragments and parent ions are re-accelerated down the flight tube and detected by a dual micro-channel-plate detector and identified by their characteristic flight time. The resulting signal is amplified, collected on a digital scope and recorded digitally using a LabView-based program. The photodissociation spectra are obtained by monitoring the fragment ion yield as a function of wavelength and then normalizing to both the parent ion signal and laser power. Difference spectra are used to identify the fragment pathways at a given wavelength, and can

also show effects due to kinetic energy release and slow photodissociation. A home-built chopper wheel assists in producing a difference spectrum by allowing for the subtraction of laser-on spectra from laser-off mass spectra.

Calculations to complement the experimental work were conducted using B3LYP hybrid density function theory with the 6-311+G basis set using Gaussian 03.¹⁹ For each complex, the geometry was optimized and harmonic vibrational frequencies calculated to confirm the structure is a minimum. The energy includes the zero point energy and thus corresponds to 0 Kelvin values.

4.3 Results

Our primary interest in this study is the dissociation dynamics of transition metal dications solvated by acetonitrile and water. The fragment ions produced by photodissociation depend mainly on three conditions: (1) whether the solvents in the cluster are homogenous or heterogeneous, (2) the coordination number of the cluster, and (3) the photon energy provided by our photodissociation laser.

We were able to produce different combinations of mixed clusters with acetonitrile and water solvating Co^{2+} and Ni^{2+} . Other studies have shown that aprotic acetonitrile solvated metal ion clusters tend to favor specific numbers of solvent molecules, such as $\text{Ni}^{2+}(\text{CH}_3\text{CN})_6$ and $\text{Cu}^{2+}(\text{CH}_3\text{CN})_5$.¹³ However, we produced smooth cluster distributions, with no pronounced “magic number” with unusually high

intensity in the mass spectrum. Figure 4.1 shows mass spectra obtained by spraying 3×10^{-4} M solutions of $\text{Co}(\text{NO}_3)_2$ and $\text{Ni}(\text{NO}_3)_2$ in 1:20 $\text{CH}_3\text{CN}:\text{H}_2\text{O}$ and optimizing the yield of small clusters. Observed coordination numbers range from 2 to 5; lower capillary temperatures lead to larger clusters.

The photodissociation work was conducted at visible and ultra-violet wavelengths. None of the clusters dissociated at 355 nm. Photolysis deeper in the ultraviolet region, at 266 nm, produced no obvious fragments, although there was substantial background at this wavelength. In the visible, studies were carried out at 532 nm and at several wavelengths from 560 to 660 nm. Although the photodissociation yield depends on the visible wavelength, the observed products and dynamics do not, so only the 532 nm results are discussed. Clusters with coordination number greater than 4 dissociated by simple solvent loss. Mixed clusters preferentially lost the water molecule. Due to their richer photodissociation dynamics, this study specifically focuses on $\text{M}^{2+}(\text{H}_2\text{O})_n(\text{CH}_3\text{CN})_m$ ($\text{M}=\text{Co}, \text{Ni}$) clusters with coordination number $n+m=2$ through 4.

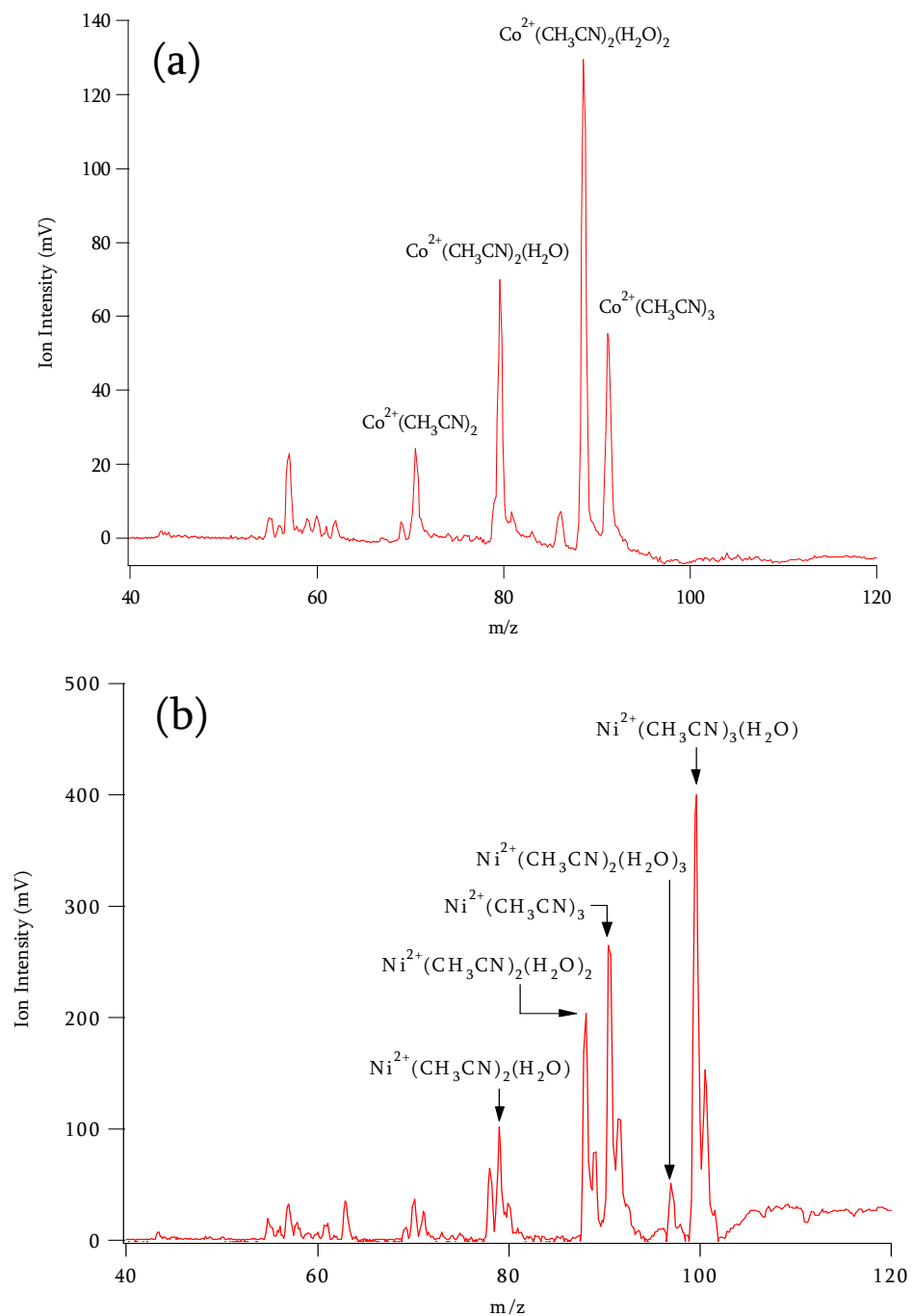
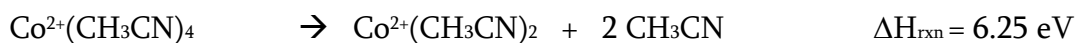
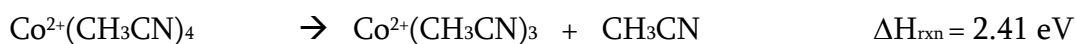


Figure 4.1: (a) Mass spectrum of $\text{Co}^{2+}(\text{CH}_3\text{CN})_n(\text{H}_2\text{O})_m$ clusters (b) Mass spectrum of $\text{Ni}^{2+}(\text{CH}_3\text{CN})_n(\text{H}_2\text{O})_m$. The peaks consist of doublets due to the two major isotopes of nickel, ^{58}Ni and ^{60}Ni , which are separated by one m/z unit as shown above.

4.3.1 Photodissociation Dynamics of Co²⁺ Complexes

4.3.1.1 Four Coordinate Complexes

Figure 4.2 (a) shows the difference spectrum of Co²⁺(CH₃CN)₄ at 532 nm. The only observed dissociation pathway is solvent loss. The major dissociation channel is the loss of one acetonitrile with a very minor channel for the loss of two acetonitrile. This minor channel was not observed for the nickel cluster (figure 4.2 b). Calculated (B3LYP/6-311+G) energies for the observed pathways are



A 532 nm photon has an energy of 2.33 eV. The observed experimental loss of an acetonitrile from Co²⁺(CH₃CN)₄ is calculated to require 2.41 eV. This is reasonable, considering the likely uncertainty in the calculated values. Also, all the experimental work was done at -298 K, so the internal vibrational energy of the parents (which is substantial, especially for the larger clusters) also contributes. The loss of two acetonitrile molecules produced a fragment that was significantly lower in photodissociation yield. This is because, as the calculation shows, absorption of three photons is required to promote this fragmentation.

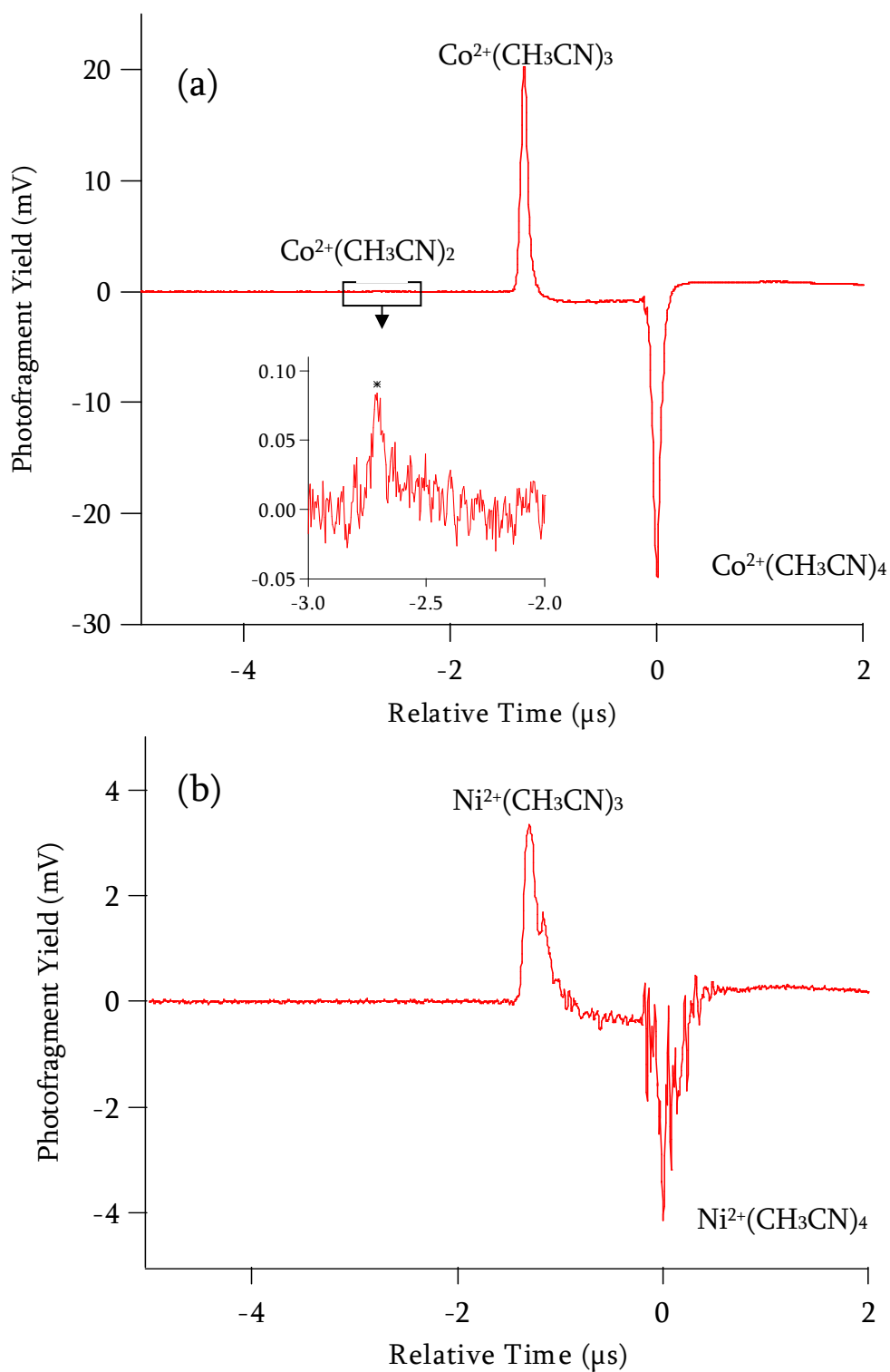
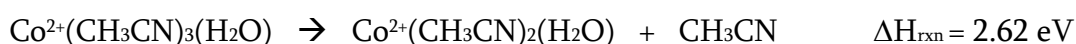
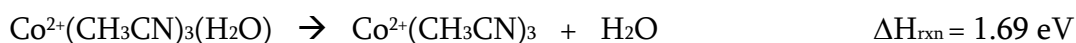


Figure 4.2: Difference spectra for $\text{Co}^{2+}(\text{CH}_3\text{CN})_4$ (top) and $\text{Ni}^{2+}(\text{CH}_3\text{CN})_4$ (bottom) at 532 nm. The fragment is due to simple solvent acetonitrile loss.

When one of the acetonitriles is replaced by a water molecule, $\text{Co}^{2+}(\text{CH}_3\text{CN})_3(\text{H}_2\text{O})$, the dissociation pathway that is observed is loss of water (figure 4.3 a). This cluster overwhelmingly loses water, which implies that acetonitrile is more strongly bound to Co^{2+} . This is due to its higher dipole moment and polarizability. This is supported by the calculations:



Loss of water from $\text{Co}^{2+}(\text{CH}_3\text{CN})_3(\text{H}_2\text{O})$ happens readily because it requires <2.33 eV. However, the loss of acetonitrile was not observed because that requires much more energy than water loss, and more than the energy of one photon from the dissociation laser.

The photodissociation of $\text{Co}^{2+}(\text{CH}_3\text{CN})_2(\text{H}_2\text{O})_2$ is dominated by solvent water loss, as shown in figure 4.4. However, two other minor pathways are observed: acetonitrile loss and proton transfer. Note that loss of acetonitrile is observed instead of loss of two water molecules. The two fragments made from proton transfer are protonated acetonitrile and the complementary singly charged metal hydroxide, $\text{CoOH}^+(\text{CH}_3\text{CN})(\text{H}_2\text{O})$. Figure 4.5 shows the proton transfer pathway is stronger for the Ni^{2+} than the Co^{2+} complex. Proton transfer was further studied with deuterated acetonitrile $\text{Co}^{2+}(\text{CD}_3\text{CN})_2(\text{H}_2\text{O})_2$ to see if the proton transferred is from acetonitrile or water. As shown in figure 4.6, the fragment observed is $\text{H}^+(\text{CD}_3\text{CN})$ rather than $\text{D}^+(\text{CD}_3\text{CN})$ indicating that the proton donor is the water molecule and not

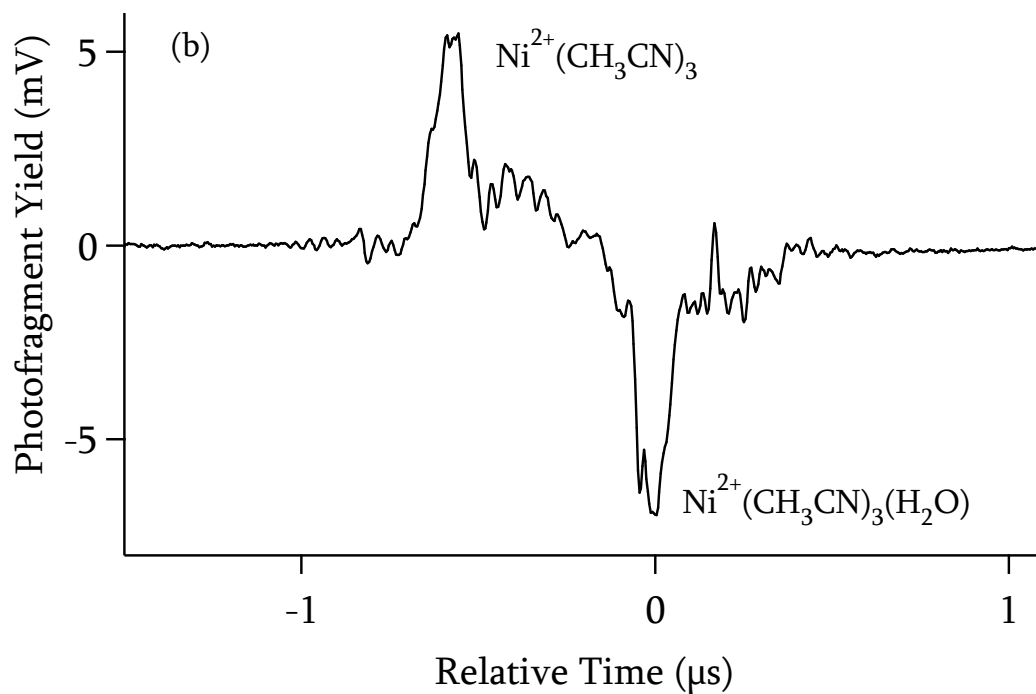
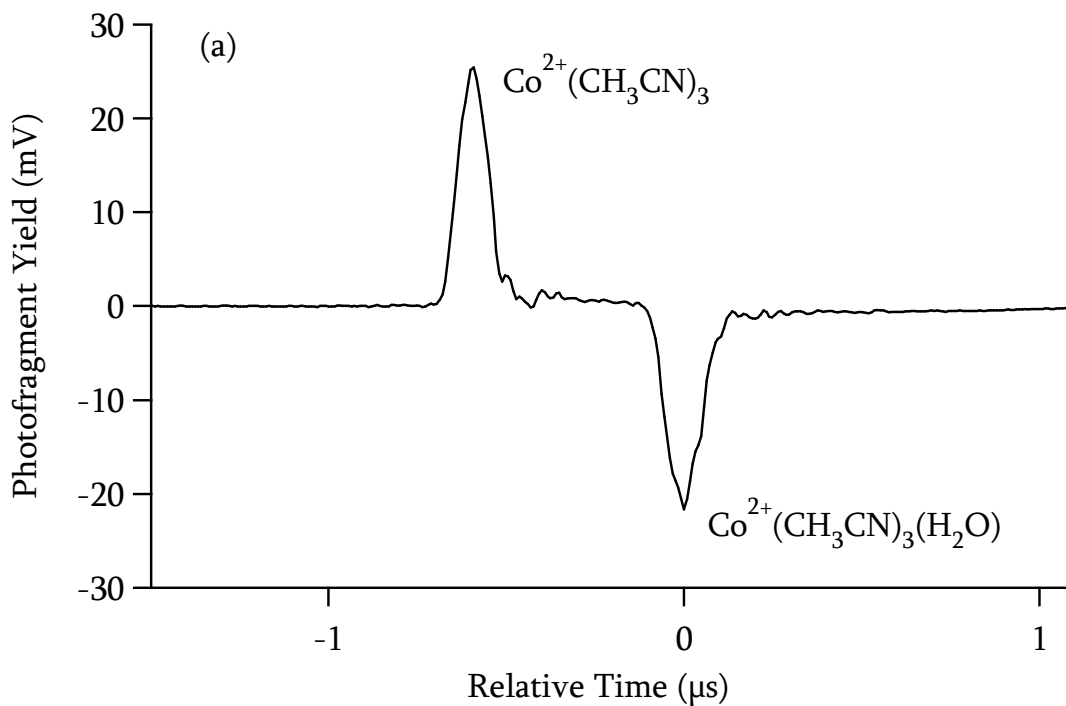


Figure 4.3: Difference spectra for $\text{Co}^{2+}(\text{CH}_3\text{CN})_3(\text{H}_2\text{O})$ (top) and $\text{Ni}^{2+}(\text{CH}_3\text{CN})_3(\text{H}_2\text{O})$ (bottom) at 532 nm. The fragment is due to simple solvent, water, loss.

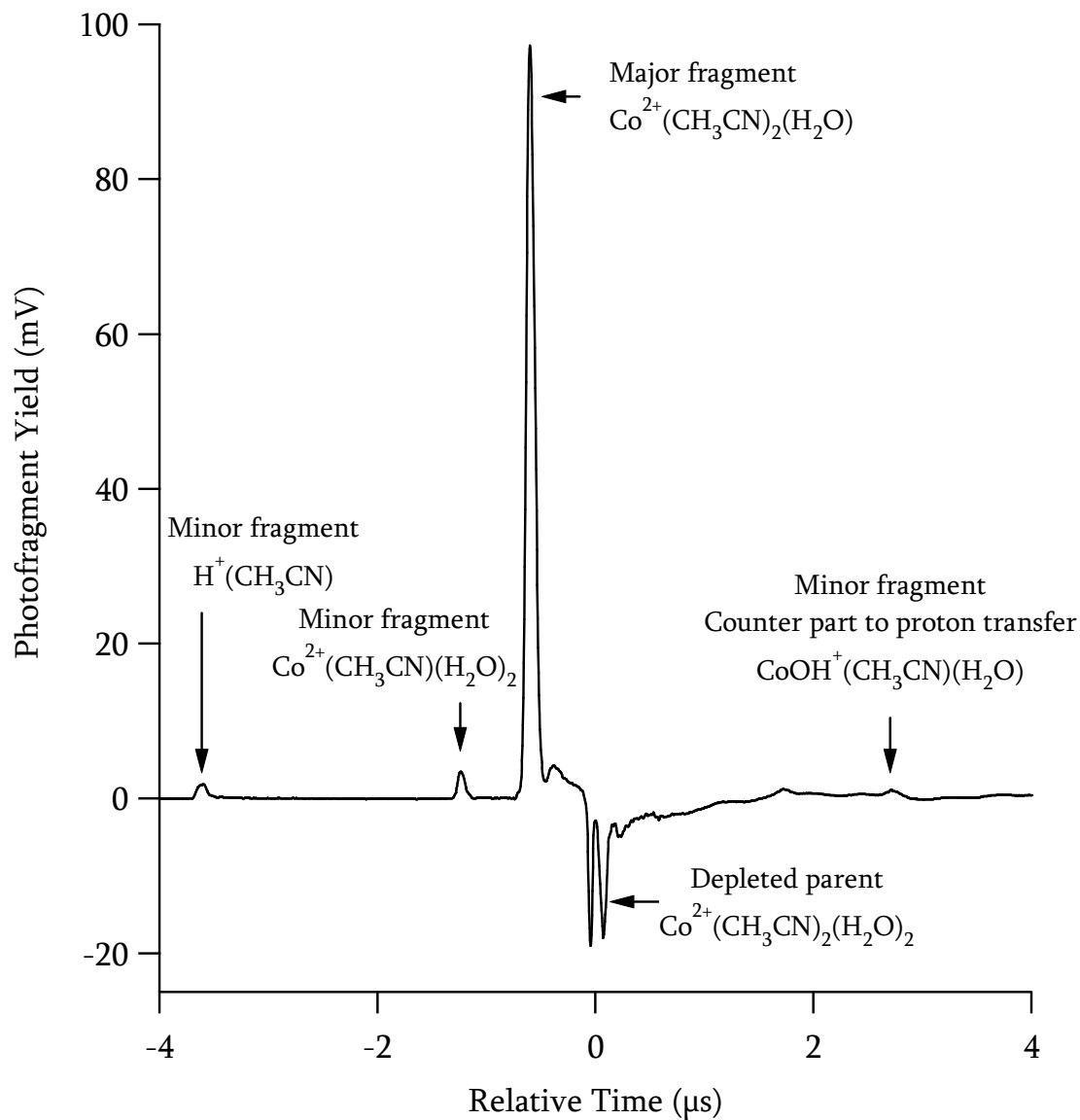


Figure 4.4: Difference spectrum for $\text{Co}^{2+}(\text{CH}_3\text{CN})_2(\text{H}_2\text{O})_2$ shows three dissociation pathways. The major channel is solvent water loss. Loss of solvent acetonitrile and proton transfer are minor channels.

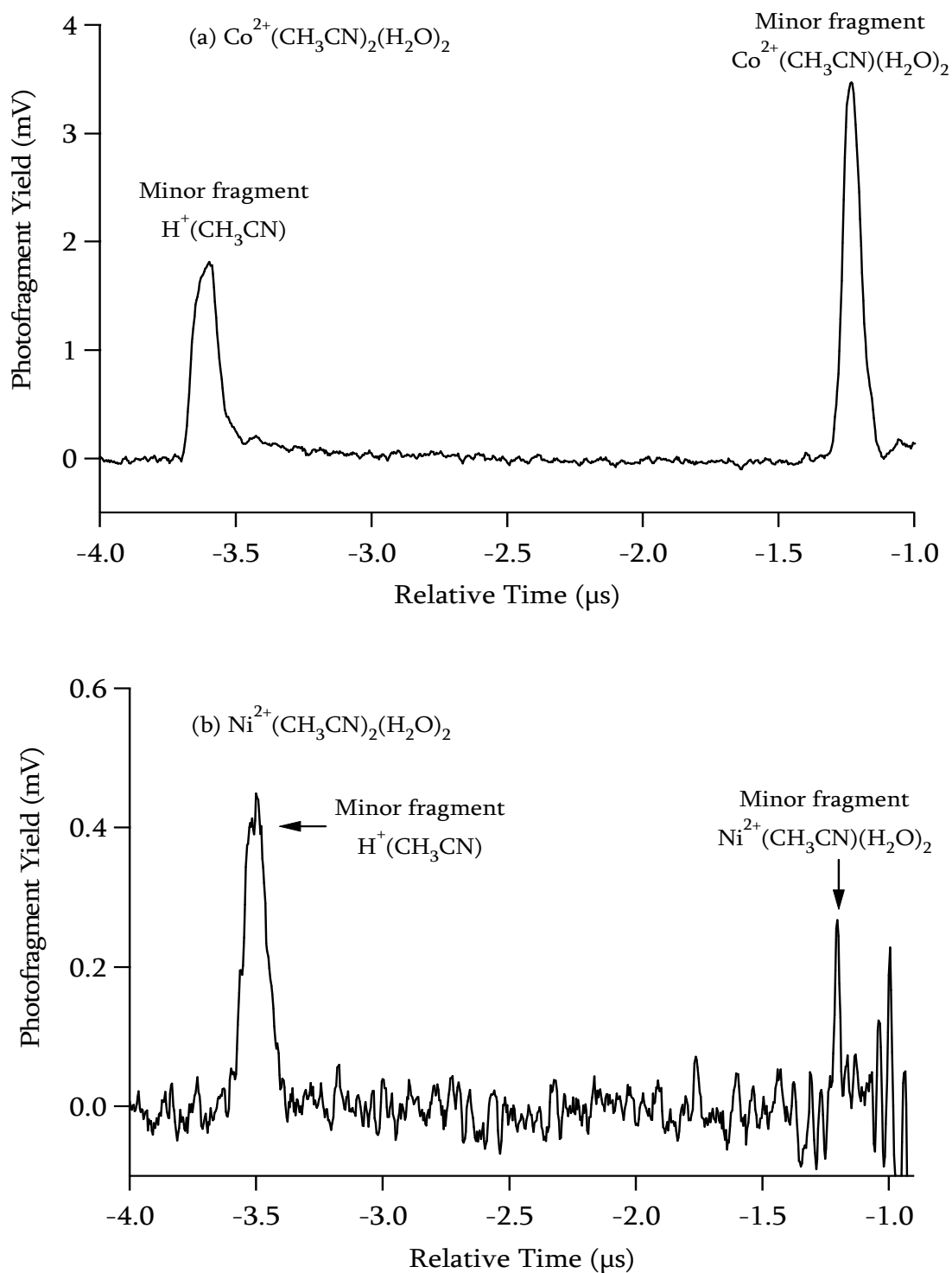


Figure 4.5: As seen in the difference spectra of (a) $\text{Co}^{2+}(\text{CH}_3\text{CN})_2(\text{H}_2\text{O})_2$ and (b) $\text{Ni}^{2+}(\text{CH}_3\text{CN})_2(\text{H}_2\text{O})_2$ the minor pathways yields are different. $\text{Ni}^{2+}(\text{CH}_3\text{CN})_2(\text{H}_2\text{O})_2$ favors proton transfer while $\text{Co}^{2+}(\text{CH}_3\text{CN})_2(\text{H}_2\text{O})_2$ prefers acetonitrile loss.

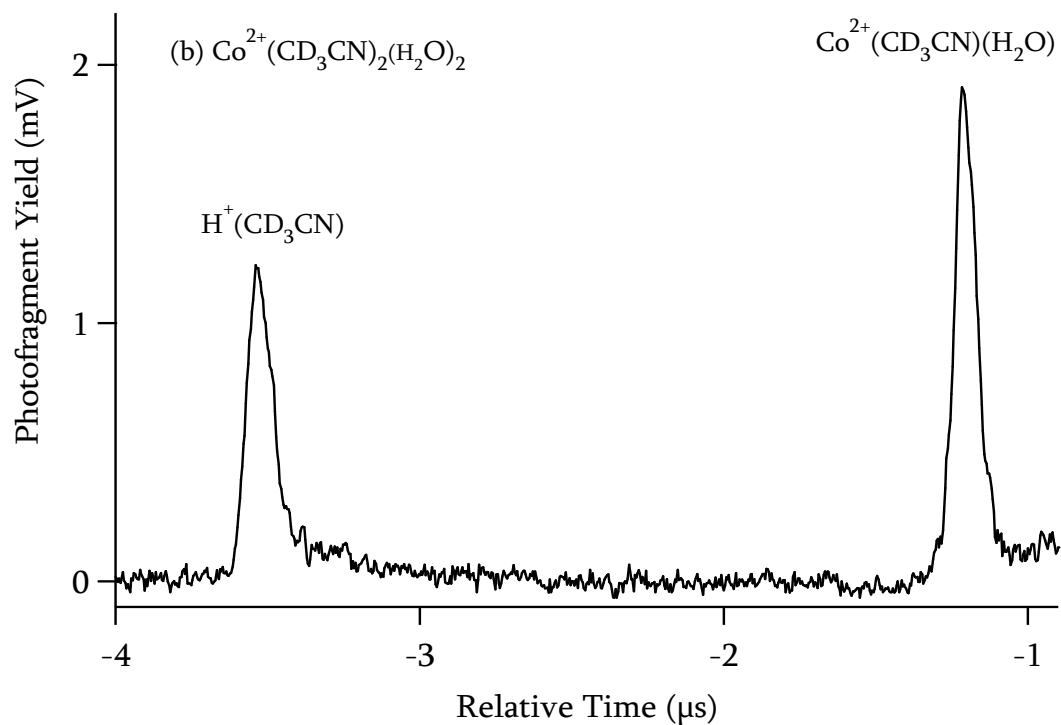
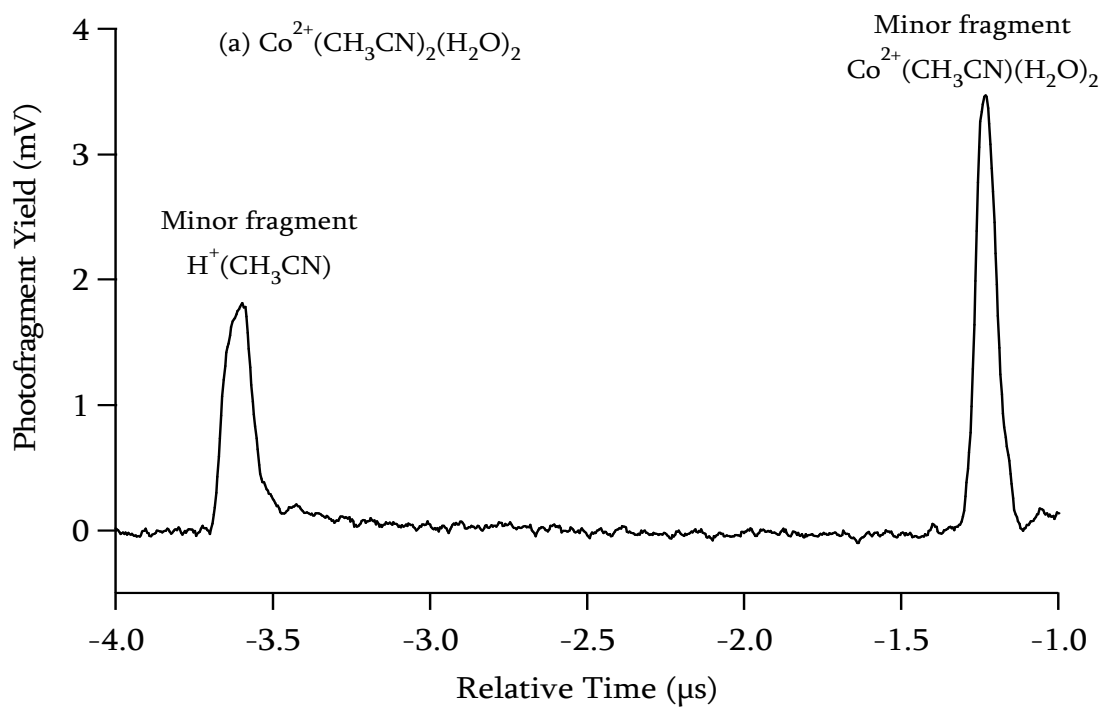
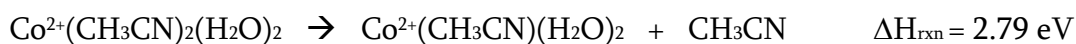
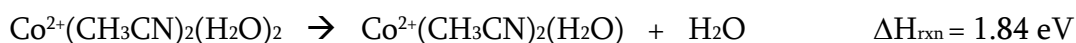


Figure 4.6: The minor fragmentation pathways, proton transfer and acetonitrile loss, are shown for (a) $\text{Co}^{2+}(\text{CH}_3\text{CN})_2(\text{H}_2\text{O})_2$ and (b) $\text{Co}^{2+}(\text{CD}_3\text{CN})_2(\text{H}_2\text{O})_2$. This was used to identify the proton donor to be water and not acetonitrile.

acetonitrile molecule. We were not able to study $M^{2+}(\text{CH}_3\text{CN})(\text{H}_2\text{O})_3$ due to the inability to produce a stable parent. In our previous studies of $\text{Ni}^{2+}(\text{H}_2\text{O})_4$ and $\text{Co}^{2+}(\text{H}_2\text{O})_4$ we found that proton transfer dominates.^{10,11}

When there is an equal number of the two solvents present in the mixed cluster, $\text{Co}^{2+}(\text{CH}_3\text{CN})_2(\text{H}_2\text{O})_2$, the preferred dissociation pathway is simple solvent water molecule loss. The calculations again predict that water loss is energetically favored:

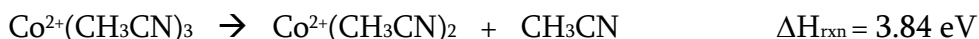


Experimentally, acetonitrile loss was observed but it is a significantly smaller dissociation channel. The other dissociation pathway was proton transfer. Energetically this is favorable since two singly charged fragments are produced. However, the activation barrier leading towards the fragments is quite high, and the transition state for proton transfer is tighter than that for solvent loss therefore this is not a very favorable dissociation channel. As we saw in the difference spectra, proton transfer and loss of acetonitrile channels have significantly lower yield than loss of water.

4.3.1.2 Three Coordinate Complexes

Producing the smaller clusters requires very different instrument conditions than for the four coordinate clusters. Mostly, the ion funnel DC gradient and pressure in the desolvating chamber have to be tuned. For example, the pressure in the chamber has to be higher (-500 mTorr), compared to -300 mTorr for larger clusters. Also, the ion funnel DC gradient has to be 30-40 V, rather than the -18-20 V typically used for four coordinate clusters.

When $\text{Co}^{2+}(\text{CH}_3\text{CN})_3$ dissociates, the only product observed was simple loss of solvent acetonitrile as shown in figure 4.7 (a). Unlike the four coordinate clusters, the second solvent molecule loss was not observed. The low photodissociation yield is likely due to the high binding energy of the solvent molecule:



This binding energy is 1.43 eV higher than for $\text{Co}^{2+}(\text{CH}_3\text{CN})_4$.

Photodissociation of the mixed three coordinate cluster, $\text{Co}^{2+}(\text{CH}_3\text{CN})_2(\text{H}_2\text{O})$, produces solvent loss and proton transfer, as shown in figure 4.8 (a). The major pathway is solvent water loss. Again, loss of acetonitrile is calculated to require more energy and is not observed:



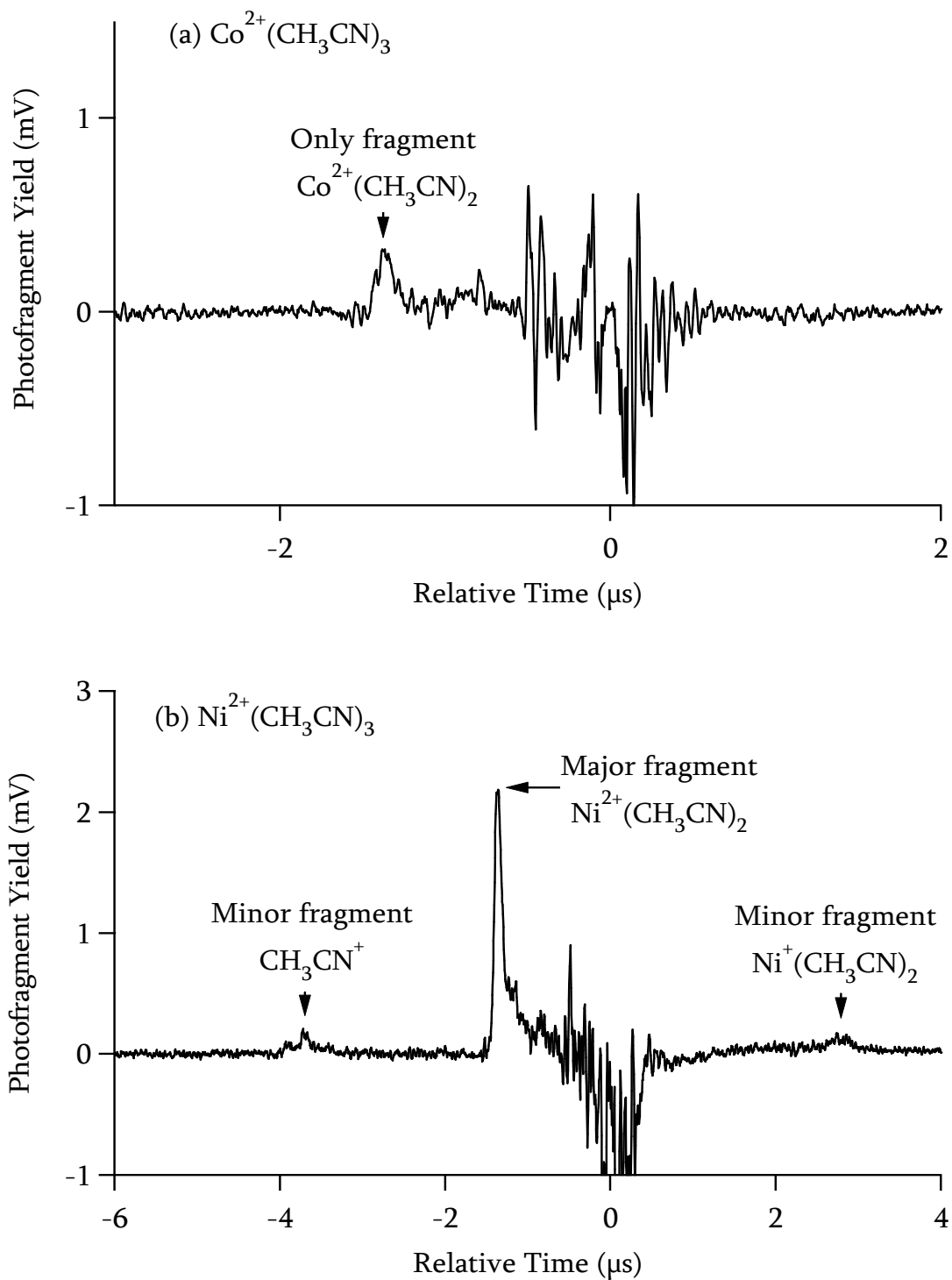


Figure 4.7: Difference spectra of three coordinate clusters (a) $\text{Co}^{2+}(\text{CH}_3\text{CN})_3$ and (b) $\text{Ni}^{2+}(\text{CH}_3\text{CN})_3$. The common fragmentation pathway is acetonitrile loss (major). The electron transfer channel is unique for Ni^{2+} cluster.

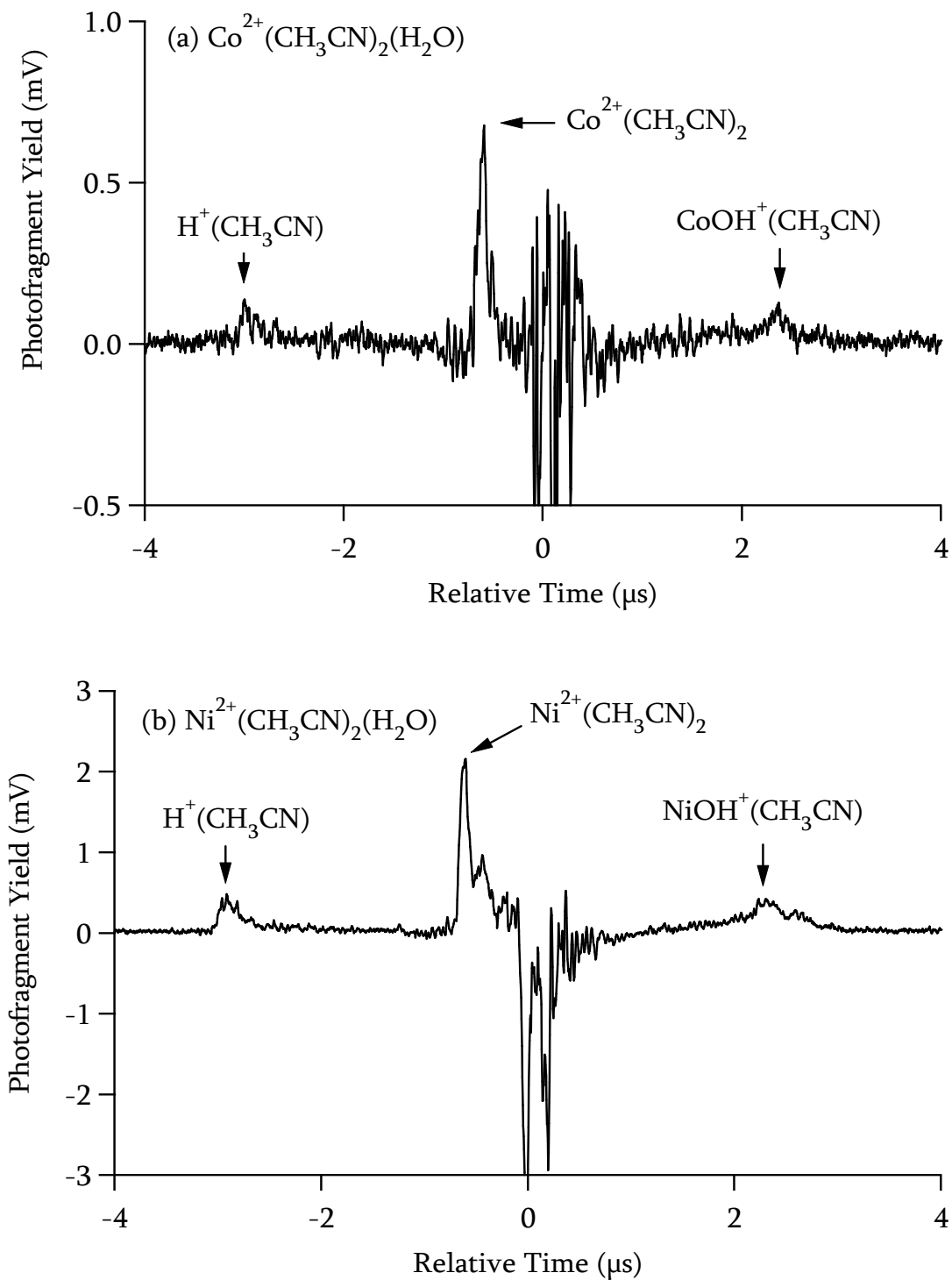
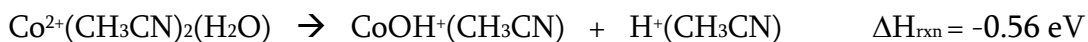


Figure 4.8: Difference spectra of (a) $\text{Co}^{2+}(\text{CH}_3\text{CN})_2(\text{H}_2\text{O})$ and (b) $\text{Ni}^{2+}(\text{CH}_3\text{CN})_2(\text{H}_2\text{O})$. The common fragmentation pathways are water loss (major) and proton transfer.

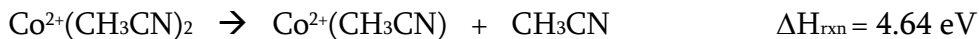
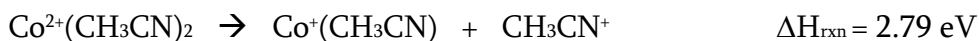
The second, minor path is proton transfer which results in producing protonated acetonitrile and the complementary metal hydroxide, $\text{CoOH}^+(\text{CH}_3\text{CN})$. This minor proton transfer pathway in three coordinate clusters results in similar low yield when compared to the four coordinate cluster proton transfer channels. The proton transfer pathway is an exothermic process, in contrast to the simple solvent losses.



However, it does not produce an abundance of fragments because this process has a calculated activation barrier of 1.10 eV, and the transition state is tighter than the simple solvent loss. In general, the photofragment yields for the three coordinate clusters are smaller than for the four coordinate clusters.

4.3.1.3 Two Coordinate Complexes

The last cluster we looked at was two coordinate $\text{Co}^{2+}(\text{CH}_3\text{CN})_2$. This shows a new dissociation pathway: electron transfer. The products are acetonitrile cation, CH_3CN^+ , and singly charged metal cation, $\text{Co}^+(\text{CH}_3\text{CN})$, as shown in figure 4.9 (a). Similar to the three coordinate clusters the photofragment yield is very low. Electron transfer is energetically favored over solvent loss:



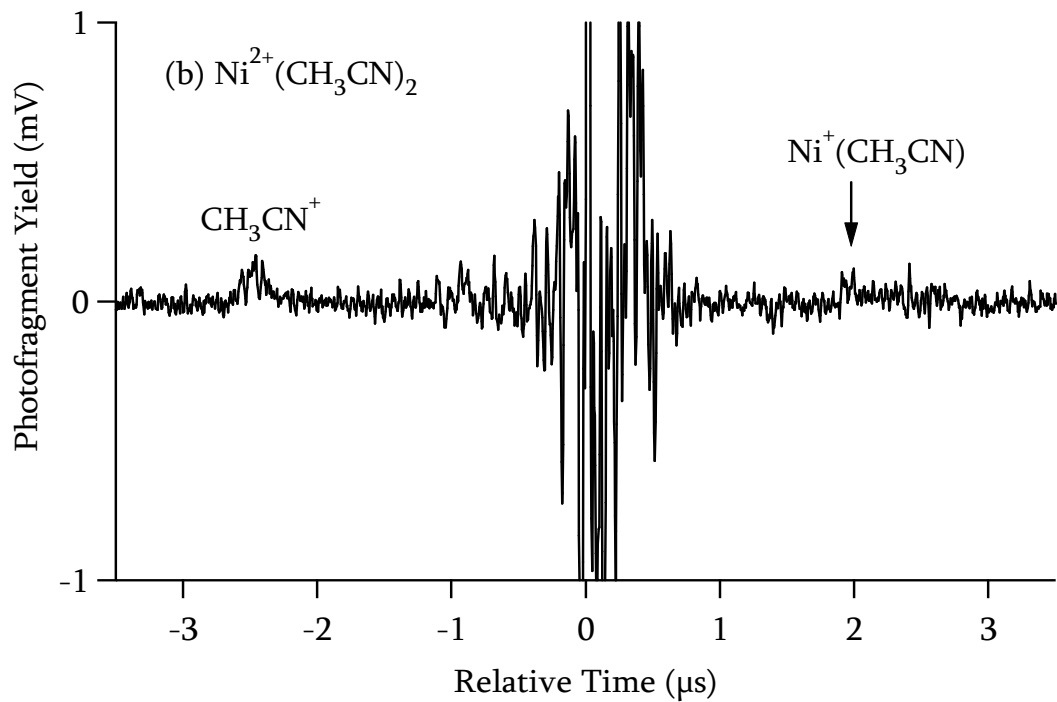
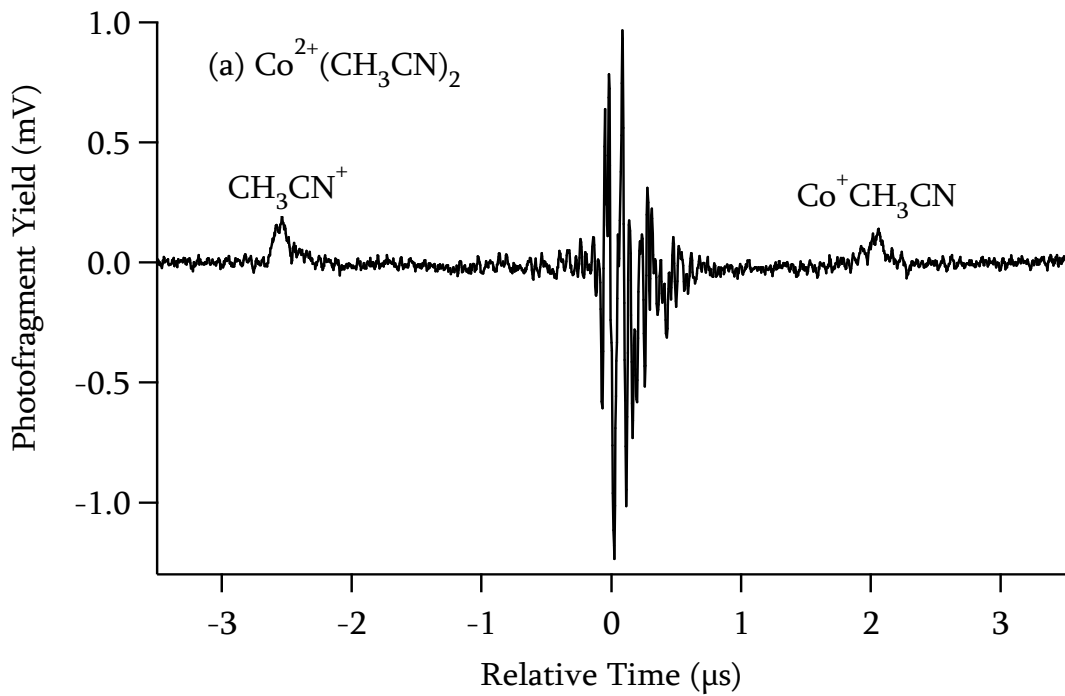


Figure 4.9: Difference spectra of (a) $\text{Co}^{2+}(\text{CH}_3\text{CN})_2$ and (b) $\text{Ni}^{2+}(\text{CH}_3\text{CN})_2$. Dissociation occurs via electron transfer.

The low photodissociation yield may be due to few molecules having sufficient energy to surmount the electron transfer activation barrier.

4.3.2 Photodissociation Dynamics of Ni²⁺ Complexes

The same clusters, M²⁺(CH₃CN)_n(H₂O)_m, were studied with Ni²⁺ as the metal. Both metals showed very similar photodissociation dynamics. The calculated thermodynamic data for observed dissociation pathways of M²⁺(CH₃CN)_n(H₂O)_m are shown for both metals in table 4.2. The energetics are similar for the two metals. However, the photofragment yields are quite different for Ni and Co complexes.

4.3.2.1 Photodissociation Yield of Four Coordinate Complexes

The absorption spectra of Ni (II) and Co (II) in solution are quite different, so we would expect that the absorption spectra of Ni²⁺(CH₃CN)_n(H₂O)_m and Co²⁺(CH₃CN)_n(H₂O)_m would also differ. The photodissociation yield reflects these differences in absorption cross section and in photodissociation quantum yield. Normalized photodissociation yields (Y) are given by

$$Y = F / (P \times L)$$

where F is the total area under all of the fragment peaks, P is the parent peak area and L is the laser power in Joules. Table 4.3 compares photodissociation yields for M²⁺(CH₃CN)_n, while yields for mixed clusters are in tables 4.4 and 4.5.

Reaction	Co Clusters (eV)	Ni Clusters (eV)
Four coordinate clusters		
$M^{2+}(CH_3CN)_4 \rightarrow M^{2+}(CH_3CN)_3 + CH_3CN$	2.41	2.13
$M^{2+}(CH_3CN)_4 \rightarrow M^{2+}(CH_3CN)_2 + 2 CH_3CN$	6.25	5.20
$M^{2+}(CH_3CN)_3(H_2O) \rightarrow M^{2+}(CH_3CN)_3 + H_2O$	1.76	1.69
$M^{2+}(CH_3CN)_3(H_2O) \rightarrow M^{2+}(CH_3CN)_2(H_2O) + CH_3CN$	2.61	2.62
$M^{2+}(CH_3CN)_2(H_2O)_2 \rightarrow M^{2+}(CH_3CN)_2(H_2O) + H_2O$	1.84	1.83
$M^{2+}(CH_3CN)_2(H_2O)_2 \rightarrow M^{2+}(CH_3CN)(H_2O)_2 + CH_3CN$	2.79	2.72
Three coordinate clusters		
$M^{2+}(CH_3CN)_3 \rightarrow M^{2+}(CH_3CN)_2 + CH_3CN$	3.84	3.06
$M^{2+}(CH_3CN)_2(H_2O) \rightarrow M^{2+}(CH_3CN)_2 + H_2O$	2.99	2.14
$M^{2+}(CH_3CN)_2(H_2O) \rightarrow M^{2+}(CH_3CN)(H_2O) + CH_3CN$	3.43	3.42
$M^{2+}(CH_3CN)_2(H_2O) \rightarrow MOH^+(CH_3CN) + H^+(CH_3CN)$	-0.56	-0.99
Two coordinate clusters		
$M^{2+}(CH_3CN)_2 \rightarrow M^+(CH_3CN) + CH_3CN^+$	2.79	1.81
$M^{2+}(CH_3CN)_2 \rightarrow M^{2+}(CH_3CN) + CH_3CN$	4.64	4.93
$M^{2+}(CH_3CN)(H_2O) \rightarrow MOH^+ + H^+(CH_3CN)$	-0.80	-1.19
$M^{2+}(CH_3CN)(H_2O) \rightarrow M^{2+}(CH_3CN) + H_2O$	4.20	3.64
$M^{2+}(CH_3CN)(H_2O) \rightarrow M^{2+}(H_2O) + CH_3CN$	4.50	5.86

Table 4.2: Energies for the dissociation reactions of $M^{2+}(CH_3CN)_n(H_2O)_m$ clusters.

Coordination number	Type of Cluster	Normalized Photodissociation Yield for Co ²⁺	Normalized Photodissociation Yield for Ni ²⁺
Four	M ²⁺ (CH ₃ CN) ₄	2.1	0.28
Three	M ²⁺ (CH ₃ CN) ₃	0.07	0.46
Two	M ²⁺ (CH ₃ CN) ₂	0.08	0.09

Table 4.3: Normalized photodissociation yields are compared for homogeneous clusters of both metals at 532 nm.

Type of Cluster	Normalized photodissociation yield for Cobalt cluster (λ_{\max})	Normalized photodissociation yield for Nickel cluster (λ_{\max})
M ²⁺ (CH ₃ CN) ₄	3.41 (595 nm)	0.28 (532 nm)
M ²⁺ (CH ₃ CN) ₃ (H ₂ O)	2.85 (605 nm)	0.74 (532 nm)
M ²⁺ (CH ₃ CN) ₂ (H ₂ O) ₂	3.09 (605-615 nm)	0.46 (605-615 nm)
M ²⁺ (CH ₃ CN) ₁ (H ₂ O) ₃	N/A	N/A
M ²⁺ (H ₂ O) ₄	(585 nm; shoulder at 518 nm)	(605 nm; shoulder at 512 nm)

Table 4.4 : Four coordinate clusters of M²⁺(CH₃CN)_n(H₂O)_m where M = Co and Ni, normalized photodissociation yield for simple solvent loss at the maximum absorption wavelength.

Type of Cluster	Normalized photodissociation yield for Cobalt cluster	Normalized photodissociation yield for Nickel cluster
$M^{2+}(\text{CH}_3\text{CN})_3$	0.07	0.46
$M^{2+}(\text{CH}_3\text{CN})_2(\text{H}_2\text{O})$	0.15	0.78

Table 4.5: Three coordinate clusters of Ni and Co, $M^{2+}(\text{CH}_3\text{CN})_n(\text{H}_2\text{O})_m$, normalized photodissociation yield at 532 nm

Figure 4.2 and table 4.3 show that $\text{Co}^{2+}(\text{CH}_3\text{CN})_4$ is more readily dissociated than the same nickel cluster by almost an order of magnitude. The calculated energy for CH_3CN loss from the nickel complex is 2.13 eV, which is 0.28 eV lower than for the cobalt complex. This suggests that the difference in photodissociation yield is not due to photodissociation quantum yield, rather is because the nickel four coordinate acetonitrile clusters do not absorb strongly for photon energies in the visible wavelengths (532–660 nm). It is clear that the cobalt four coordinate clusters dissociate more readily than nickel for all combinations of $M^{2+}(\text{CH}_3\text{CN})_n(\text{H}_2\text{O})_m$.

The major pathway for all four coordinate clusters is simple solvent loss. However, $\text{Ni}^{2+}(\text{CH}_3\text{CN})_2(\text{H}_2\text{O})_2$ fragments via two minor pathways: proton transfer and a small amount of loss of acetonitrile as shown in figure 4.10. The same dissociation channels were observed $\text{Co}^{2+}(\text{CH}_3\text{CN})_2(\text{H}_2\text{O})_2$. But, in the cobalt complex, acetonitrile loss was slightly favored over proton transfer pathway. The opposite is true for $\text{Ni}^{2+}(\text{CH}_3\text{CN})_2(\text{H}_2\text{O})_2$.

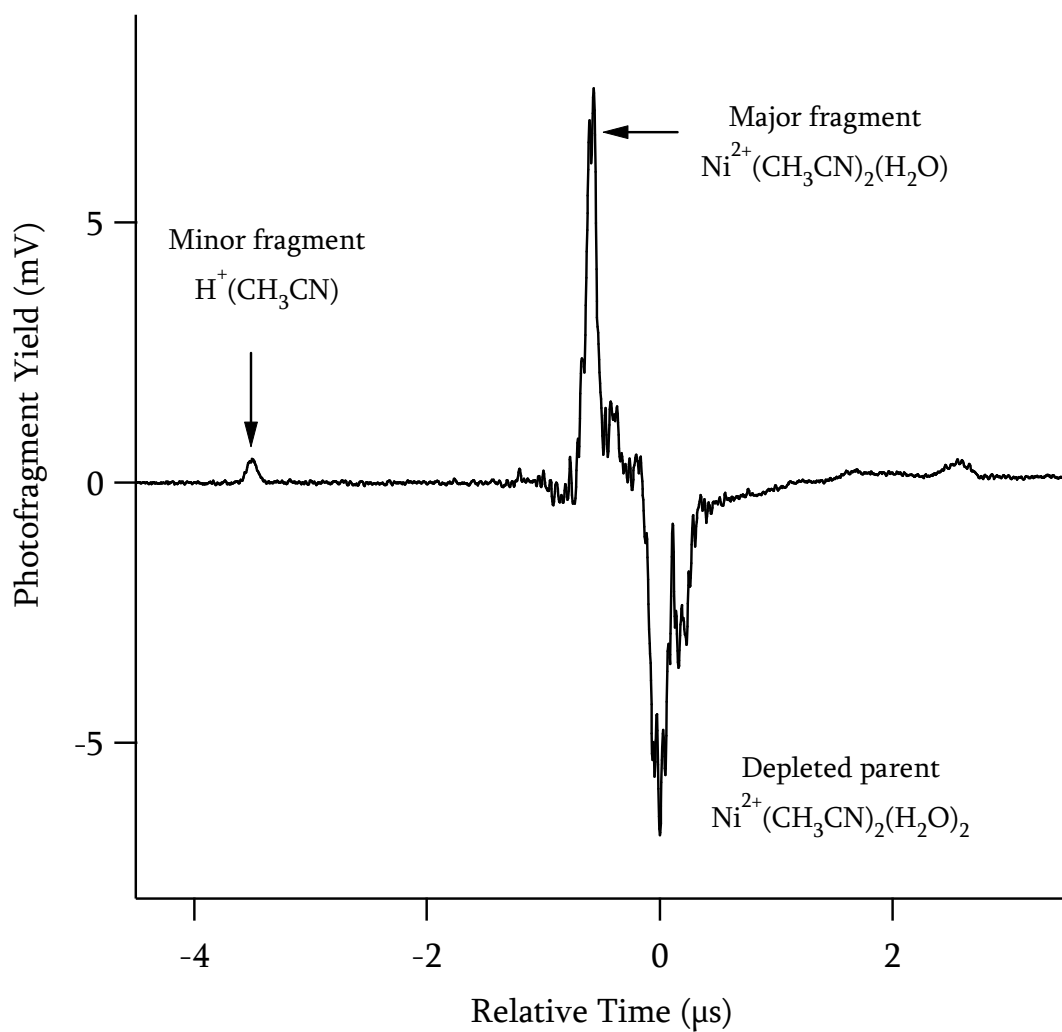
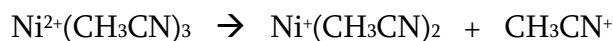


Figure 4.10: Difference spectrum for $\text{Ni}^{2+}(\text{CH}_3\text{CN})_2(\text{H}_2\text{O})_2$ shows three dissociation pathways: proton transfer and solvent (major: water, very minor: acetonitrile) loss.

4.3.2.2 Photodissociation Yield of Three Coordination Complexes

The photodissociation yield for three coordinate nickel complexes is similar to that of four coordinate complexes, with complexes containing more water generally showing higher yield. In contrast the photodissociation yield for three coordinate cobalt complexes is very low. This could be due to differences in absorption, but it is also likely that photodissociation quantum yield plays a role. Solvent binding energies in $\text{Co}^{2+}(\text{CH}_3\text{CN})_3$ and $\text{Co}^{2+}(\text{CH}_3\text{CN})_2(\text{H}_2\text{O})$ are calculated to be above the 2.33 eV photon energy, and are ~ 0.8 eV higher than those of the corresponding nickel complexes. As with the four coordinate mixed clusters, $\text{Ni}^{2+}(\text{CH}_3\text{CN})_2(\text{H}_2\text{O})$ shows higher branching for proton transfer than the cobalt complex (figure 4.8).

The most interesting observation compared to $\text{Co}^{2+}(\text{CH}_3\text{CN})_3$ is that electron transfer was a minor dissociation pathway that was observed for $\text{Ni}^{2+}(\text{CH}_3\text{CN})_3$.



This may show slight broadening in the time-of-flight profile (figure 4.7) due to kinetic energy release, but it is hard to quantify, as the fragment peak is broadened due to dissociation of ^{58}Ni and ^{60}Ni complexes.

4.3.2.3 Photodissociation Yield of Two Coordinate Complexes

The photodissociation yields of $M^{2+}(\text{CH}_3\text{CN})_2$ were similar for the two metals. Electron transfer is the only channel observed, and this is likely to have a large barrier, which will reduce the photodissociation quantum yield.

4.3.3 Wavelength Dependence

The wavelength at which maximum photodissociation is observed (λ_{max}) depends on the type of solvent present. The $\text{Co}^{2+}(\text{CH}_3\text{CN})_4$ complex shows maximum dissociation near 595 nm and as the number of water molecules increases the absorption peak shifted toward 605-615 nm. Previous studies in our lab have shown that the $\text{Co}^{2+}(\text{H}_2\text{O})_4$ maximum absorption is around 585 nm with a shoulder extending to 518 nm.¹¹ Generally, acetonitrile addition shifts the absorption to a slightly lower energy compared to the homogeneous water complex.

Four coordinate clusters of nickel shows different trend in the wavelength dependence of the dissociation. As the number of acetonitrile molecules increases in the four coordinate clusters the maximum absorption peak moved towards higher energy, 532 nm, compared to homogeneous water clusters which peak near 605 nm.¹⁰ These molecules are considerably larger hence the absorption peaks are also broader.

4.4 Discussion

The microsolvation of Co^{2+} and Ni^{2+} by acetonitrile and water study was specifically done to understand the interaction of solvents with the metal center and competition between two different solvent molecules such as protic water and aprotic acetonitrile. Since prior work in our lab focused on protic solvents, this will shed more information on aprotic solvents. Acetonitrile is the better solvent towards M^{2+} due to its higher polarizability and dipole moment. The smallest cluster previously made in our lab is $\text{M}^{2+}(\text{H}_2\text{O})_4$, but with acetonitrile we are able to make smaller clusters such as $\text{M}^{2+}(\text{CH}_3\text{CN})_2$. This is due to acetonitrile being a better solvent and minimizing proton transfer dissociation.

4.4.1 Geometry of the Metal Dication Clusters

Our earlier studies conclude that the four coordinate clusters $\text{M}^{2+}(\text{H}_2\text{O})_4$ for $\text{M} = \text{Co}$ and Ni are tetrahedral and that these absorptions are red shifted from the solution data of Swaddle and Fabes.²⁰ Tetrahedral complexes absorb more strongly than square planar due to lack of center of inversion in the geometry. Our mixed four coordinate clusters, $\text{M}^{2+}(\text{CH}_3\text{CN})_n(\text{H}_2\text{O})_m$, also showed the maximum absorption in the bulk range of the tetrahedral absorption peak. This again suggests that these four coordinate complexes are approximately tetrahedral. This is supported by our

calculations which predict tetrahedral geometries for $\text{Co}^{2+}(\text{CH}_3\text{CN})_4$ and $\text{Ni}^{2+}(\text{CH}_3\text{CN})_4$.

4.4.2 Homogeneous Acetonitrile Clusters

Leary and co-workers have conducted studies to compare the CID of divalent cations, $\text{M}^{2+}(\text{CH}_3\text{CN})$ and $\text{M}^{2+}(\text{CH}_3\text{CN})_2$, of alkaline earth metals such as calcium and transition metals such as Sr, Mn and Co.^{14,15} Shvartsburg and co-workers have specifically looked at the charge transfer and fragmentation pathways for $\text{M}^{2+}(\text{CH}_3\text{CN})_n$ metals such as Be, Mg, Ca, Sr, Ba, Zn, Cd, Mn, Fe, Co, Ni and Cu.¹³ The CID studies show that the major dissociation pathways for smaller clusters with aprotic solvents are proton transfer, electron transfer and heterolytic bond cleavage as shown in figure 4.11. These CID studies were only done for the homogeneous acetonitrile clusters.

Our photofragmentation studies of $\text{M}^{2+}(\text{CH}_3\text{CN})_n$, show similar dissociation pathways. However, heterolytic bond cleavage was not observed. This may have been due to our inability to create the $\text{M}^{2+}(\text{CH}_3\text{CN})$ parent. The larger clusters showed simple solvent loss. The smallest cluster we observe, $\text{M}^{2+}(\text{CH}_3\text{CN})_2$, showed proton transfer and electron transfer in CID studies. With the quantitative photon energy provided in our photodissociation dynamics studies we only observe electron transfer. The electron and proton transfer products only differ by one mass unit, so there is the possibility that both pathways exist and the peaks overlap. To confirm

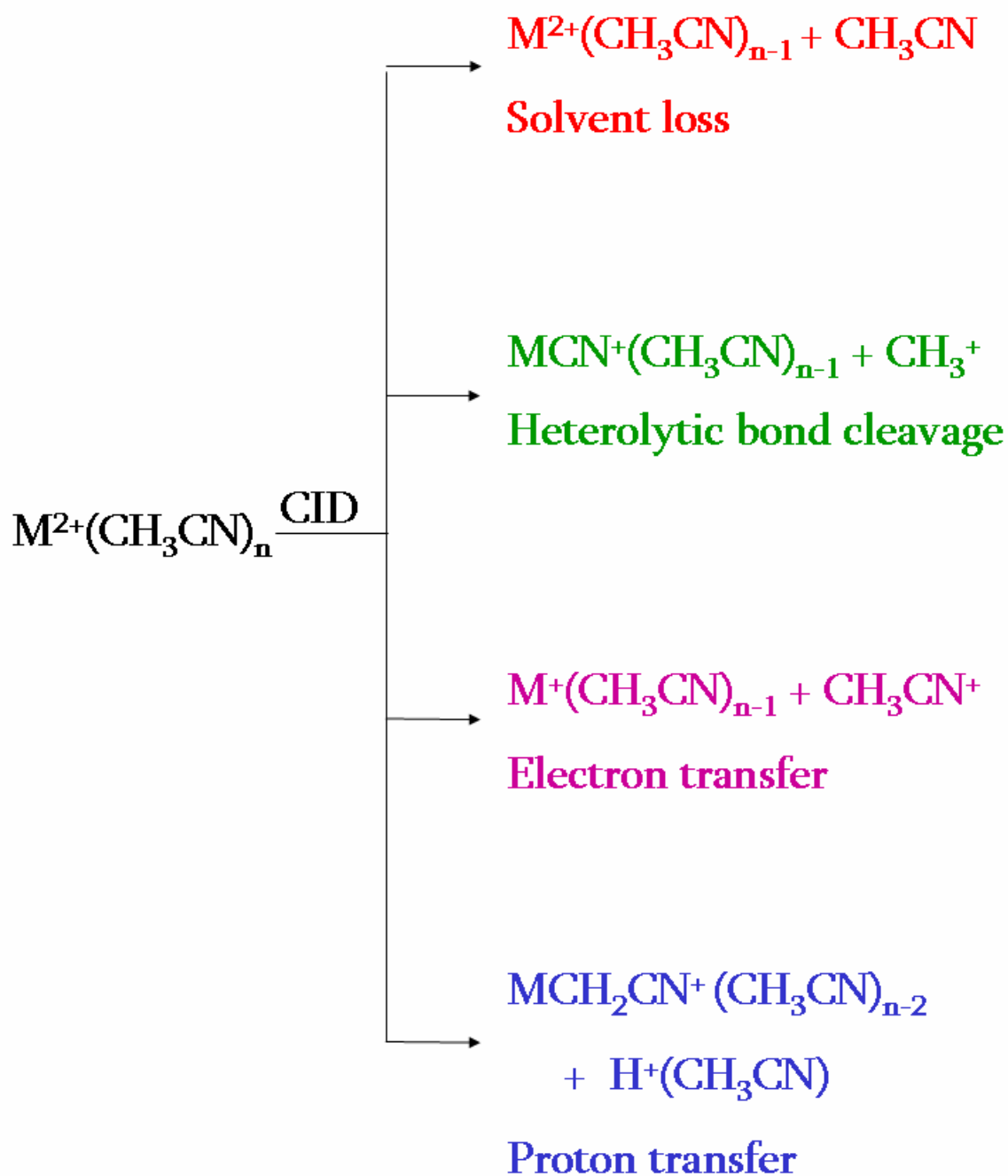


Figure 4.11: Shvartsburg and coworkers have above fragmentation pathways for doubly charged metals such as Be, Mg, Ca, Sr, Ba, Zn, Cd, Mn, Fe, Co, Ni and Cu with acetonitrile.¹³ Collision energies range from 40 – 160 eV.

that the only dissociation pathway we monitored was due to electron transfer, the study was extended using deuterated acetonitrile, CD_3CN . Deuteron transfer will result in fragments that are two mass units apart. However, we only see one fragment pathway: electron transfer. The difference between the CID and photolysis results could be due to more energy being available in the CID studies and a proton transfer barrier that lies above our photon energy.

4.4.3 Photodissociation Dynamics of $\text{M}^{2+}(\text{CH}_3\text{CN})_n(\text{H}_2\text{O})_m$ Clusters

4.4.3.1 Simple Solvent Loss Pathway

Solvent loss is the dominant path of dissociation for metal-solvent clusters with coordination number $n > 2$. Observation of simple solvent loss is similar to the $\text{M}^{2+}(\text{H}_2\text{O})_n$ and $\text{M}^{2+}(\text{CH}_3\text{OH})_n$ studies done previously in our lab, where solvent loss dominates for $n > 4$.¹⁰⁻¹² Also, if there is a combination of solvents such as water and acetonitrile, the more weakly bound solvent is more likely to cleave the electrostatic bond with the metal dication, leading to preferential loss of water. The smallest cluster we could produce with water and methanol had $n=4$. Acetonitrile stabilizes Co^{2+} and Ni^{2+} better than water, so we were able to produce mixed three-coordinate clusters which mostly dissociate by solvent water loss.

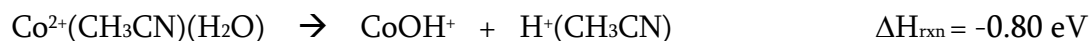
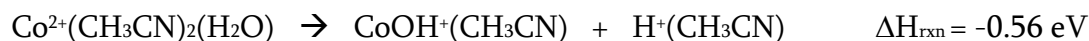
4.4.3.2 Electron Transfer Pathway

The novel important dissociation pathway that was observed is electron transfer. This is only observed for the two and three coordinate clusters, $M^{2+}(CH_3CN)_2$ for both metals. Protic solvents like water favor proton transfer, and this is the major dissociation pathway for small clusters. For aprotic solvents, in the absence of proton transfer, electron transfer is observed. Also, doubly charged clusters fragmenting to two singly charged species typically provide information on kinetic energy release (KER) in the form of peak broadening. This was obvious in our earlier studies of $M^{2+}(H_2O)_4$ and $M^{2+}(CH_3OH)_4$. However, there is much less KER for the acetonitrile complexes (see figure 4.9). This could be due to electron transfer taking place when the two fragments are fairly far apart, minimizing Coulomb repulsion.

4.4.3.3 Proton Transfer Pathway

The other interesting dissociation pathway was proton transfer. This was only observed for mixed clusters, and its importance differed between the metals, Ni and Co. Proton transfer was observed when there was at least one water molecule present in the metal cluster, so homogeneous acetonitrile clusters did not show this channel. Also, the $M^{2+}(CH_3CN)_3(H_2O)$ cluster did not follow the proton transfer pathway, presumably because loss of water is much more favorable.

According to the calculations shown below the proton transfer pathways are exothermic.



Previous work in our lab on $\text{M}^{2+}(\text{H}_2\text{O})_4$ shows that during the dissociation via proton transfer, the transition state adopts a salt-bridge arrangement $\text{M}^{2+}\text{-OH}^-\text{-H}_3\text{O}^+$.²¹ This lowers the Coulomb barrier to fragments. $\text{Co}^{2+}(\text{H}_2\text{O})_4$ lies 0.22 eV above the proton transfer products $\text{H}_3\text{O}^+ + \text{CoOH}^+(\text{H}_2\text{O})_2$. However, $\text{Co}^{2+}(\text{H}_2\text{O})_4$ is kinetically stable because proton transfer has a 1.5 eV barrier. If we consider the thermodynamics of $\text{Co}^{2+}(\text{CH}_3\text{CN})_2(\text{H}_2\text{O})$, the calculations show that proton transfer is exothermic by 0.56 eV in the absence of a photon. However, the $\text{Co}^{2+}(\text{CH}_3\text{CN})_2\text{-H}_2\text{O}$ attractive potential and the $\text{CoOH}^+(\text{CH}_3\text{CN})\text{-(H}^+\text{CH}_3\text{CN)}$ repulsive potentials are separated by a significant barrier, thus allowing us to observe thermodynamically unstable $\text{Co}^{2+}(\text{CH}_3\text{CN})_2(\text{H}_2\text{O})$. The transition state for proton transfer from $\text{Co}^{2+}(\text{CH}_3\text{CN})_2(\text{H}_2\text{O})$ is also calculated to have a salt-bridge structure $(\text{CH}_3\text{CN})\text{Co}^{2+}\text{-OH}^-\text{-H}^+(\text{NCCH}_3)$. We did not make sufficient amounts of $\text{Co}^{2+}(\text{CH}_3\text{CN})(\text{H}_2\text{O})_2$ to study. This is likely because the barrier to proton transfer for this molecule is so low that it dissociates in our source. Mixed water-acetonitrile clusters show proton transfer, and this channel becomes increasingly important as more acetonitriles are replaced by water. This is due to two effects. Water is less able to stabilize the 2+ charge than acetonitrile and studies done with deuterated acetonitrile confirm that the proton donor is water.

Proton transfer fragments showed no significant peak broadening, indicating that the kinetic energy release is small. This suggests that the transition state for proton transfer occurs at large $\text{MOH}^+\text{-H}^+(\text{CH}_3\text{CN})$ distances, and that acetonitrile vibrations provide an efficient sink for excess energy.

4.4.4 Influence of Metal

Nickel dications solvated by acetonitrile and water generally show the same dissociation pathways for similar clusters as cobalt. One exception is that proton transfer is more favored in nickel complexes such $\text{M}^{2+}(\text{CH}_3\text{CN})_2(\text{H}_2\text{O})$. Nickel's second ionization energy is 18.17 eV, which is slightly higher than that of cobalt (17.08 eV). This favors proton transfer to create two singly charged ions rather than the loss of solvent.

4.5 References

- (1) Lever, A. B. P. *Inorganic Electronic Spectroscopy (Second Edition)*; Elsevier: Amsterdam, 1984.
- (2) Shvartsburg, A. A.; Siu, K. W. M. *J. Am. Chem. Soc.* **2001**, *123*, 10071.
- (3) Stace, A. J. *J. Phys. Chem. A* **2002**, *106*, 7993.
- (4) Peschke, M.; Blades, A. T.; Kebarle, P. *J. Am. Chem. Soc.* **2000**, *122*, 1492.
- (5) Kebarle, P. *Int. J. Mass Spectrom.* **2000**, *200*, 313.
- (6) Lisy, J. M. *Int. Rev. Phys. Chem.* **1997**, *16*, 267.
- (7) Keese, R. G.; A. W. Castleman, J. *J. Phys. Chem. Ref. Data* **1986**, *15*, 1011.
- (8) Stace, A. J.; Walker, N. R.; Firth, S. *J. Am. Chem. Soc.* **1997**, *119*, 10239.
- (9) Yamashita, M.; Fenn, J. B. *J. Phys. Chem.* **1984**, *88*, 4451.
- (10) Thompson, C. J.; Husband, J.; Aguirre, F.; Metz, R. B. *J. Phys. Chem. A* **2000**, *104*, 8155.
- (11) Faherty, K. P.; Thompson, C. J.; Aguirre, F.; Michne, J.; Metz, R. B. *J. Phys. Chem. A* **2001**, *105*, 10054.
- (12) Thompson, C. J.; Faherty, K. P.; Stringer, K. L.; Metz, R. B. *Phys. Chem. Chem. Phys.* **2005**, *7*, 814.
- (13) Shvartsburg, A. A.; Wilkes, J. G.; Lay, J. O.; Siu, K. W. M. *Chem. Phys. Lett.* **2001**, *350*, 216.
- (14) Kohler, M.; Leary, J. A. *Int. J. Mass Spectrom. Ion Proc.* **1997**, *162*, 17.
- (15) Kohler, M.; Leary, J. A. *J. Am. Soc. Mass Spectrom.* **1997**, *8*, 1124.

- (16) Metz, R. B. *Int. J. Mass Spectrom.* **2004**, *235*, 131.
- (17) Chowdhury, S. K.; Katta, V.; Chait, B. T. *J. Rapid Commun. Mass Spectrom.* **1990**, *4*, 81.
- (18) Him, T.; Tolmachev, A. V.; Harkewicz, R.; Prior, D. C.; Anderson, G.; Udseth, H. R.; Smith, R. D.; Bailey, T. H.; Rakov, S.; Futrell, J. H. *Anal. Chem.* **2000**, *72*, 2247.
- (19) Frisch, M. J.; Trucks, G. W.; Schlegel, H. B.; Scuseria, G. E.; Robb, M. A.; Cheeseman, J. R.; Zakrzewski, V. G.; Montgomery, J. A.; Stratmann, R. E.; Burant, J. C.; Dapprich, S.; Millam, J. M.; Daniels, A. D.; Kudin, K. N.; Strain, M. C.; Farkas, O.; Tomasi, J.; Barone, V.; Cossi, M.; Cammi, R.; Mennucci, B.; Pomelli, C.; Adamo, C.; Clifford, S.; Ochterski, J.; Petersson, G. A.; Ayala, P. Y.; Cui, Q.; Morokuma, K.; Malick, D. K.; Rabuck, A. D.; Raghavachari, K.; Foresman, J. B.; Cioslowski, J.; Ortiz, J. V.; Stefanov, B. B.; Liu, G.; Liashenko, A.; Piskorz, P.; Komaromi, I.; Gomperts, R.; Martin, R. L.; Fox, D. J.; Keith, T.; Al-Laham, M. A.; Peng, C. Y.; Nanayakkara, A.; Gonzalez, C.; Challacombe, M.; Gill, P. M. W.; Johnson, B. G.; Chen, W.; Wong, M. W.; Andres, J. L.; Head-Gordon, M.; Replogle, E. S.; Pople, J. A. *Gaussian 98*; Revision A.3 ed.; Gaussian, Inc.: Pittsburgh PA, 1998.
- (20) Swaddle, T. W.; Fabes, L. *Can. J. Chem.* **1980**, *58*, 1418.
- (21) Beyer, M. K.; Metz, R. B. *J. Phys. Chem. A* **2003**, *107*, 1760.

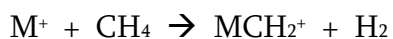
CHAPTER 5

IONIZATION ENERGIES OF PtC_nH_m AND A POTENTIAL ENERGY SURFACE FOR THE $Pt + CH_4$ REACTION

5.1 Introduction

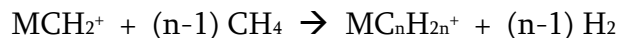
Although the US has extensive natural gas reserves, gasoline production from natural gas has been hampered by the lack of appropriate catalysts. If an efficient catalyst to convert methane to larger hydrocarbons were developed, it then could be matched with systems like zeolites to produce highly branched hydrocarbons.¹ This process will produce high octane petroleum without consuming scarce crude oil. However, the main problem with activating methane is that it is the least reactive hydrocarbon, due to the strong C-H bonds (104 kcal/mol), which is higher than the C-H bond strength in other primary or secondary alkanes (90-98 kcal/mol).

This economic imperative has led to extensive research on methane activation using a variety of transition metal catalysts. One particularly interesting finding is that some gas phase transition metal cations, M^+ , do undergo reactions with methane. Beauchamp and co-workers using Fourier-transform ion cyclotron resonance studies have shown that most of the third row transition metals spontaneously dehydrogenate methane at room temperature.²



However, the dehydrogenation reaction is endothermic for the first and second row metals.³⁻⁵

In some cases, the metal carbenes can further react via Fischer-Tropsch methylene coupling to create larger hydrocarbons.²



For example, tungsten cation reacts sequentially with methane to make $WC_8H_{16}^+$. The initial four methane molecule reactions are fast near the collision rate and the subsequent four methane molecule reactions are much slower. The late transition metals are less reactive. At thermal energies, Pt^+ reacts readily with methane to produce $PtCH_2^+$, which is unreactive towards methane.^{2,5-7}

Platinum is widely used as an industrial catalyst. For example, platinum-based catalysts are used for dehydrogenation, isomerization and aromatization reactions in the petroleum industry.^{8,9} As a result, the consecutive reactions of Pt^+ with methane have received particular attention, as the simplest model of C-H bond activation.⁷ It is also used to test the reliability of electronic structure calculations which are challenging as due to relativistic effects, unpaired electrons and low-lying excited states.^{6,10}

In studying models for C-H bond activation, one would like to study a system that is as similar as possible to heterogeneous catalysts that industry uses. An interesting question is to what extent charge influences the reactivity. The long range M^+-CH_4 ion-induced dipole attraction tends to reduce reaction barriers, compared to

the corresponding neutral system. As a result, neutral metal atoms are much less reactive with methane and larger hydrocarbons than the cations.¹¹ At thermal energies, no neutral metal dehydrogenates methane.¹² However, platinum is consumed in collisions with methane.¹²⁻¹⁴ Studies show that this as a termolecular reaction: platinum inserts into a C-H bond, and the resulting H-Pt-CH₃ complex is stabilized by collisions with methane or helium buffer gas. Although predicted by computational studies, H-Pt-CH₃ has not been experimentally observed. While reactions of cations can be readily monitored by mass spectrometry, neutral reactions are hard to observe due to the lack of charge. Thus, the reaction energetics, rates and products have not been studied as much. The bond strength and relative energies of PtCH₂ and H-Pt-CH₃ have not been measured.

In our lab, we have looked at the intermediates and products of reactions of metal cations with small alkanes for first row transition metals such as Fe, Co and Ni, and third row metals Ta, Pt and Au.¹⁵⁻¹⁷ This chapter discusses our production of PtCH₂ and H-Pt-CH₃ by reaction of laser ablated platinum atoms with methane and subsequent measurement of their photoionization efficiencies (PIE). Ionization energies are derived from the PIEs. Ion beam studies have provided a wealth of information on bond dissociation energies for cations.⁵ Combining these bond energies with ionization energies for the corresponding neutrals allows us to determine bond energies for the neutral and to produce a potential energy diagram for neutral platinum reacting with methane. These results will then be used to

evaluate the reliability of computational approaches to the study of platinum activation of hydrocarbons which ultimately provide insights to theoretical models on late transition metal catalysts.

5.2 Experimental

Our study was carried out at the Chemical Dynamics Beamline at the Advanced Light Source (ALS) at Lawrence Berkeley National Laboratory. The beamline provides vacuum ultraviolet (VUV) light with photon energies of 8-16 eV at a repetition rate of 500 MHz. The linewidth is determined by the slit width on a 3 m monochromator. It was 20-50 meV in these studies. The instrumentation consisted of a laser ablation source coupled to a reflectron time-of-flight mass spectrometer. The ablation source was previously described in chapter 2 and other literature.¹⁸⁻²⁰ A schematic of the apparatus is shown in figure 5.1. A platinum tube (99.95% pure, Goodfellow) was used to produce Pt neutral atoms that then reacted with methane gas from a pulsed piezoelectric valve at 20 psi stagnation pressure. The ablation laser is a Nd:YAG at 532 nm with a repetition rate of 50 Hz. The laser can produce up to 8 mJ/pulse. High laser power favors production of PtC, while production of PtCH₂ and H-Pt-CH₃ is optimum at 3 mJ/pulse. The PtC_nH_m produced are cooled in the supersonic expansion and then transmitted to the next region through a skimmer. These neutral molecules are irradiated by the VUV light. Prior to the skimmer, a set

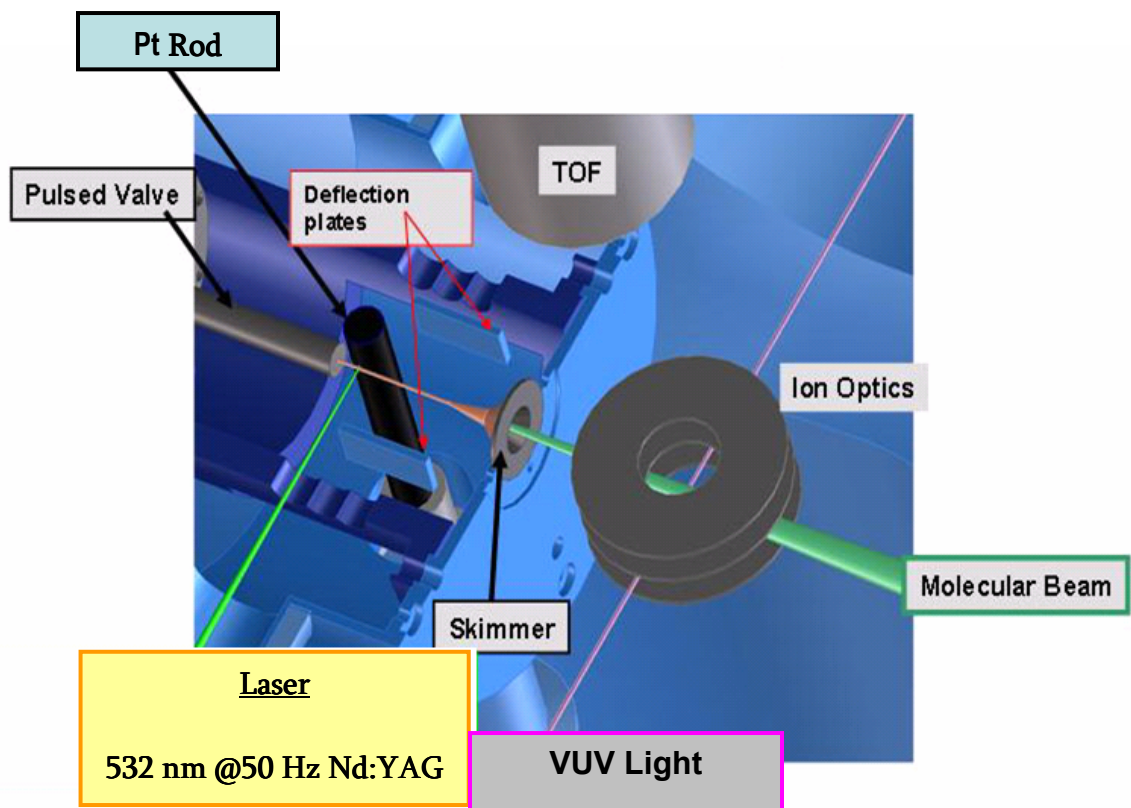
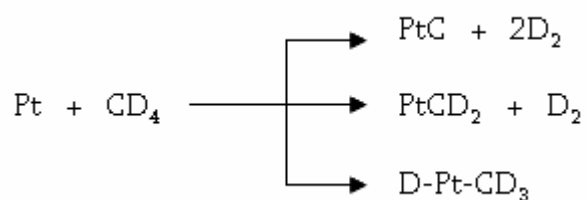


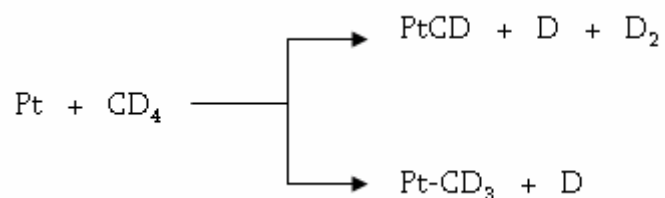
Figure 5.1: The ablation reflectron time-of-flight instrument used at the ALS is shown above. The VUV light irradiates the molecular beam at the center of the ion optics as shown (courtesy of Dr. Musa Ahmed, Lawrence Berkeley National Lab).

of deflector plates help to divert unwanted ions produced by ablation from the neutral beam. A pulsed voltage extracts neutrals that are ionized by the VUV light into a time-of-flight reflectron mass spectrometer. Another set of deflector plates located in the flight tube is used to maximize the signal. Ions travel to the detector where they are collected on a dual micro channel plate detector and characterized according to their arrival times. The time-of-flight spectra of the ions are collected with a multichannel scaler card (FAST Comtec 7886).

The use of a reflectron to increase the mass resolution is very important since Pt has four major isotopes: ^{194}Pt (33 %), ^{195}Pt (34 %), ^{196}Pt (25 %), and ^{198}Pt (7 %). To identify the products and avoid isobaric interferences we used deuterated methane for initial studies. Platinum-195 is the only odd mass isotope. So, in reactions with CD_4 , odd mass products must contain ^{195}Pt . These initial studies established the following reactions



but not the following reactions



So, subsequent experiments were done with CH₄, and the ¹⁹⁵Pt containing peak was typically monitored, as it is uniquely present in all odd mass peaks.

Mass spectra are obtained as a function of VUV photon energy, typically integrating over 5000 laser shots at each energy. Photoionization efficiency curves (PIE) are measured by integrating the area under the photo-ion of interest and normalizing to ALS current and VUV flux as measured by a Si photodiode. A survey scan is initially done over a range of energies to identify the products and estimate the onset region for each of the products. Finer scans, with smaller VUV linewidth, were then done near the onset. The fine scans were then used to find the ionization energy.

5.3 Results

Reaction of laser-ablated platinum atoms with methane was monitored by VUV ionization of the products. As noted above, the large number of platinum isotopes makes it difficult to identify the products of reaction with CH₄. Therefore we first used CD₄, and the resulting mass spectrum at 11 eV photon energy is shown in figure 5.2. It is clear that we are only making PtC, PtCD₂ and PtCD₄. No PtCD and PtCD₃ are observed. Small amounts of PtC₂D_n are also produced. Using ethane as a reaction partner leads to much higher yields of PtC₂H_n and of PtH₂ and studies of these species will be discussed elsewhere. Photoionization studies of PtC have

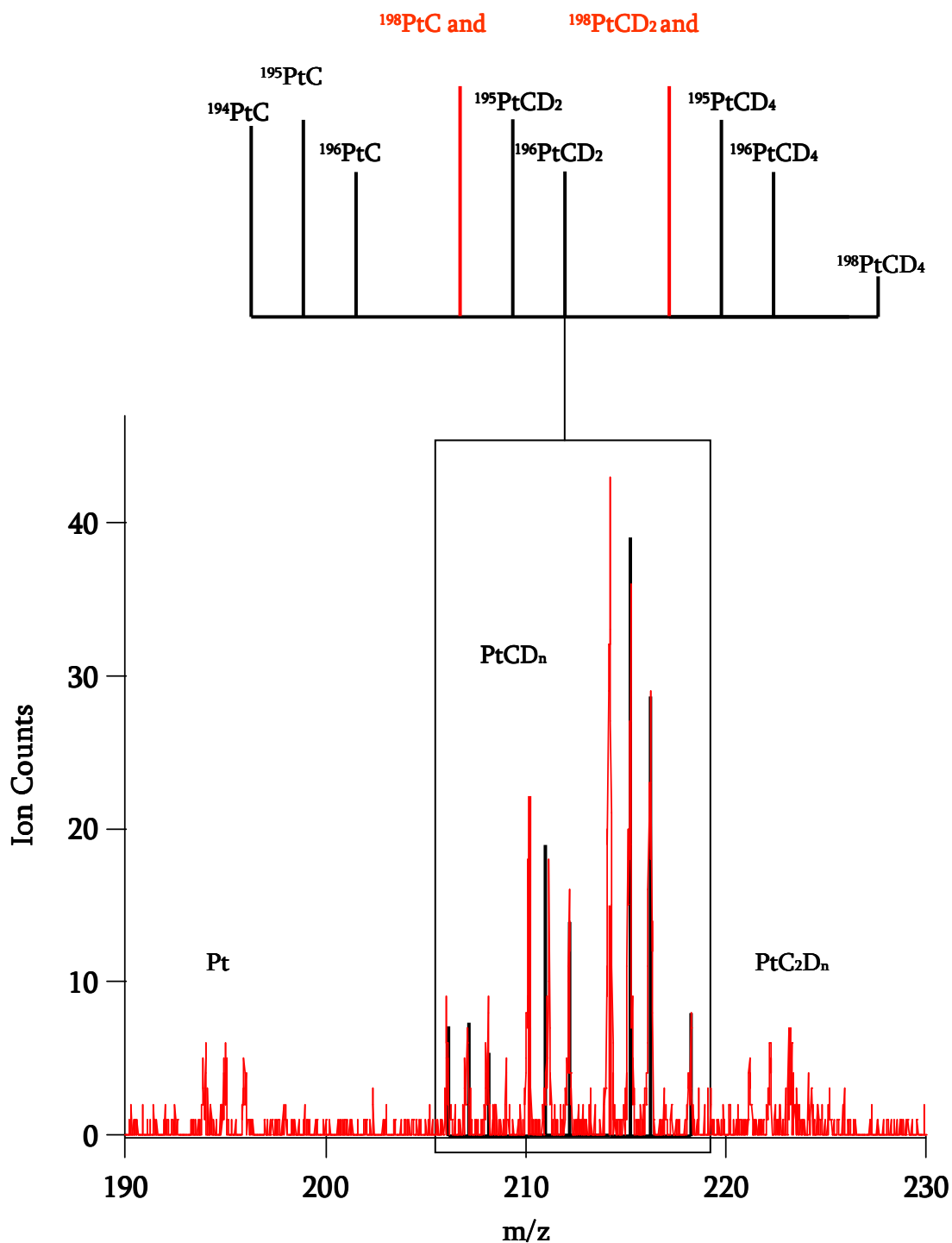


Figure 5.2: The mass spectrum of the ionized products from the reaction of laser-ablated platinum with CD_4 at 11 eV. The enlarged portion shows the assignment of the PtCD_n peaks.

already been published.²⁰ A complementary mass spectrum taken at 11 eV for the reaction of CH₄ with platinum is shown in figure 5.3.

A survey scan was run over a range of 8-10.5 eV to estimate the onset regions for the products of the reaction of platinum with methane. Fine scans with higher energy resolution and smaller step size onset were run near the ionization onset to find the ionization energy. Figure 5.4 shows the PIE of PtCH₂ near the ionization onset. It is important to find a peak that is not contaminated by isobaric interferences, so the onset is only due to the desired molecules. This data is obtained by monitoring only $m/z = 209$, which corresponds to ¹⁹⁵PtCH₂. This avoids interferences due to PtC and PtCH₄. The onset for PtCH₂ is at 8.78±0.05 eV. The other onset found from this study is due to the insertion intermediate, H-Pt-CH₃. The ionization energy is 8.89±0.05 eV, as shown in figure 5.5.

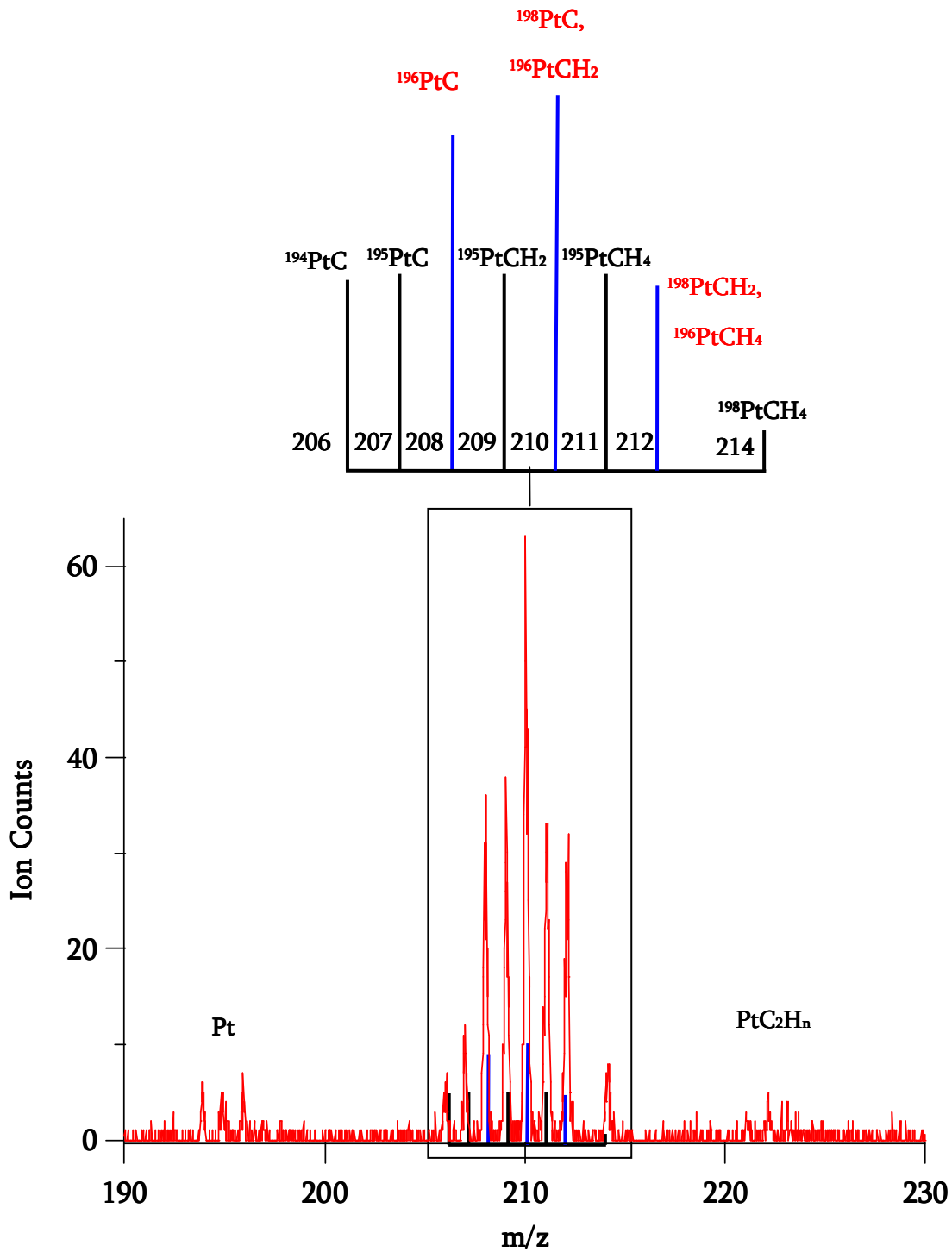


Figure 5.3: The mass spectrum of the ionized products from the reaction of laser-ablated platinum with CH_4 at 11 eV. The enlarged portion shows the assignment of the PtCH_n peaks.

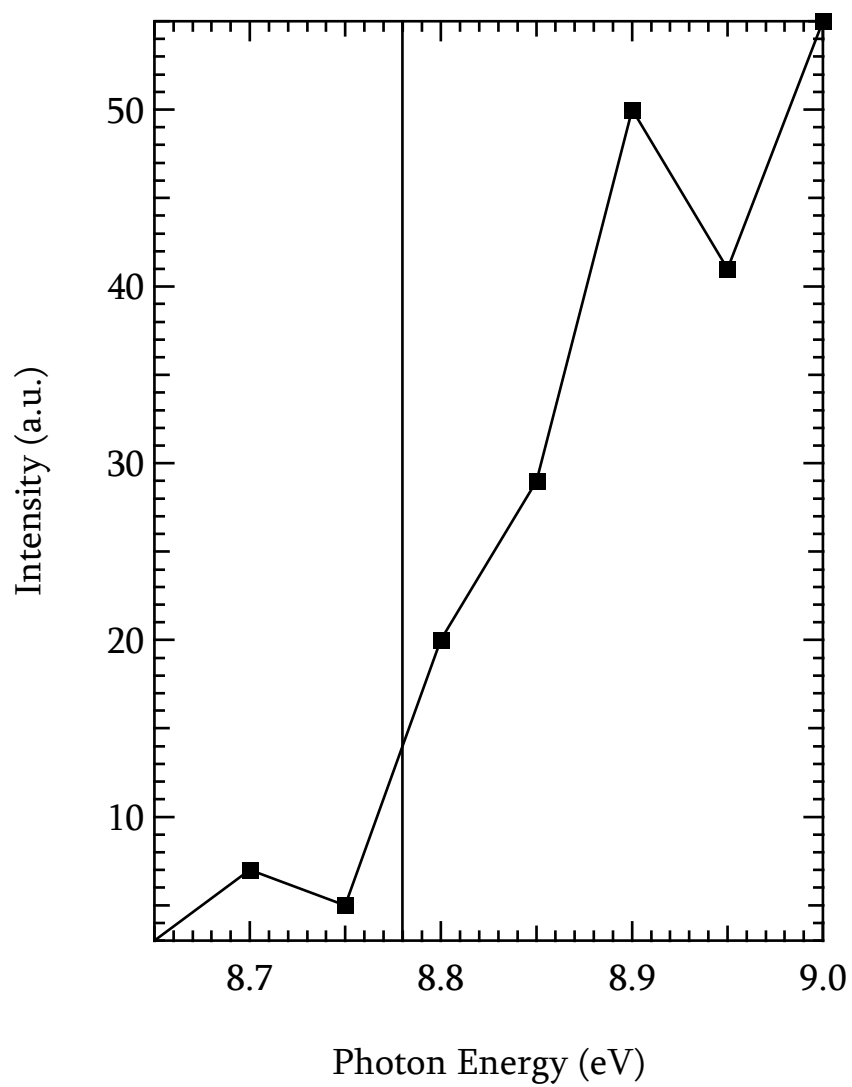


Figure 5.4: The ionization energy onset for $^{195}\text{PtCH}_2$ made via reaction of methane with platinum. The vertical line shows the ionization energy of 8.78 eV.

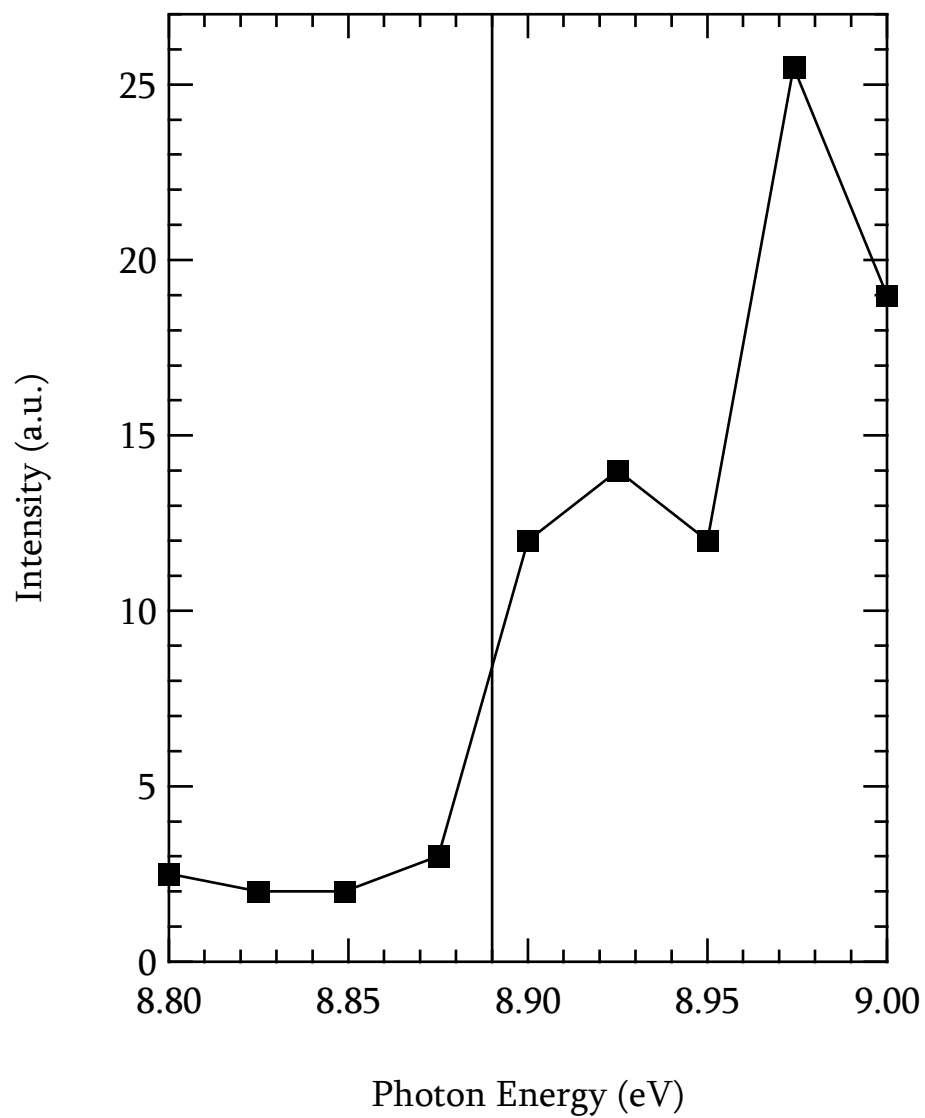


Figure 5.5: The ionization energy onset for the insertion intermediate, $\text{H-}^{195}\text{Pt-CH}_3$ made via reaction of methane with platinum. The vertical line shows the ionization energy of 8.89 eV.

5.4 Discussion

Bond strengths for many transition metal cations have been measured in guided ion beam experiments in which the charged products of an endothermic reaction are monitored as a function of collision energy.^{3,21} Measuring bond strengths in neutrals is more challenging, as it is much harder to control the collision energy, and even identifying the products is difficult. The classic method of measuring bond strengths of nonvolatile and transient molecules is Knudsen cell mass spectrometry in which equilibrium concentration of neutrals are sampled, ionized, and mass analyzed.²² Unfortunately, this typically requires very high temperatures (~2300 K for FeC) and is only applicable to simple compounds, due to interfering side reactions. However, neutral bond strengths can be accurately measured indirectly, by combining cation bond strengths with measured ionization energies.²⁰

5.4.1 Potential Energy Surface for Methane Activation by Platinum

We use the bond dissociation energies measured by Armentrout and coworkers for platinum containing cations⁵ along with ionization energies of PtCH₂, H-Pt-CH₃, and PtH₂ and PtC²⁰ to derive bond energies for the neutrals. For example, figure 5.6 shows the thermodynamic cycle used to derive the bond dissociation energy for PtCH₂;

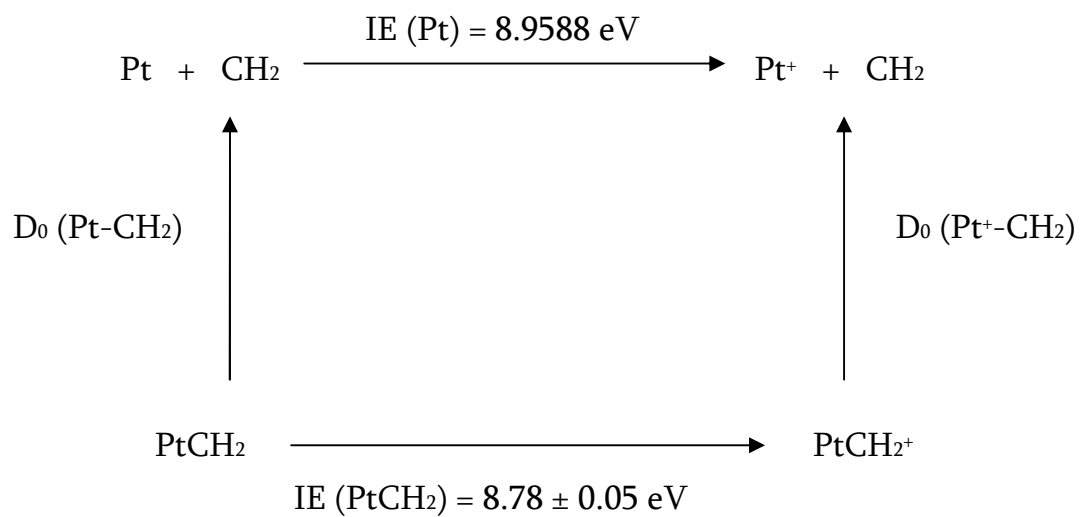


Figure 5.6: Thermodynamic cycle used to calculate the bond dissociation energy of Pt-CH₂.

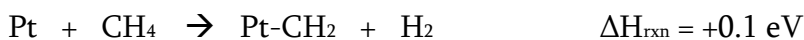
$$D_0(\text{Pt-CH}_2) = D_0(\text{Pt}^+\text{-CH}_2) + \text{IE}(\text{Pt-CH}_2) - \text{IE}(\text{Pt})$$

$$D_0(\text{Pt-CH}_2) = 4.62 \pm 0.06 \text{ eV}$$

This is a 0 K value. Table 5.1 summarizes the derived bond strengths for compounds related to methane activation by Pt and Pt⁺. Using this information about Pt-CH₂, we can calculate the enthalpy for the Pt + CH₄ reaction:



These two combined provide the dehydrogenation reaction enthalpy.



A second key finding is the energy of the H-Pt-CH₃ insertion intermediate. Based on its ionization energy and the energetics of [H-Pt-CH₃]⁺, it lies 1.69 eV below Pt + CH₄. The potential energy surface (figure 5.7) for the Pt + CH₄ reaction was created using the above information. The energies of transition states and minor intermediates that were not observed were estimated using the calculations.¹² This potential energy surface will guide our discussion of other experimental and computational studies of the Pt + CH₄ reaction.

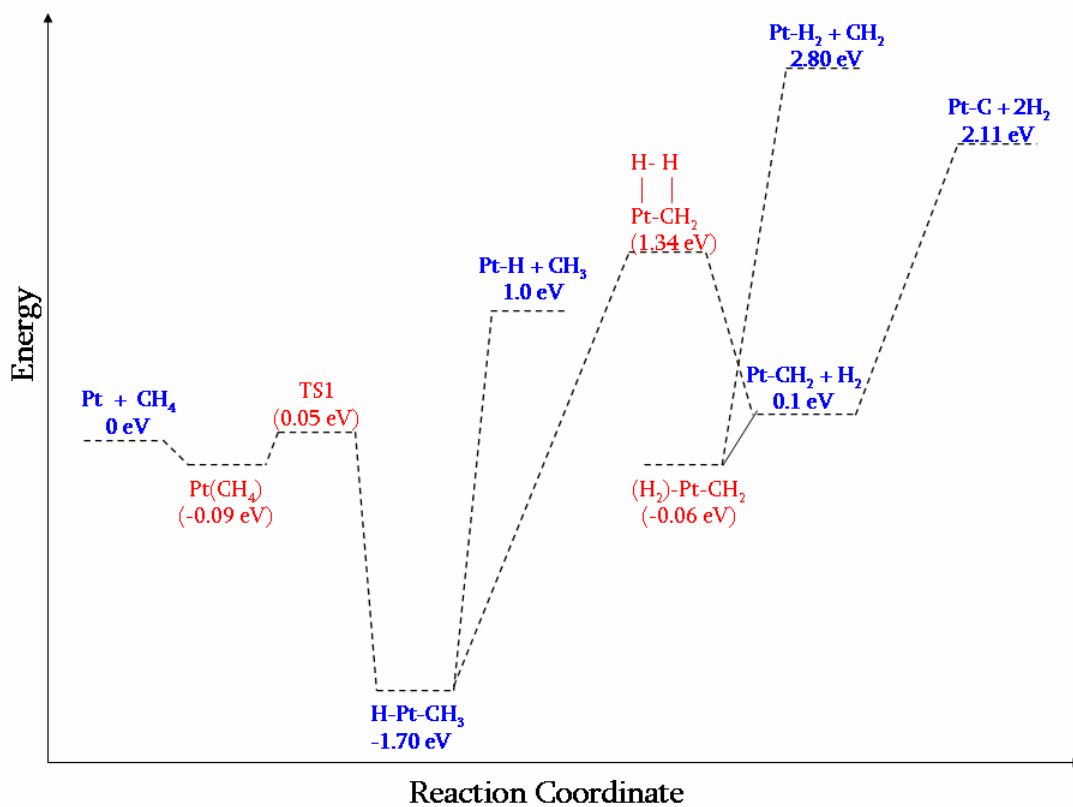


Figure 5.7: The potential energy surface for the reaction of methane with platinum. Values in parenthesis are based on calculations.⁹

	IE (eV)	D ₀ (cation) (eV)	D ₀ (neutral) (eV)
Pt	8.9588	-	-
Pt – H	-	2.81 ± 0.05	3.48
Pt – H ₂	9.35 ± 0.05	1.52 ± 0.12	1.91 ± 0.12
Pt – C	9.45 ± 0.05	5.43 ± 0.05	5.95 ± 0.07
Pt – CH ₂	8.78 ± 0.05	4.80 ± 0.03	4.62 ± 0.06
Pt – CH ₄	8.89 ± 0.05	1.77 ± 0.08	1.70 ± 0.09

Table 5.1: Ionization energies and bond strengths for platinum containing compounds at 0 K. Cation values are from Armentrout and co-workers⁵ and Pt-H neutral bond strength from Brooks and co-workers.²³

5.4.2 Experimental and Theoretical Studies of Methane Activation by Pt Atoms

There have been several studies on the reaction of methane with neutral platinum atoms.¹²⁻¹⁴ Weisshaar and Carroll monitored the reaction by using laser induced fluorescence detection to measure the decay of the ground state metal atom concentration with respect to hydrocarbon number density at a given reaction time.¹² The reaction rate was measured at 300 K at several He pressures. It was found that the rate increases with the pressure of He, which is maximum at 0.5-0.8 Torr. The rate of reaction with ethane is much higher, and is independent of helium pressure. Theory predicts that Pt dehydrogenation of methane is endothermic by 0.3 eV.¹²

These results suggest that Pt reacts with CH₄ to produce the insertion intermediate H-Pt-CH₃. This intermediate is stabilized by colliding with He gas and does not go on to produce the endothermic final products PtCH₂ and H₂. In addition, the calculations predict that there is a 1.34 eV barrier between H-Pt-CH₃ and products.

These calculations, as well as experiments and calculations by Campbell¹⁴ highlight the influence of both the ground state ($s^1d^9\ ^3D_3$) and low lying excited state ($d^{10}\ ^1S_0$) on producing the insertion intermediate H-Pt-CH₃. Spin-orbit interaction between these two states deepens the insertion potential well and also causes triplet-singlet crossing at lower energies. This provides the triplet ground state easy access to the singlet insertion well at thermal energies. This underscores the importance of properly treating unpaired electrons, low lying electronic states and relativistic effects to accurately describe reactions of transition metals.

Our experiments show that the calculations slightly underestimate platinum bond strengths. The overall dehydrogenation reaction is 0.1 eV endothermic, rather than the 0.3 eV endothermic predicted by theory. The global minimum is the insertion intermediate, H-Pt-CH₃, which experimentally lies 1.70 eV below Pt + CH₄. The calculations predict it is only 1.39 eV below the reactants. These underestimated stabilities also suggest that the calculated barrier to products is too high.

5.4.3 Methane Activation by Platinum Cation

Armentrout and co-workers have extensively studied C-H bond activation in methane by platinum cation.⁵ They have used reaction and collision induced dissociation studies over a wide range of kinetic energies to measure energetics of the potential energy surfaces for endothermic and exothermic reactions and used theory to fill in gaps. This resulting potential energy surface is shown in figure 5.8. Pt^+ reacts with CH_4 without a barrier to produce the intermediate $\text{H-Pt}^+-\text{CH}_3$, which is the global minimum on the potential energy surface. The first C-H bond activation is possible due to the metal orbitals: empty $6s$ acts as the acceptor while filled $5d-\pi$ act as the donor. The second C-H bond activation also takes place with a small barrier, below the reactants' energy. The resulting intermediate, $(\text{H})_2\text{Pt}^+\text{CH}_2$, produces $(\text{H}_2)\text{Pt}^+\text{CH}_2$ through reductive elimination. The $(\text{H}_2)\text{Pt}^+\text{CH}_2$ then goes on to make $\text{PtCH}_2^+ + \text{H}_2$ via decomposition. Overall, the reaction is exothermic by 0.09 eV relative to reactants. All of the barriers lie below the reactant energy, so the reaction is efficient at low collision energies. At higher collision energies other products are formed. Above 2 eV the Pt^+-H and Pt^+-CH_3 products are formed via simple bond cleavage from $\text{H-Pt}^+-\text{CH}_3$. These products are kinetically favored at high collision energy, and dominate the thermodynamically favored PtCH_2^+ , which is made via a tight transition state. At 2.5 eV or higher the PtH^+ channel dominates over the isoenergetic PtCH_3^+ channel due to angular momentum constraints. At even higher

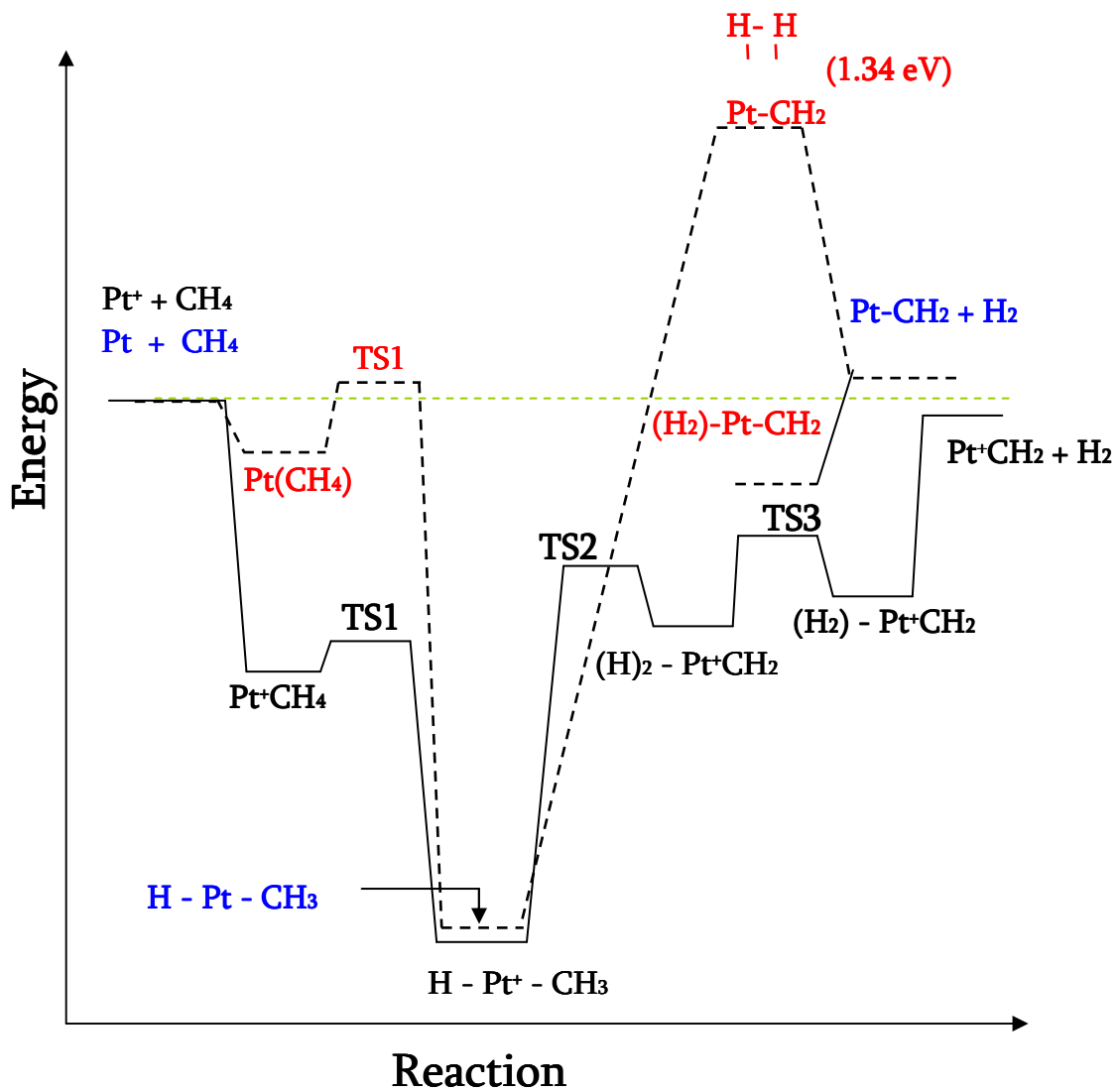


Figure 5.8: Comparison of $\text{Pt}^+ + \text{CH}_4$ reaction with $\text{Pt} + \text{CH}_4$ reaction.

energies PtC^+ and PtCH^+ are produced as results of dehydrogenation of PtCH_2^+ and PtCH_3^+ . These endothermic products are kinetically favored at higher energies.

5.4.4 Effect of Charge on Methane Activation by Platinum

Comparing the reactions of Pt and Pt^+ with methane is useful in understanding how charge and electron occupancy affect the reaction thermodynamics and kinetics. Figure 5.7 compares the potential energy surfaces for $\text{Pt} + \text{CH}_4$ and $\text{Pt}^+ + \text{CH}_4$. In each case, the zero of energy is the reactants. The global minimum on the potential energy surface is due to the insertion intermediate, and the relative energies of H-Pt-CH_3 and $\text{H-Pt}^+-\text{CH}_3$ are very similar. For the cation, there is no barrier to forming $\text{H-Pt}^+-\text{CH}_3$, which is a direct result of the electrostatic attraction between the positive metal core and electron rich methane. For the neutral, insertion may have a small barrier. The calculations¹² predict a ~ 0.05 eV barrier, but this does not include spin-orbit coupling, which should lower the barrier.

There is a very significant difference in the mechanism when it comes to the second C-H bond activation. The cation follows an α -migration transition state to produce $(\text{H})_2\text{-Pt}^+-\text{CH}_2$, followed by H-H recombination to form $(\text{H}_2)\text{Pt}^+\text{CH}_2$, all with small barriers.⁵ The neutral follows a α -elimination transition state via a four-center complex which has a large barrier.¹² For the neutral, the $(\text{H})_2\text{-Pt-CH}_2$ intermediate appears to lie at too high an energy to be involved in the mechanism. This is likely an electron occupancy effect: neutral Pt has too few empty orbitals to form the three (or

four) bonds required. Neutral iridium, which is isoelectronic to Pt^+ , is predicted¹² to react via an $(\text{H})_2\text{-M-CH}_2$ intermediate just like Pt^+ . The overall reaction energetics for Pt and Pt^+ are similar: the cation products are 0.18 eV below the neutral products. As a result, the overall reaction is slightly exothermic for Pt^+ and slightly endothermic for Pt. We do not have $\text{IE}(\text{PtCH}_3)$ to calculate the energy of the $\text{PtCH}_3 + \text{H}$ product, but the relative energetics of other endothermic products such as PtH , PtH_2 , and PtC do not depend strongly on charge.

The overall conclusion, as shown in figure 5.7, is that dehydrogenation of methane by neutral platinum atoms is not possible at thermal energies because the reaction is endothermic and because a large barrier precedes the final products. With the platinum cation the same reaction leads to products at thermal energies being slightly exothermic, with no large barriers.

5.5 References

- (1) Usui, K.; Kidena, K.; Murata, S.; Nomura, M.; Trisunaryanti, W. *Fuel* **2004**, *83*, 1899.
- (2) Irikura, K. K.; Beauchamp, J. L. *J. Phys. Chem.* **1991**, *95*, 8344.
- (3) *Organometallic Ion Chemistry*; Freiser, B. S., Ed.; Kluwer Academic Publishers: Dordrecht, 1996; Vol. 15.
- (4) Eller, K.; Schwarz, H. *Chem. Rev.* **1991**, *91*, 1121.
- (5) Zhang, X. G.; Liyanage, R.; Armentrout, P. B. *J. Am. Chem. Soc.* **2001**, *123*, 5563.
- (6) Heinemann, C.; Wesendrup, R.; Schwarz, H. *Chem. Phys. Lett.* **1995**, *239*, 75.
- (7) Koszinowski, K.; Schröder, D.; Schwarz, H. *J. Phys. Chem. A* **2003**, *107*, 4999.
- (8) Crabtree, R. H. *Wiley: New York* **2005**, *4th ed.*
- (9) Centi, G.; Cavani, F.; Trifirò, F. *Selective Oxidation by Heterogeneous Catalysis*; Kluwer Academic: New York, 2001.
- (10) Heinemann, C.; Schwarz, H.; Koch, W.; Dyall, K. G. *J. Chem. Phys.* **1996**, *104*, 4642.
- (11) Weisshaar, J. C. *Acc. Chem. Res.* **1993**, *26*, 213.
- (12) Carroll, J. J.; Weisshaar, J. C.; Siegbahn, P. E. M.; Wittborn, C. A. M.; Blomberg, M. R. A. *J. Phys. Chem.* **1995**, *99*, 14388.
- (13) Carroll, J. J.; Weisshaar, J. C. *J. Phys. Chem.* **1996**, *100*, 12355.
- (14) Campbell, M. L. *J. Chem. Soc. Faraday Trans.* **1998**, *94*, 353.

- (15) Husband, J.; Aguirre, F.; Thompson, C. J.; Laperle, C. M.; Metz, R. B. *J. Phys. Chem. A* **2000**, *104*, 2020.
- (16) Aguirre, F.; Husband, J.; Thompson, C. J.; Metz, R. B. *Chem. Phys. Lett.* **2000**, *318*, 466.
- (17) Metz, R. B. *Int. Rev. Phys. Chem.* **2004**, *23*, 79.
- (18) Nicolas, C.; Shu, J.; Peterka, D. S.; Poisson, L.; Leone, S. R.; Ahmed, M. *J. Am. Chem. Soc.* **2006**, *128*, 220.
- (19) Belau, L.; Wilson, K. R.; Leone, S. R.; Ahmed, M. *J. Phys. Chem. A* **2007**, *111*, 7562.
- (20) Citir, M.; Metz, R. B.; Belau, L.; Ahmed, M. *J. Phys. Chem. A* **2008**, *112*, 9584.
- (21) Armentrout, P. B. *Int. J. Mass Spectrom.* **2000**, *200*, 219.
- (22) Drowart, J.; Chatillon, C.; Hastie, J.; Bonnell, D. *Pure Appl. Chem.* **2005**, *77*, 683.
- (23) Scheer, M.; Haugen, H. K.; Brooks, R. L. **1999**, *61*, 12505.

CHAPTER 6

CONCLUSIONS AND FUTURE WORK

6.1 Conclusions

All three projects share the common interest in our lab: to strive to understand the covalent and non-covalent interactions in transition metal chemistry whether cation, dication or neutral. We use spectroscopy with well-defined photon energies in all three experiments so we can quantitatively study thermodynamics, bonding and dynamics of transition metal systems. The projects that are described in chapter 3 and chapter 4 were conducted at the our lab using photofragment spectroscopy and the studies in chapter 5 were done at the Advanced Light Source, Lawrence Berkeley Labs using photoionization. The first two projects that are described look at cation chemistry in detail using the spectroscopy and dissociation dynamics of the molecules and the last project looks into neutral atom chemistry using ionization energies of the molecules.

6.1.1 Photofragment Spectroscopy of $\text{TiO}^+(\text{CO}_2)$

The TiO neutral has been detected near numerous stars and its presence is used to identify cool M and S class stars. Neutral TiO is detected based on absorption in three strong electronic transitions in the visible. The resulting rotational structure

is used to measure the local temperature. The low ionization energy of TiO and high bond strength of TiO^+ make it likely that it is present in circumstellar envelopes. The electronic spectrum of TiO^+ has not been measured, which clearly hampers its detection. The high $\text{Ti}^+\text{-O}$ bond strength also makes it difficult to detect via photofragment spectroscopy. We would like to use our calculations on TiO^+ and $\text{TiO}^+(\text{CO}_2)$, as well as experimental results on $\text{TiO}^+(\text{CO}_2)$, to predict the electronic spectroscopy of bare TiO^+ .

The resonant photodissociation spectrum of $^{48}\text{TiO}^+(\text{CO}_2)$ is obtained by monitoring the only fragment $^{48}\text{TiO}^+$. This provides the absorption spectrum of $\text{TiO}^+(\text{CO}_2)$ when absorption leads to dissociation. The spectrum is richly structured, with four vibrational bands separated by $\sim 950\text{ cm}^{-1}$. Each band consists of several peaks separated by $\sim 45\text{ cm}^{-1}$. The $\sim 950\text{ cm}^{-1}$ progression is due to the covalent TiO stretch. Isotopic shift studies aid the assignment of the band origin. The low-frequency vibrations are due to the non-covalent metal- CO_2 stretch (186 cm^{-1}) and rock (45 cm^{-1}). The four Ti-O stretching bands exhibit almost identical low-frequency structure, indicating that there is little coupling between the covalent Ti-O stretch and the metal- CO_2 stretch and rock. The long progressions observed in the metal-ligand rock and, to a lesser extent, stretch indicate that the TiO^+ electronic state substantially affects its interaction with CO_2 . Another observation made is that slow dissociation leads to peak tailing (figure 3.5). The lifetime drops rapidly with

increasing photon energy, until no tailing is observed at energies above 16500 cm⁻¹, indicating lifetimes below 50 ns.

Electronic structure calculations were carried out on TiO⁺ and TiO⁺(CO₂) to determine which electronic state is responsible for the observed transitions and also how the CO₂ affects the vibrational frequencies and electronic spectroscopy of TiO⁺. Thus, we can use our experimental results on TiO⁺(CO₂) to predict the electronic spectrum of bare TiO⁺ in the visible. Calculations show that the transitions to the ²A' (²Σ) state are predicted to be about an order of magnitude weaker than those to the ²A' (²Π) states. We observed only one electronic transition which is assigned to the ²A' (²Π) state. Calculations also show that interaction with CO₂ splits the ²Π excited state of TiO⁺ into two states. The lower-energy state corresponds to an electron in the out-of-plane π orbital, resulting in less repulsion with CO₂ than promotion to the in-plane π orbital. Binding to the CO₂ lowers the symmetry, so transitions to the ²A' (²Σ) state are no longer forbidden, but are weak with $f \approx 0.0007$. The low-energy ²A' component of the ²Π state retains significant oscillator strength ($f \approx 0.0057$), while the ²A' component has $f \approx 0$.

6.1.2 Microsolvation of Ni²⁺ and Co²⁺ by Acetonitrile and Water: Photodissociation

Dynamics of M²⁺(CH₃CN)_n(H₂O)_m

The microsolvation of metal dication by acetonitrile and water study was specifically done to understand the interaction of solvents with the metal center and

how the nature of the solvent, protic water and aprotic acetonitrile, affect binding and charge transfer dynamics. The clusters were produced by electrospray and characterized by photofragment spectroscopy in an ion trap dual time-of-flight mass spectrometer. The homogeneous clusters with acetonitrile, $n=4$ and 3 dissociated by simple solvent loss and only $n=2$ showed electron transfer as a dissociation pathway. Mixed clusters with water and acetonitrile reveal more interesting dissociation dynamics. Again, larger clusters, ($n=4$ and 3) show simple solvent loss. Water loss was favored over acetonitrile loss by a significant yield which is understandable because acetonitrile is a better solvent in the gas phase due to its higher dipole moment and polarizability. Proton transfer was observed as a minor channel for $M^{2+}(\text{CH}_3\text{CN})_2(\text{H}_2\text{O})_2$ and $M^{2+}(\text{CH}_3\text{CN})_2(\text{H}_2\text{O})$ but was not seen in $M^{2+}(\text{CH}_3\text{CN})_3(\text{H}_2\text{O})$. In our lab we previously observed proton loss as the major channel for $M^{2+}(\text{H}_2\text{O})_4$. Studies of deuterated clusters confirm that water acts as the proton donor.

Considering the photodissociation yield it was clear that four coordinate clusters of cobalt dissociated more readily than nickel clusters whereas for the three coordinate clusters, dissociation was more efficient for nickel clusters over cobalt. For the two coordinate clusters, dissociation is via electron transfer but the yield is low for both metals. Our calculations of reaction energetics, dissociation barriers, and the positions of excited electronic states complemented the experimental work.

6.1.3 Ionization Energies of PtC_nH_m and a Potential Energy Surface for the $\text{Pt} + \text{CH}_4$ reaction

Although the US has extensive natural gas reserves, our petroleum production comes from consuming scarce crude oil. The challenge lies in finding an efficient catalyst that can convert methane to larger hydrocarbons, which can be used to revolutionize the usage of natural gas. This is where the importance of C-H bond activation in methane by transition metals becomes vital for industrial purposes. Gas phase Pt^+ , along with several other third-row transition metal cations, efficiently activate methane at thermal energies, producing $\text{H}_2 + \text{MCH}_2^+$, which can then react with additional CH_4 , forming $\text{MC}_n\text{H}_{2n}^+$.¹ This reaction is not observed for the corresponding ground state neutrals, although platinum does insert into methane forming H-Pt-CH₃.

We studied PtCH_2 and the H-Pt-CH₃ reaction intermediate by reaction of laser ablated platinum atoms with methane and subsequent measurement of their photoionization efficiencies (PIE). Ionization energies are derived from the PIEs. Armentrout and co-workers have studied the same system, C-H bond activation in methane, using the platinum cation whereas we are used the platinum neutral.² Using their bond dissociation energies and the ionization energies we found for the neutrals, we are able to derive bond energies for the neutrals. Using the resulting experimental bond energies of PtH, PtH₂, PtC, and PtCH₂, and the H-Pt-CH₃

intermediate, along with calculated values for the transition state energies we were able to produce a potential energy surface for methane activation by platinum atoms.

The global minimum on the potential energy surface is due to the intermediate H-Pt-CH₃ which is 1.70 eV below Pt + CH₄ reactants. Insertion has a very small barrier, -0.05 eV, making this a favorable process. Up to this point, the neutral and cation reactions are very similar, and [H-Pt-CH₃]⁺ is only slightly more stable, 1.77 eV below Pt⁺ + CH₄. For the cations the second C-H bond activation also takes place at low energies according to calculations. This intermediate, (H)₂PtCH₂⁺, produces (H₂)Pt⁺CH₂ through a reductive elimination process. The intermediate later goes on to make Pt⁺CH₂ via decomposition. Overall the reaction Pt⁺ + CH₄ → PtCH₂⁺ + H₂ is exothermic by 0.19 eV. There are no barriers above the reactant energy, consistent with efficient reaction at thermal energies.

The situation for the neutral is quite different. First, our experiments show that the Pt + CH₄ → PtCH₂ + H₂ reaction is endothermic by 0.1 eV. Calculations predict that the second C-H bond activation to produce (H₂)PtCH₂ has a barrier of 1 eV above products, or 1.34 eV above reactants.³ Other products, such as PtC + 2H₂ or H-Pt-H + CH₂ are substantially more endothermic. These results agree with the experimental observation that neutral platinum readily inserts into methane, but no subsequent reaction to produce PtCH₂ occurs.

6.2 Future Work on the Electrospray Ionization Instrument

6.2.1 Electronic Spectroscopy

The first project that was studied using this instrument was $M^{2+}(\text{CH}_3\text{CN})_n(\text{H}_2\text{O})_m$ because it was a new addition to our lab (in 2002). This instrument differs from the laser ablation instrument in several ways: ions are made by electrospray ionization in the room and introduced to the vacuum via a capillary and an ion funnel for enhanced ion transmission, and ions are collected in an ion trap, where they are thermalized. Therefore, this instrument can be used to study many interesting and different molecules.

Most first row transition metal ions are six-coordinate (octahedral or slightly distorted octahedral geometry) in aqueous solutions. The conventional explanation for the characteristic absorption bands of these ions in the visible and near ultraviolet regions is due to transitions between d orbitals. According to crystal field theory the degenerate atomic 3d orbitals split into set of molecular e_g and t_{2g} orbitals. These d-d bands are symmetry forbidden in octahedral symmetry, making them weak. This weak transition is reflected in small extinction coefficients generally in the magnitude of $\epsilon = 1\text{-}10 \text{ M}^{-1} \text{ cm}^{-1}$. Previously in our lab, Co^{2+} and Ni^{2+} have been studied with water, and methanol as solvents to understand the spectroscopy and photodissociation dynamics.^{4,5}

6.2.1.1 Electronic Spectroscopy of $M^{2+}(\text{solvent})_n$ for $M = \text{Ni}$ and Co at 80 K

The motivation for this study arose when Gilson and Krauss came up with the controversial idea that $\text{Co}^{2+}(\text{H}_2\text{O})_6$ is not responsible for bulk absorption properties and that a strongly absorbing minor species could play the necessary role.^{6,7} Their calculations show transition energies and oscillator strengths for $\text{Co}^{2+}(\text{H}_2\text{O})_6$ to have very low ($f < 10^{-6}$) oscillator strength, thus leaving minor species such $\text{Co}^{2+}(\text{H}_2\text{O})_5$ and $\text{Co}^{2+}(\text{H}_2\text{O})_4$ as likely chromophores. The penta-coordinate species is predicted to have the largest effect. Later, Fedorchuk and Swaddle contested Krauss' calculation by stating that $\text{Co}^{2+}(\text{H}_2\text{O})_6$ is the chromophore responsible for absorption properties through thermal distortions and vibronic coupling.⁸ Previously, our lab studied gas phase $\text{Co}^{2+}(\text{H}_2\text{O})_n$ for $n=4-7$. Our lab's photodissociation results (figure 6.1) show that the $n=6$ chromophore is responsible for the room temperature solution's absorption spectrum since gas phase and solution phase spectra are similar.⁵ It is slightly disappointing that the photodissociation spectra of gas phase $\text{Co}^{2+}(\text{H}_2\text{O})_4$ and $\text{Co}^{2+}(\text{H}_2\text{O})_6$ are nearly as broad as the solution spectra.

At room temperature, a molecule such as $\text{Co}^{2+}(\text{H}_2\text{O})_6$ has many populated low frequency vibrations. This could broaden the spectrum as transitions take place from vibrationally excited molecules in the ground electronic state. As figure 6.2 shows, cooling the ions down to 80 K greatly reduces this effect and should lead to a better resolved spectrum. We modified the apparatus by adding a liquid N_2 cooled can that

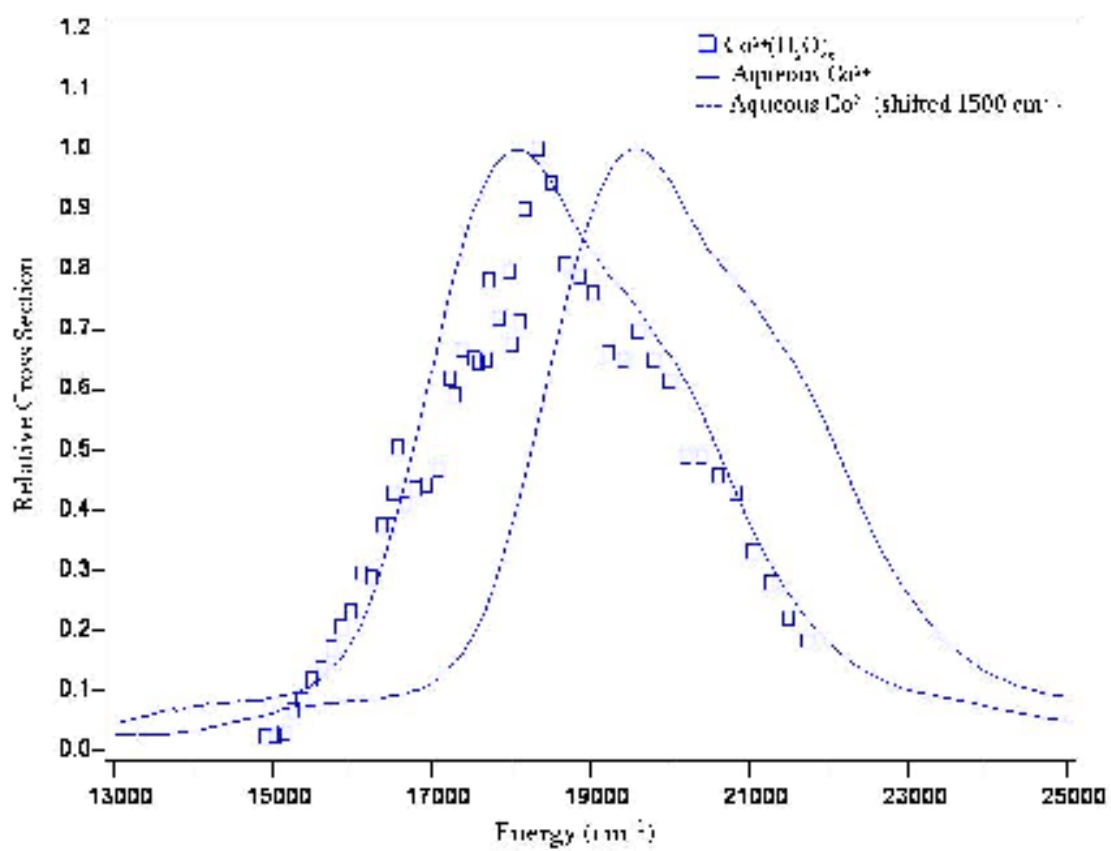


Figure 6.1: Total photodissociation spectrum of $\text{Co}^{2+}(\text{H}_2\text{O})_6$ and the absorption spectrum of Cobalt (II) in aqueous solution.

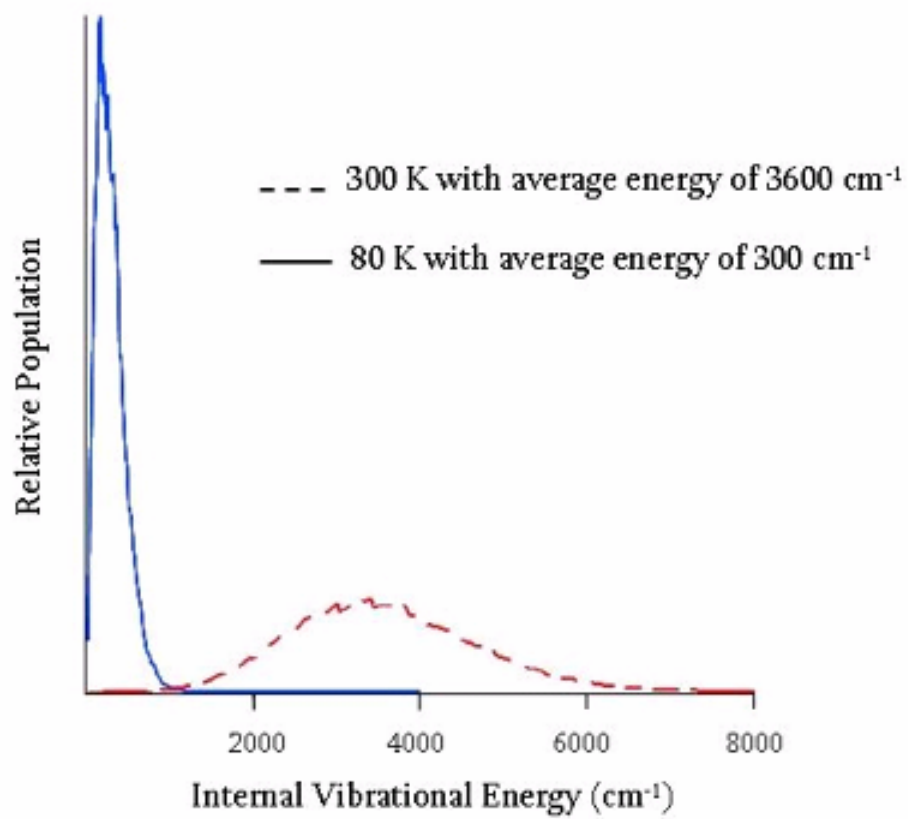


Figure 6.2: Spectral resolution is greatly improved by lowering the internal energy of the ions. The vibration energy calculations were done on $\text{Zn}^{2+}(\text{H}_2\text{O})_6$.

surrounds the ion trap, cooling the trap, helium bath and ions to ~ 80 K.

6.2.1.2 Electronic Spectroscopy of $\text{Cu}^{2+}(\text{H}_2\text{O})_n$ at 80 K

As Cu^{2+} is d^9 , $\text{Cu}^{2+}(\text{H}_2\text{O})_6$ distorts from octahedral geometry due to the Jahn-Teller effect. A few studies have shown that metals with Jahn-Teller effect exchange water ligands with solvent water molecules at faster rate than metals without this effect.⁹ It would be interesting to compare previously studied metals like Co^{2+} and Ni^{2+} with Cu^{2+} . Thus, according to calculations, $\text{Cu}^{2+}(\text{H}_2\text{O})_4$ is square planar whereas $\text{Co}^{2+}(\text{H}_2\text{O})_4$ and $\text{Ni}^{2+}(\text{H}_2\text{O})_4$ are tetrahedral. The tetrahedral complexes absorb much more strongly than square planar or octahedral since the d-d transition is symmetry allowed. An added motivation for this study comes after Stace and co-workers have stated that larger clusters ($n > 4$) of $\text{Cu}^{2+}(\text{H}_2\text{O})_n$ are formed by adding water molecules to the second solvation shell of $\text{Cu}^{2+}(\text{H}_2\text{O})_4$.¹⁰ This would be in contrast to solution, where copper (II) is six coordinate. Using photodissociation spectra, we can look into whether $\text{Cu}^{2+}(\text{H}_2\text{O})_6$ is four or six coordinate.

The second ionization energy of M^{2+} and the M^+-OH bond strength influence the energetics of charge transfer as well as the number of solvent molecules needed to stabilize the metal. By studying the charge transfer dissociation of $\text{Cu}^{2+}(\text{H}_2\text{O})_4$ we can compare it to two systems with significantly different energetics: $\text{Co}^{2+}(\text{H}_2\text{O})_4$ and $\text{Ni}^{2+}(\text{H}_2\text{O})_4$. Vukomanovic's study has shown that CID of $\text{Cu}^{2+}(\text{H}_2\text{O})_n$ leads to loss of

H₂O for both large and small ions and smaller ions tend to dissociate by charge reduction.¹¹ We could measure the dissociation pathways and kinetic energy release of fragment ions following visible photolysis of Cu²⁺(H₂O)_n, examining ions at 300 K and 80 K. Cooling the ions will provide us a well defined, lower internal energy, as shown in figure 6.2, making the comparison between theory and experiment more detailed.

6.2.2 Vibrational Spectroscopy

Obtaining vibrational spectra of the ions using photofragment spectroscopy is more challenging than electronic spectroscopy, as one infrared photon usually does not have enough energy to dissociate the cluster. Two possible methods of obtaining vibrational spectra are to use infrared multiphoton dissociation (IRMPD) or a spy molecule (“argon tagging”). Our group has used both of these methods to study singly charged transition metal ions with different ligands.^{12,13} The clusters we are hoping to study are large enough to conduct experiments using IRMPD. This requires rapid intramolecular vibrational redistribution so that the excited molecules get to absorb more photons at the resonant wavelength. The other method we propose, argon tagging, can be done in the liquid nitrogen cooled ion trap by using argon as the buffer gas instead of helium. Absorption of IR photons leads to loss of the weakly bound Ar atom. Argon atoms have a small effect on the vibrational frequencies of the molecule. The vibrational frequency of the untagged molecules can be estimated by

measuring the spectra of clusters with varied number of argon atoms. Vibrational spectroscopy studies can be carried out with an infrared laser system that we have in our lab. It is tunable from 600-4000 cm^{-1} .

6.2.2.1 Vibrational Spectroscopy of $\text{Cu}^{2+}(\text{H}_2\text{O})_n$ and $\text{Co}^{2+}(\text{CH}_3\text{CN})_n$ Clusters

The following study would complement the previous electrospray spectroscopy studies and will gather information via vibrational spectroscopy of the molecule. The vibrational spectrum of solvated M^{2+} ions is very sensitive to their structure. For example, consider $\text{Cu}^{2+}(\text{H}_2\text{O})_6$. As shown in figure 6.3, when the cluster is six coordinate, calculations predict that the O-H stretch is intensified with a slight red shift in comparison to free H_2O . This will be different if the complex is four coordinate, since the O-H stretch shows a much larger red shift and a higher intensity. Ziegler and co-workers have calculated that the four coordinate complex is more stable by 71 kJ/mol using density functional theory without zero point energy correction.¹⁴ We have carried out B3LYP calculations, using a larger basis set (SDD for Cu and 6-311++G** for O and H) that predict it is only more stable by 25 kJ/mol. Experiments in this area would clearly illuminate this further. Our study would experimentally explore the competition between metal ion-water and water-water interactions, which is very challenging to calculate.

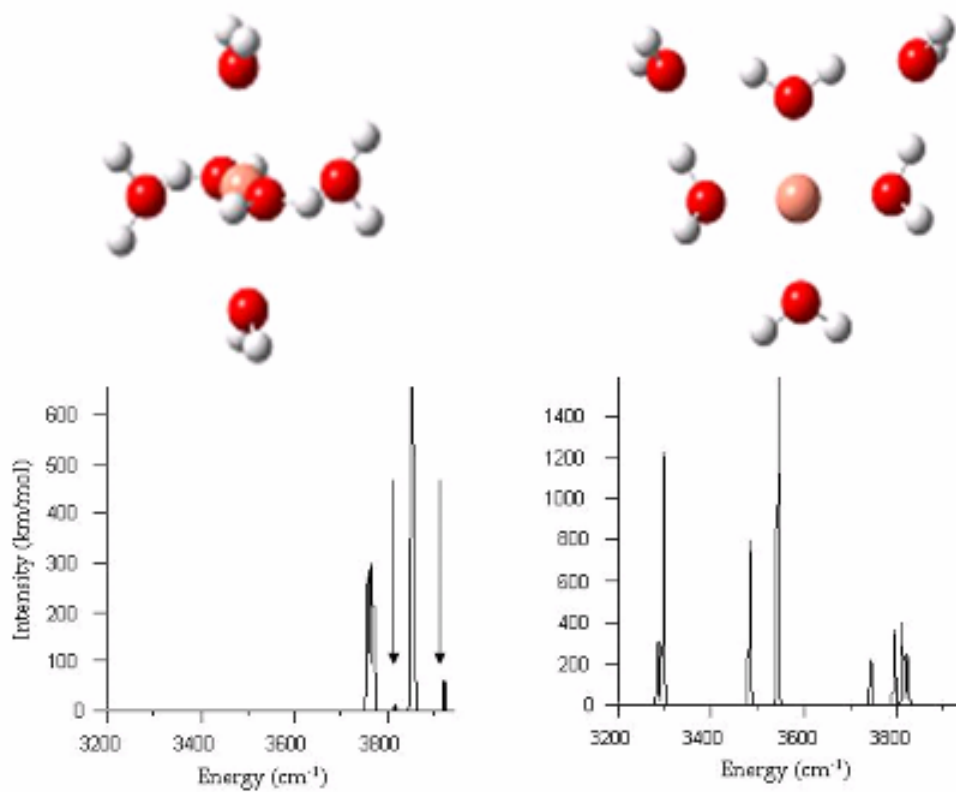


Figure 6.3: Structures and calculated IR spectra of two possible structures of $\text{Cu}^{2+}(\text{H}_2\text{O})_6$. Arrows and solid bars indicate the calculated positions and intensities for bare H_2O .

Also, previous studies in our lab have shown that $\text{Co}^{2+}(\text{CH}_3\text{OH})_4$ has a similar visible photofragment spectrum to $\text{Co}^{2+}(\text{H}_2\text{O})_4$, suggesting it is also tetrahedral.¹⁵ As the number of methanol molecules increases, the spectra of $\text{Co}^{2+}(\text{CH}_3\text{OH})_n$ (for $n=5$ & 6) look like that of tetrahedral $\text{Co}^{2+}(\text{CH}_3\text{OH})_4$, suggesting that these clusters are also four coordinate. This is different from $\text{Co}^{2+}(\text{H}_2\text{O})_6$ which is six coordinate. So another interest we have is to explore the possibility of using IR studies with $\text{Co}^{2+}(\text{CH}_3\text{OH})_n$.

6.2.2.1 Vibrational Spectroscopy of Metal Dication – Polypeptide Complexes

Still, not much is understood about the effect water molecules play in the conformations and stability of peptides. Gas phase studies of bare and hydrated peptides can explore these effects. Bowers' group has studied the hydration equilibrium of small peptides using ES-MS and showed that peptide structural changes are a function of water molecules.¹⁶ The ability to produce functional peptides in the gas phase opens up another avenue to look at metal ions in the context of biological systems. Lately many researches are heading toward exploring metals in biology.^{17,18} Some researches have explored the CID of alkali metal peptide clusters to find different dissociation pathways based on the metal binding site.¹⁹ Knowing the fragmentations can reveal important structural information of these complexes. For example, Gross and co-workers have found that the position of aromatic rings plays a key role in which position fragmentation takes place on a peptide chain that is

attached to a doubly charged transition metal ion.²⁰ Photoexcitation can lead to different dissociation pathways than CID. We could study photodissociation of small peptide-metal clusters with the same metals (Cu^{2+} , Ni^{2+} and Co^{2+}) and compare photodissociation paths with CID results. The peptides of interest will vary with aromatic (F-phenylalanine) and non-aromatic (A-alanine) functional groups such as FAAA, AFAA, AAFA and AAAF. The metal interaction with the aromatic molecules tends to be very strong. For example, two conjugated rings could make a sandwich with the metal or the rings could stack, leaving the metal interaction only from one side of the ring. Therefore, having the aromatic peptide on a terminal position rather than the middle of a chain could lead to a difference in the dissociation path. Spectroscopically, metal-ligand charge transfer in the visible and also the positions of C-H and N-H stretch frequencies in the IR provide information on the environment near the metal. We can study how the addition of water molecules to the peptide affects metal binding using vibrational spectra. Comparing the results with calculated IR spectra can lead us to identify the structure of the complex.

6.3 References

- (1) Irikura, K. K.; Beauchamp, J. L. *J. Phys. Chem.* **1991**, *95*, 8344.
- (2) Zhang, X. G.; Liyanage, R.; Armentrout, P. B. *J. Am. Chem. Soc.* **2001**, *123*, 5563.
- (3) Carroll, J. J.; Weisshaar, J. C.; Siegbahn, P. E. M.; Wittborn, C. A. M.; Blomberg, M. R. A. *J. Phys. Chem.* **1995**, *99*, 14388.
- (4) Thompson, C. J.; Husband, J.; Aguirre, F.; Metz, R. B. *J. Phys. Chem. A* **2000**, *104*, 8155.
- (5) Faherty, K. P.; Thompson, C. J.; Aguirre, F.; Michne, J.; Metz, R. B. *J. Phys. Chem. A* **2001**, *105*, 10054.
- (6) Gilson, H. S. R.; Krauss, M. *J. Phys. Chem. A* **1998**, *102*, 6525.
- (7) Gilson, H. S. R.; Krauss, M. *J. Phys. Chem. A* **2000**, *104*, 5653.
- (8) Fedorchuk, C.; Swaddle, T. W. *J. Phys. Chem. A* **2000**, *104*, 5651.
- (9) Marini, G. W.; Liedl, K. R.; Rode, B. M. *J. Phys. Chem. A* **1999**, *103*, 11387.
- (10) Wright, R. R.; Walker, N. R.; Firth, S.; Stace, A. J. *J. Phys. Chem. A* **2001**, *105*, 54.
- (11) Stone, J. A.; Vukomanovic, D. *Int. J. Mass Spectrom.* **1999**, *185*, 227.
- (12) Metz, R. B. *Adv. Chem. Phys.* **2008**, *138*, 331.
- (13) Citir, M.; Metz, R. B. *J. Chem. Phys.* **2008**, *128*, 024307.
- (14) Bérces, A.; Nukada, T.; Margl, P.; Ziegler, T. *J. Phys. Chem. A* **1999**, *103*, 9693.

- (15) Thompson, C. J.; Faherty, K. P.; Stringer, K. L.; Metz, R. B. *Phys. Chem. Chem. Phys.* **2005**, *7*, 814.
- (16) Wyttenbach, T.; Evard, D. D.; Maier, J. P. *J. Chem. Phys.* **1989**, *90*, 4645.
- (17) Bowers, M. T.; Marshall, A. G.; McLafferty, F. W. *J Phys Chem* **1996**, *100*, 12897.
- (18) Luk, E. J., L. T.; Culotto, V. C. . *J. Biol. Inorg. Chem.* **2003**, *8*, 803.
- (19) Teesch, L. M.; Adams, J. *J. Am. Chem. Soc.* **1991**, *113*, 812.
- (20) Hu, P. F.; Sorensen, C.; Gross, M. L. *J. Am. Soc. Mass Spectrom.* **1995**, *6*, 1079.

BIBLIOGRAPHY

- (1) Aguirre, F.; Husband, J.; Thompson, C. J.; Metz, R. B. *Chem. Phys. Lett.* **2000**, *318*, 466.
- (2) Aguirre, F.; Husband, J.; Thompson, C. J.; Stringer, K. L.; Metz, R. B. *Journal of Chemical Physics* **2002**, *116*, 4071.
- (3) Åkesson, R.; Pettersson, L. G. M.; Sandström, M.; Wahlgren, U. *J. Phys. Chem.* **1992**, *96*, 150.
- (4) Allison, J.; Ridge, D. P. *J. Am. Chem. Soc.* **1979**, *101*, 4998.
- (5) Armentrout, P. B. *Int. J. Mass Spectrom.* **2000**, *200*, 219.
- (6) Armentrout, P. B.; Kickel, B. L. Gas-Phase Thermochemistry of Transition Metal Ligand Systems: Reassessment of Values and Periodic Trends. In *Organometallic Ion Chemistry*; Freiser, B. S., Ed.; Kluwer Academic Publishers: Dordrecht, The Netherlands, 1994; pp 1.
- (7) Bange, H. W., Williams, J. *Atmospheric Environment* **2000**, *34*, 4959.
- (8) Bauschlicher, C. W., Jr.; Maitre, P. *Theor. Chim. Acta* **1995**, *90*, 189.
- (9) Belau, L.; Wilson, K. R.; Leone, S. R.; Ahmed, M. *J. Phys. Chem. A* **2007**, *111*, 7562.
- (10) Bellert, D.; Buthelezi, T.; Brucat, P. J. *Chem. Phys. Lett.* **1998**, *290*, 316.
- (11) Bellert, D.; Buthelezi, T.; Hayes, T.; Brucat, P. J. *Chem. Phys. Lett.* **1997**, *276*, 242.
- (12) Bérces, A.; Nukada, T.; Margl, P.; Ziegler, T. *J. Phys. Chem. A* **1999**, *103*, 9693.
- (13) Beyer, M. K.; Metz, R. B. *J. Phys. Chem. A* **2003**, *107*, 1760.
- (14) Blades, A. T.; Jayaweera, P.; Ikonomou, M. G.; Kebarle, P. *Int. J. Mass Spec. Ion Proc.* **1990**, *102*, 251.

- (15) Böhme, D. K.; Schwarz, H. *Angew. Chem., Int. Ed. Engl.* **2005**, *44*, 2336.
- (16) Bowers, M. T.; Marshall, A. G.; McLafferty, F. W. *J Phys Chem* **1996**, *100*, 12897.
- (17) Burrows, A.; Dulick, M.; Bauschlicher, C. W., Jr.; Bernath, P. F.; Ram, R. S.; Sharp, C. M.; Milsom, J. A. *Astrophys. J.* **2005**, *624*, 988.
- (18) Campbell, M. L. *J. Chem. Soc. Faraday Trans.* **1998**, *94*, 353.
- (19) Carroll, J. J.; Weisshaar, J. C. *J. Phys. Chem.* **1996**, *100*, 12355.
- (20) Carroll, J. J.; Weisshaar, J. C.; Siegbahn, P. E. M.; Wittborn, C. A. M.; Blomberg, M. R. A. *J. Phys. Chem.* **1995**, *99*, 14388.
- (21) Centi, G.; Cavani, F.; Trifirò, F. *Selective Oxidation by Heterogeneous Catalysis*; Kluwer Academic: New York, 2001.
- (22) Chowdhury, S. K.; Katta, V.; Chait, B. T. *J. Rapid Commun. Mass Spectrom.* **1990**, *4*, 81.
- (23) Citir, M.; Altinay, G.; Metz, R. B. *J. Phys. Chem. A* **2006**, *110*, 5051.
- (24) Citir, M.; Metz, R. B. *J. Chem. Phys.* **2008**, *128*, 024307.
- (25) Citir, M.; Metz, R. B.; Belau, L.; Ahmed, M. *J. Phys. Chem. A* **2008**, *112*, 9584.
- (26) Crabtree, R. H. *Wiley: New York* **2005**, *4th ed.*
- (27) Drowart, J.; Chatillon, C.; Hastie, J.; Bonnell, D. *Pure Appl. Chem.* **2005**, *77*, 683.
- (28) Duncan, M. A. *Int. Rev. Phys. Chem.* **2003**, *22*, 407.
- (29) Eller, K.; Schwarz, H. *Chem. Rev.* **1991**, *91*, 1121.
- (30) Faherty, K. P.; Thompson, C. J.; Aguirre, F.; Michne, J.; Metz, R. B. *J. Phys. Chem. A* **2001**, *105*, 10054.

- (31) Fedorchuk, C.; Swaddle, T. W. *J. Phys. Chem. A* **2000**, *104*, 5651.
- (32) *Organometallic Ion Chemistry*; Freiser, B. S., Ed.; Kluwer Academic Publishers: Dordrecht, 1996; Vol. 15.
- (33) Frisch, M. J.; Trucks, G. W.; Schlegel, H. B.; Scuseria, G. E.; Robb, M. A.; Cheeseman, J. R.; Zakrzewski, V. G.; Montgomery, J. A.; Stratmann, R. E.; Burant, J. C.; Dapprich, S.; Millam, J. M.; Daniels, A. D.; Kudin, K. N.; Strain, M. C.; Farkas, O.; Tomasi, J.; Barone, V.; Cossi, M.; Cammi, R.; Mennucci, B.; Pomelli, C.; Adamo, C.; Clifford, S.; Ochterski, J.; Petersson, G. A.; Ayala, P. Y.; Cui, Q.; Morokuma, K.; Malick, D. K.; Rabuck, A. D.; Raghavachari, K.; Foresman, J. B.; Cioslowski, J.; Ortiz, J. V.; Stefanov, B. B.; Liu, G.; Liashenko, A.; Piskorz, P.; Komaromi, I.; Gomperts, R.; Martin, R. L.; Fox, D. J.; Keith, T.; Al-Laham, M. A.; Peng, C. Y.; Nanayakkara, A.; Gonzalez, C.; Challacombe, M.; Gill, P. M. W.; Johnson, B. G.; Chen, W.; Wong, M. W.; Andres, J. L.; Head-Gordon, M.; Replogle, E. S.; Pople, J. A. *Gaussian 98*; Revision A.3 ed.; Gaussian, Inc.: Pittsburgh PA, 1998.
- (34) Gilson, H. S. R.; Krauss, M. *J. Phys. Chem. A* **1998**, *102*, 6525.
- (35) Gilson, H. S. R.; Krauss, M. *J. Phys. Chem. A* **2000**, *104*, 5653.
- (36) Gregoire, G.; Duncan, M. A. *J. Chem. Phys.* **2002**, *117*, 2120.
- (37) Hammer, N. I.; Diken, E. G.; Roscioli, J. R.; Johnson, M. A.; Myshakin, E. M.; Jordan, K. D.; McCoy, A. B.; Huang, X.; Bowman, J. M.; Carter, S. *J. Chem. Phys.* **2005**, *122*, Art. No. 244301.
- (38) Heinemann, C.; Schwarz, H.; Koch, W.; Dyall, K. G. *J. Chem. Phys.* **1996**, *104*, 4642.
- (39) Heinemann, C.; Wesendrup, R.; Schwarz, H. *Chem. Phys. Lett.* **1995**, *239*, 75.
- (40) Him, T.; Tolmachev, A. V.; Harkewicz, R.; Prior, D. C.; Anderson, G.; Udseth, H. R.; Smith, R. D.; Bailey, T. H.; Rakov, S.; Futrell, J. H. *Anal. Chem.* **2000**, *72*, 2247.
- (41) Hu, P. F.; Sorensen, C.; Gross, M. L. *J. Am. Soc. Mass Spectrom.* **1995**, *6*, 1079.

- (42) Husband, J. *Thesis University of Massachusetts Amherst* **2001**.
- (43) Husband, J.; Aguirre, F.; Thompson, C. J.; Laperle, C. M.; Metz, R. B. *J. Phys. Chem. A* **2000**, *104*, 2020.
- (44) Irikura, K. K.; Beauchamp, J. L. *J. Phys. Chem.* **1991**, *95*, 8344.
- (45) Judai, K. S., K.; Amatsutsumi, S.-i.; Yagi, K.; Yasuike, T.; Yabushita, S.; Nakajima, A.; Kaya, K. *Chem. Phys. Lett.* **2001**, *334*, 277.
- (46) Kebarle, P. *Int. J. Mass Spectrom.* **2000**, *200*, 313.
- (47) Kebarle, P.; Tang, L. *Anal. Chem.* **1993**, *65*, 972A.
- (48) Keese, R. G.; A. W. Castleman, J. *J. Phys. Chem. Ref. Data* **1986**, *15*, 1011.
- (49) Kim, J. H.; Ishihara, A.; Mitsushima, S.; Kamiya, N.; Ota, K. I. *Electrochim. Acta* **2007**, *52*, 2492.
- (50) Kohler, M.; Leary, J. A. *Int. J. Mass Spectrom. Ion Proc.* **1997**, *162*, 17.
- (51) Kohler, M.; Leary, J. A. *J. Am. Soc. Mass Spectrom.* **1997**, *8*, 1124.
- (52) Koszinowski, K.; Schröder, D.; Schwarz, H. *J. Phys. Chem. A* **2003**, *107*, 4999.
- (53) Koyanagi, G. K.; Bohme, D. K. *J. Phys. Chem. A* **2006**, *110*, 1232.
- (54) Laskin, J.; Lifshitz, C. *J. Mass Spectrom.* **2001**, *36*, 459.
- (55) Lever, A. B. P. *Inorganic Electronic Spectroscopy (Second Edition)*; Elsevier: Amsterdam, 1984.
- (56) Lisy, J. M. *Int. Rev. Phys. Chem.* **1997**, *16*, 267.
- (57) Luk, E. J., L. T.; Culotto, V. C. . *J. Biol. Inorg. Chem.* **2003**, *8*, 803.
- (58) Marini, G. W.; Liedl, K. R.; Rode, B. M. *J. Phys. Chem. A* **1999**, *103*, 11387.

- (59) McLaughlin, B. M.; Ballance, C. P.; Berrington, K. A. *J. Phys. B-At. Mol. Opt. Phys.* **2001**, *34*, L179.
- (60) Merer, A. J. *Ann. Rev. Phys. Chem.* **1989**, *40*, 407.
- (61) Metz, R. B. *Int. J. Mass Spectrom.* **2004**, *235*, 131.
- (62) Metz, R. B. *Int. Rev. Phys. Chem.* **2004**, *23*, 79.
- (63) Metz, R. B. *Adv. Chem. Phys.* **2008**, *138*, 331.
- (64) Metz, R. B.; Nicolas, C.; Ahmed, M.; Leone, S. R. *J. Chem. Phys.* **2005**, *123*, 114313.
- (65) Nicolas, C.; Shu, J.; Peterka, D. S.; Poisson, L.; Leone, S. R.; Ahmed, M. *J. Am. Chem. Soc.* **2006**, *128*, 220.
- (66) O'Connor, P. B., Costello, C. E., Earle, W. E. *Journal of the American Society for Mass Spectrometry* **2002**, *13*, 1370.
- (67) Okumura, M.; Yeh, L. I.; Meyers, J. D.; Lee, Y. T. *J. Chem. Phys.* **1986**, *85*, 2328.
- (68) Parke, L. G., Hinton, C. S., Armentrout, P. B. *J. Phys. Chem. C.* **2007**, *111*, 17773.
- (69) Peschke, M.; Blades, A. T.; Kebarle, P. *J. Am. Chem. Soc.* **2000**, *122*, 1492.
- (70) Posey, L. A., DeLuca, M. J., Johnson, M. A. *Chemical Physics Letters* **1986**, *131*, 170.
- (71) Prior, D. A., G.; Bruce, J.; Schaeffer, S.; Kim, T. M.; Smith, R. *Computing and Information Sciences 1999 Annual Report* **1999**, PNNL.
- (72) Proch, D., Trickl, T. *Rev. Sci. Instrum.* **1989**, *60*, 713.
- (73) Rodriguez-Cruz, W. E.; Jockusch, R. A.; Williams, E. R. *J. Am. Chem. Soc.* **1998**, *120*, 5842.

- (74) Sappey, A. D.; Eiden, G.; Harrington, J. E.; Weisshaar, J. C. *J. Chem. Phys.* **1989**, *90*, 1415.
- (75) Scheer, M.; Haugen, H. K.; Brooks, R. L. **1999**, *61*, 12505.
- (76) Schinke, R. *Photodissociation Dynamics*; University Press: Cambridge, 1993.
- (77) Schröder, D.; Schwarz, H. *Angew. Chem. Int. Ed. Engl.* **1995**, *34*, 1973.
- (78) Shvartsburg, A. A.; Siu, K. W. M. *J. Am. Chem. Soc.* **2001**, *123*, 10071.
- (79) Shvartsburg, A. A.; Wilkes, J. G.; Lay, J. O.; Siu, K. W. M. *Chem. Phys. Lett.* **2001**, *350*, 216.
- (80) Smith, J. N.; Flagan, R. C.; Beauchamp, J. L. *J. Phys. Chem. A* **2002**, *106*, 9957.
- (81) Stace, A. J. *J. Phys. Chem. A* **2002**, *106*, 7993.
- (82) Stace, A. J.; Walker, N. R.; Firth, S. *J. Am. Chem. Soc.* **1997**, *119*, 10239.
- (83) Stone, J. A.; Vukomanovic, D. *Int. J. Mass Spectrom.* **1999**, *185*, 227.
- (84) Swaddle, T. W.; Fabes, L. *Can. J. Chem.* **1980**, *58*, 1418.
- (85) Teesch, L. M.; Adams, J. *J. Am. Chem. Soc.* **1991**, *113*, 812.
- (86) Thompson, C. J.; Faherty, K. P.; Stringer, K. L.; Metz, R. B. *Phys. Chem. Chem. Phys.* **2005**, *7*, 814.
- (87) Thompson, C. J.; Husband, J.; Aguirre, F.; Metz, R. B. *J. Phys. Chem. A* **2000**, *104*, 8155.
- (88) Usui, K.; Kiden, K.; Murata, S.; Nomura, M.; Trisunaryanti, W. *Fuel* **2004**, *83*, 1899.
- (89) Walker, N. R.; Walters, R. S.; Duncan, M. A. *J. Chem. Phys.* **2004**, *120*, 10037.
- (90) Weisshaar, J. C. *Acc. Chem. Res.* **1993**, *26*, 213.

- (91) Wiley, W. C., McLaren, I. H. *Rev. Sci. Instrum.* **1955**, *26*, 1150.
- (92) Wright, R. R.; Walker, N. R.; Firth, S.; Stace, A. J. *J. Phys. Chem. A* **2001**, *105*, 54.
- (93) Wyttenbach, T.; Evard, D. D.; Maier, J. P. *J. Chem. Phys.* **1989**, *90*, 4645.
- (94) Xu, X.; Faglioni, F.; William A. Goddard, I. *J. Phys. Chem. A* **2002**, *106*, 7171.
- (95) Yamashita, M.; Fenn, J. B. *J. Phys. Chem.* **1984**, *88*, 4451.
- (96) Zhang, X. G.; Liyanage, R.; Armentrout, P. B. *J. Am. Chem. Soc.* **2001**, *123*, 5563.